Title
Neural Dust: Ultrasonic Biological Interface

Author
Seo, Dongjin

Publication Date
2016

Peer reviewed|Thesis/dissertation

Neural Dust: Ultrasonic Biological Interface

by

Dongjin Seo

A dissertation submitted in partial satisfaction of the
requirements for the degree of
Doctor of Philosophy

in

Engineering - Electrical Engineering and Computer Sciences

in the

Graduate Division

of the

University of California, Berkeley

Committee in charge:

Professor Michel M. Maharbiz, Chair
Professor Elad Alon
Professor John Ngai

Fall 2016

Neural Dust: Ultrasonic Biological Interface

Abstract

Neural Dust: Ultrasonic Biological Interface

by

Dongjin Seo

Doctor of Philosophy in Engineering - Electrical Engineering and Computer Sciences

University of California, Berkeley

Professor Michel M. Maharbiz, Chair

A seamless, high density, chronic interface to the nervous system is essential to enable clinically relevant applications such as electroceuticals or brain-machine interfaces (BMI). Currently, a major hurdle in neurotechnology is the lack of an implantable neural interface system that remains viable for a patient's lifetime due to the development of biological response near the implant. Recently, mm-scale implantable electromagnetics (EM) based wireless neural interfaces have been demonstrated in an effort to extend system longevity, but the implant size scaling (and therefore density) is ultimately limited by the power available to the implant.

In this thesis, we propose neural dust, an entirely new method of wireless power and data telemetry using ultrasound, which can address fundamental issues associated with using EM to interrogate miniaturized implants. Key concepts and fundamental system design trade-offs and ultimate size, power, and bandwidth scaling limits of such system are analyzed from first principles. We demonstrate both theoretically and experimentally that neural dust scales extremely well, down to 100's, if not 10's of μm. We highlight first wireless recordings from nerve and muscle in an animal model using neural dust prototype. The thesis concludes with strategies for multi-neural dust interrogation and future directions of neural dust beyond neuromodulation.

To my loving parents Taewon and Kyunghee and my sister Dongeun (Jane).

Contents

List of Figures

List of Tables

Acknowledgments

For the past few years, I have had the fortune of meeting perhaps the most incredible set of people here at Berkeley. It has been a truly humbling experience and I have grown in so many dimensions. I do not expect that this acknowledgement section will do justice to how thankful I am to you all. Thank you all for playing such a crucial role in a very important chapter of my life.

I have been incredibly lucky to have not one, but two amazing advisors here at Berkeley. I would like to first thank Prof. Elad Alon who welcomed me to the Berkeley community and his newly formed group at the time. As a first-year graduate student, I wrestled with what would be the "right" project and "right" people to work with, and how my choices now will set the course for the rest of my graduate school[1]. During this time, Elad was extremely patient, helped me navigate through many different projects I was interested in, and taught me how to ask research questions. His ability to communicate difficult engineering ideas and his attention to details have been a constant source of inspiration. Thank you for being attentive.

I would also like to thank Prof. Michel Maharbiz. When I first met Michel, I was instantly drawn to his infectious energy and his ability to capture everyone's wildest imagination. I have always been in awe of his ability to absorb information, digest, massage and add a little sprinkle of Maharbiz magic, and produce perhaps the most insane, yet feasible ideas. I will miss the countless number of hours in his office, bouncing ideas off each other, strategizing, bantering, and playing D&D. When he takes his academic advisor hat off, Michel is also a great cook, a bouldering partner, and a friend. Thank you for being more than an academic advisor to me.

I am very grateful to have other two members of the original neural dust mafia, Prof. Jose Carmena and Prof. Jan Rabaey. Jose introduced me to the BMI community here at UC Berkeley and UCSF through his EE290P class and his incredible connections. His ability to think big and razor focus on the prize and opening up his lab for the in-vivo experiments made neural dust possible. Jan was also instrumental in the conception of neural dust. It was his vision that created centers such as Berkeley Wireless Research Center and Swarm lab that provided me the resources that I need to execute the project.

I am thankful to have Prof. John Ngai as my outside qualifying and dissertation committee member. His willingness to take an interest in my work and his insights have been tremendously helpful in taking the project on the right path from the start.

I am incredibly lucky to have had a series of amazing mentors who have truly made everything possible. In high school, Prof. Abdul Barakat invited our family to his then lab at UC Davis and also gave me my very first research project, looking at functional study and shape control of vascular endothelial cells. I am honored to have had my academic experience start under his supervision. Prof. Michael Roukes and Prof. Wonhee Lee introduced me to

[1]Turns out this is usually not the case – I dabbled on at least five different projects in the beginning. But it was a fun experience and an opportunity to learn so much about many different fields. So, if you are a first-year reading this, don't be stressed; have fun.

the world of microfabrication, mentoring me throughout my first experience in the cleanroom. Prof. Pietro Perona and Prof. Michael Maire tasked me with several exciting computer vision projects. Prof. Ali Hajimiri captivated me to analog circuit design with his classes. My then graudate student mentor, Prof. Kaushik Sengupta, gave me the opportunity to work on an independent project as a junior at Caltech and taught me how to think outside the box. I am very thankful that with their supervision, I was able to publish my first academic paper, attend conferences, present at group meeting, and sample what it is like to be a graduate student.

I would like to extend a huge thanks to all the members of several labs and centers I had the privilege of being part of over the years. Chronologically, I would like to thank the past and current members of the Barakat lab, Roukes lab, Perona lab, Hajimiri lab, Alon lab, Carmena lab, Rabaey lab, and Maharbiz lab and the cohorts at 550 Cory, BWRC, and Swarm lab. Members of those labs and centers were truly exceptional groups of people and I thank them for being collaborators, mentors, and friends.

I have also had the incredible fortune of working with many talented undergraduate or visiting students over the course of my Ph.D. I would like to thank Clark Chen, Shreyas Parthasarathy, Tamara Rossy, Rebecca Sandrone, Ryan Shih, Utkarsh Singhal, Kyle Slater, Xiaoshan Wang, and Brent Yi. Neural dust would not be possible without all your hard work.

I would like to acknowledge support from the past and current staffs at BWRC, BSAC, and SWARM lab. Semi-annual retreats were great motivators for me to hit the intermediate milestones, showcase my work, and connect with industry folks.

I would like to acknowledge the past and current staffs at the department of EECS at Berkeley and Marvell nanolab. A special thanks to Shirley Salanio for helping me navigate through a number of graduation requirements and departmental forms and Eric Arvai for helping me with recording the dissertation talk and video editing.

I would like to thank TSMC for providing fabrication support on several different projects throughout my Ph.D.

I would like to especially acknowledge the following people. I would like to thank Dr. Lingkai Kong for being my graduate student contact during my visit to Berkeley and later a mentor of all forms. I thank you for your wisdom and your patience. I thank Nathan Narvesky for his breath and depth of knowledge in hardware design and his willingness to help and brainstorm with me on various ideas throughout my Ph.D. Huge thanks to Prof. Alexander Bertrand who was instrumental in the work described in Chapter 5 during his short visit. I am grateful to Konlin Shen for all his help with the fabrication of neural dust motes in the early days and his positivity that uplifted me during the tough times. I was lucky to have Ryan Neely as my partner-in-crime during the in-vivo recordings with neural dust. His ability to execute and sometimes improvise was instrumental to the work described in Chapter 4. I would like to thank Dr. Hao-Yen Tang for our collaboration with his low-power ultrasonic imager ASIC. His strong technical background, work ethic, and the ability to identify important research questions was truly inspiring. I would like to extend my gratitude to my friend Christopher Sutardja who was able to connect me with on a

personal level. Thank you for your friendship.

I would like to acknowledge the past and current members of the Korean EECS Association (KEECS) and Korean Graduate Student Association (KGSA). I would like to especially thank Dr. Kangwook Lee, Dr. Jaehwa Kwak, Dr. Sangyoon Han, Jaeduk Han, Taehwan Kim, Hoekun Kim, Seobin Jung, and Kyoungtae Lee for their friendship and helping me with my Korean. A deepest gratitude to all the members of the Gilman soccer club and Galácticos. I have played and loved soccer all my life and being able to play with such an amazing group of people was one of the most memorable moments of my Ph.D.

I would also like to acknowledge National Science Foundation's Graduate Research Fellowship (NSFGRF) and Defense Advanced Research Project Agency (DARPA) for their financial support. I was fortunate to have been collectively funded by these organizations for nearly my entire Ph.D. The work described here would not have been possible without their support.

Most of all, I owe any successes to my family. Words cannot express your love and sacrifice.

Finally, I would like to thank my better half Yeounsu (Yvonne) Kim for making every day wonderful and dynamic.

Chapter 1

Introduction

> As long as our brain is a mystery, the universe, the reflection of the structure of the brain will also be a mystery.
>
> *Santiago Ramón y Cajal*

Half a century of scientific and engineering effort has yielded a vast body of knowledge about the human nervous system as well as a set of tools for stimulating and recording from neurons. Recently proposed roadmaps for the field of neuromodulation [1, 29] highlight the need for neural interface technologies that can record appropriate physiological markers across multiple biological targets and be used to update stimulation parameters in real-time.

Key features of such closed-loop technologies include high-density, stable recordings of many neurons, wireless and implantable modules to enable characterization of functionally specific neural signals, and scalable device platform that can interface with small nerves or single cortical neurons of 100 μm of diameter or less. Such closed-loop system that can both decipher and precisely modulate physiological activity in the body can have immediate benefits. For clinically relevant applications, such as bioelectronic medicine (or electroceuticals) [29] and brain-machine interfaces (BMI) [17], such system can offer immediate therapeutic effects for patient groups suffering from neurodegenerative diseases such as epilepsy, tetraplegia, amyotropic lateral sclerosis (ALS), cerebral palsy, peripheral neuropathy, and many more. Beyond specific patient groups, seamless interface to the nervous system can enable high bandwidth analog input and output interface to our electronic devices, bypassing limits imposed by especially our low bandwidth digital outputs (i.e., speech, typing, etc.).

This thesis presents the analysis, design, and experimental verification of one promising biological interface technology called *neural dust* that can enable significant scaling in the number of neural recordings from the nervous system while providing a path towards a truly chronic neural recording solution.

1.1 Interface to the nervous system

Currently, there are numerous modalities with which one can extract information from the nervous system. Advances in imaging technologies such as functional magnetic resonance imaging (fMRI), electroencephalography (EEG), positron emission tomography (PET), and magnetoencephalography (MEG) have provided a wealth of information about collective behaviors of groups of neurons [12]. Numerous efforts are focusing on intra- [110] and extra-cellular [26] electrophysiological recording and stimulation, molecular recording [114], optical recording [115], and hybrid techniques such as opto-genetic stimulation [15] and photo-acoustic [30] methods to perturb and record the individual activity of neurons in large ensembles.

1.1.1 In-vivo demonstrations

By far the most popular method for recording from the nerve is the direct electrical measurement of potential changes near relevant neurons during depolarization events called action potentials (AP) using multi-electrode technology. Various neural probes (or microelectrode arrays) exist[1], which are typically at least 1 mm long and less than 50 μm wide at the tip. The spacing between the probes is on the order of a few 100's of μm and recording sites are located either along the shaft or at the tip of each electrode. Variants of microelectrode arrays are used both in non-human primates and in humans to demonstrate control of robotic prosthetic arms [16, 21, 40, 73, 75], control of wheelchair [85], restoring movement impaired by spinal cord injury [14], and sensation [32].

One of the biggest issues with microelectrode arrays or any penetrating electrode technology, however, is the immunoresponse of the brain tissue upon insertion at the implant site. Once the probes are inserted, scar tissue forms around the probes and can cover the recording site of the array, degrading the signal-to-noise (SNR) of the recorded signals over time [81]. Improvements in the surgical procedures (i.e., reducing the mechanical mismatch between electrode arrays and soft tissue), materials and shapes of electrodes, and miniaturization of electrodes with novel microfabrication processes have been studied but longevity of recordings with multi-electrodes are still one of the biggest hurdles to overcome.

1.1.2 Trends and scaling of wired neural interfaces

Since the introduction of multi-electrode recording technology in the 1950s to record from the brain [2], the number of recording channels and therefore the number of neurons simultaneously recorded have witnessed a tremendous growth. Examination of studies published over the past few decades has resulted in "Stevenson's law" which observed that the number of simultaneously recorded neurons have doubled approximately every 7 years especially

[1]Examples include Utah array [63], Michigan probes [109], Duke array [72].

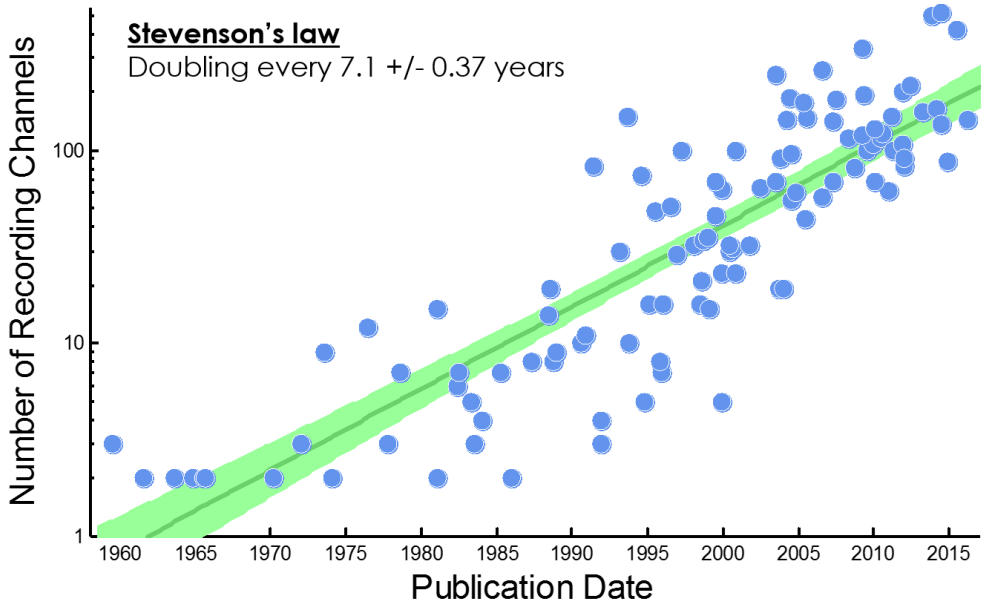

Figure 1.1: Stevenson's law observed from the past 5 decades of research that there is doubling in the number of simultaneously recorded neurons (or recording channels) approximately every 7 years. This law predicts that it will be ∼100 years until we can record from one million neurons simultaneously.

since the 1950s [99]. This is akin to the famous Moore's law which predicted doubling of device density[2] every 2 years.

Although rapid advances have been observed in neurotechnology over the years, Stevenson's law predicts that, at the current rate of growth, it would take 15 years until we can record from approximately 1,000 neurons, 60 years until we reach 100,000 neurons, and in ∼100 years, physiologists should be able to record from 1,000,000 (one million) neurons. Note that this is also rather optimistic in that it assumes unperturbed, continuous scaling of multi-electrode technology, which is certainly fraught with its set of limitations, such as interconnect density limit, micro-fabrication challenges, tissue scarring, and many more.

The trend indicates that new technological breakthroughs are necessary in order to accelerate growth, similar to the disruption of Moore's law with the introduction of CMOS technology. Several groups are investigating novel technologies, such as advanced imaging technologies utilizing two-photon microscopy [20, 28], wireless implantable devices [10, 68, 98, 102], molecular-level recording [35, 53, 114], and hybrid techniques such as opto-genetics [15, 24, 80] and photo-acoustic methods [30, 108]. All modalities, of course, have some fundamental tradeoffs and are usually limited in temporal or spatial resolution, portability, power, invasiveness, etc. A comprehensive review of tradeoffs focused on recording from all

[2]There are variants of Moore's law: doubling of (number of transistors, component cost, etc.) every 2 years.

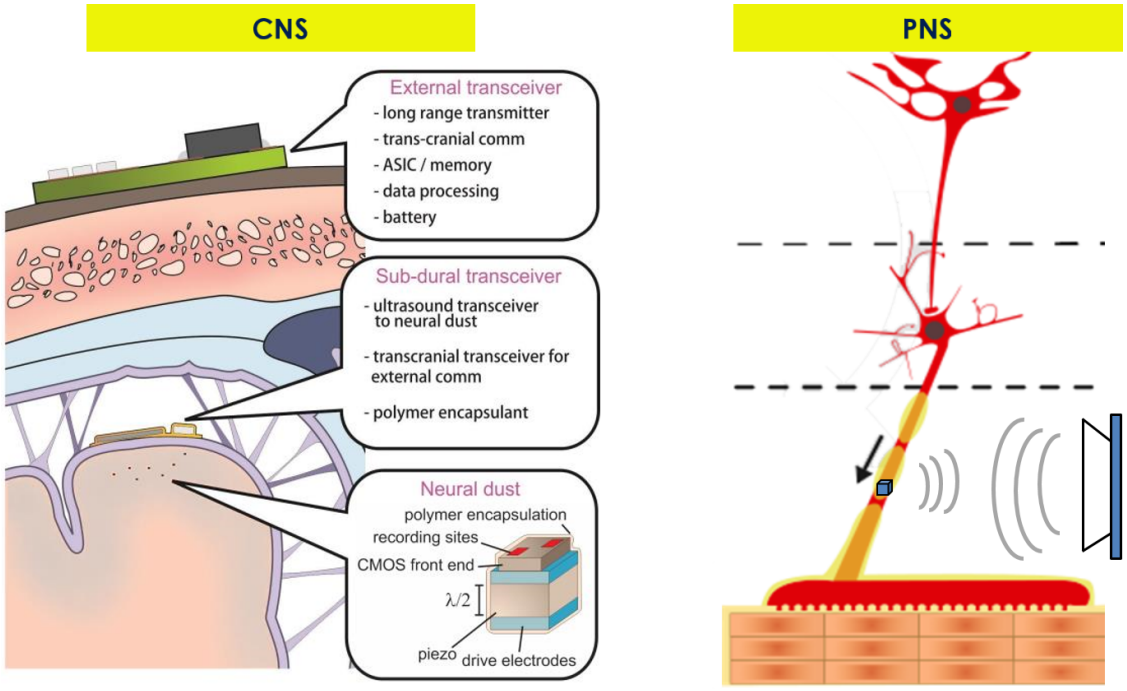

Figure 1.2: Neural dust system can be configured to record from the neocortex (left) or from afferent or efferent nerves in the peripheral nervous system (right). Note that for interfacing with the central nervous system (left), ultrasonic transceiver is implanted sub-cranially and powered by an external transceiver via EM. For peripheral nervous system (right), such tiered approach is not necessary as highly attenuative (to ultrasound) bone is not directly in the path of ultrasound waves.

neurons in a mouse brain can be found in [62].

1.1.3 Wireless neural interfaces

Recently, wireless devices to enable untethered recording in rodents [59, 102] and nonhuman primates [33, 94, 113], as well as mm-scale integrated circuits for neurosensing application [10, 25, 71] have been developed. However, most wireless systems use electromagnetic (EM) energy coupling and communication, which becomes extremely inefficient in systems smaller than ∼5 mm due to the inefficiency of coupling radio waves at these scales within tissue [84, 96]. Detailed analysis of this will be covered in Chapter 2 and Chapter 3.

1.2 Thesis Contribution

We introduce *neural dust*, which is an ultra-miniature as well as extremely compliant biological interface shown in Figure 1.2, for both interfacing with the central nervous system

(CNS) and the peripheral nervous system (PNS). The system is designed in light of a need for radical improvements in scalability. In this thesis, we primarily focus on the analysis, design, and experimental verification of *neural dust* that can enable significant scaling in the number of neural recordings from the nervous system while providing a path towards a truly chronic neural recording solution.

1.3 Thesis Organization

The rest of this thesis is organized as follows:

- **Chapter 2:** In this chapter, we provide an overview of available wireless power transfer (WPT) techniques to power implantable systems. We examine tradeoffs among different methods qualitatively and compare the performance of previously published work. In particular, we study how commonly used electromagnetics (EM) based WPT performs at the millimeter and sub-millimeter scale necessary for the proposed high-density neural interfaces. We conclude with simulations that due to the non-linear interplay of form factor, speed of light, and frequency spectra of tissue absorption, EM-based power transmission is not an appropriate energy modality for powering sub-mm sized implants.

- **Chapter 3:** In this chapter[3], we show ultrasound as a viable alternative method to power sub-mm implantable systems. We introduce a novel neural interface system, called *neural dust*, which uses ultrasound to couple power to small implantable "motes" and wirelessly communicate recorded signals via backscattering. We provide theory, system design tradeoffs, scaling limits, and simulations of neural dust as a platform to record from the neocortex. We verify experimentally that our model correctly predicts power transfer efficiency and backscatter sensitivity down to 100 μm scales.

- **Chapter 4:** In this chapter[4], we demonstrate wireless recordings from nerve and muscle in a rodent model using neural dust. We show hardware implementation of the transceiver and a mm-sized neural dust mote prototype fabricated on a commercially available polyimide backplane. We benchmark the performance of neural dust in a water tank setup and verified that the performance did not degrade much in a rodent model. As the first in-vivo electrophysiological recordings with neural dust, this work highlights the potential for an ultrasound-based neural interface system for advancing future bioelectronics-based therapies.

[3] A part of this chapter was published in arXiv [96] and Journal of Neuroscience Methods [95].

[4] This chapter is done in collaboration with Ryan M. Neely and Dr. Hao-Yen Tang. A part of this chapter was presented in IEEE Engineering in Medicine and Biology Conference [97] and published in IEEE Transaction on Biomedical Circuits and Systems [105] and Neuron [98].

- **Chapter 5:** In this chapter[5], we explore more in-depth analysis of cooperative transmit (TX) and receive (RX) beamforming approaches with multiple transceivers to enable multi-mote interrogation. We discuss the mathematical formalization of the problem and simulate the model to compare the performance of different beamforming techniques. We show that linearly constrained minimum variance (LCMV) beamforming technique performs the best and that cooperation among transceivers is necessary to suppress interference from neighboring motes and achievable sufficient signal-to-noise ratio. We examine spatial multiplexing scheme to increase the overall throughput and hierarchical processing flow to reduce the processing and communication burden.
- **Chapter 6:** we conclude the thesis with the summary of the results and important future research directions.

[5]This chapter is done in collaboration with Dr. Alexander Bertrand. A part of this chapter was presented in IEEE Engineering in Medicine and Biology Conference [8].

Chapter 2

Powering Implantable Systems

> If you want to find the secrets of the universe, think in terms of energy, frequency and vibration
>
> *Nikola Tesla*

In this chapter, we provide an overview of options available to power an implantable device, which requires a long term, safe, and reliable source of energy for operation. Since the introduction of the first cardiac pacemakers in 1958 [3], batteries have been the traditional method of supplying power to implants. Although batteries are a convenient and reliable source of energy with relatively high energy density, and despite rapid advances in electrochemical energy storage, their limited lifetime and leakage of harmful chemicals require subsequent replacements and limits their usage. This is especially problematic for powering miniature implants. Additionally, to eliminate the risk of infection associated with the transcutaneous/trans-cranial wires required for power, such tethers should be avoided as much as possible; a wireless hub is therefore essential to relay the information recorded by the device through the skull or the skin. As a result, we explore several different methods for powering implants wirelessly[1].

2.1 Wireless powering options

The requirements for any implantable device employing microelectrodes to acquire useful neural signals are fairly stringent. The two primary constraints on the implanted device are size and power. On the one hand, in order to reduce the biological response near the implant

[1]There are alternative methods that look to harvest energy from the environment, such as kinetic, thermal, solar, chemical, etc. that are not discussed here. For detailed treatment, refer to [91].

site[2], it is highly desirable to minimize the volume of the implant. However, reducing the size of the implant not only reduces the amount of power smaller devices can collect, but reduces the distance between recording points, which decreases the absolute magnitude of the measured potentials. This decreased amplitude exacerbates the constraints on the electronics as it needs to reduce its noise and cram similar functionality in a smaller footprint. With this tradeoff in mind, we will examine several wireless powering modalities.

2.1.1 Electromagnetic (EM) power transfer

Electromagnetic (EM) means of wireless power transfer are the most commonly used method. Generally, an EM field source (e.g., point, dipole, antenna, or coil) produces EM waves in the surrounding media, which then interacts with the media to generate non-radiative and radiative components of the EM waves. As the EM waves propagate away from the source, its wave properties change and the characteristics of the wave can be divided into near-field (i.e., closer to the source) and far-field; Rayleigh distance is the distance at which the field characteristics transition from near-field to far-field [3].

There are several variants of the EM power transfer but all methods can be broadly classified under the following two categories: non-radiative (or near-field) and radiative (or far-field). Non-radiative methods refer to either electric (i.e., capacitive) or magnetic (i.e., inductive) field based power transfer that occurs in the near-field of the transmitter. Radiative methods, on the other hand, refer to power transfer by beams of electromagnetic radiation. The beam consists of both electric and magnetic field components and the field generally decays with $1/r^2$. The mode of EM power transfer is largely determined by the operation frequency (f_{res}), wavelength in the propagation medium (λ), aperture of the transmitter (D), and propagation distance (d).

Inductive powering

Inductive powering is the most widely used non-radiative technique to transfer energy across tissue. An external coil (primary) generates time-varying fields, which are primarily magnetic in nature (i.e., quasi-magnetostatic), and couple energy to an implant with a separate coil (secondary) via magnetic induction. The efficiency of inductive powering largely depends on the self-inductance and the mutual coupling between the two coils. These parameters are directly related to the size of the coils and inversely proportional to the distance between the coils, which limit the achievable range and efficiency. The range is usually limited to distance on the order of the diameter of the secondary coil.

There have been several techniques, such as resonance and adaptive tuning [93], quality factor enhancement [86], and multi-coil configuration [50] to improve inductive powering.

[2]In addition to disrupting normal biological behaviors, formation of scar tissue around the implant can significantly degrade its performance.

[3]This is a crude approximation of the intricate physics involved in wave propagation. For detailed treatment, refer to [5, 82].

Efficiency of over 82% have been demonstrated [86]. However, due to the exponential decay of the evanescent near-field, the mutual coupling between the coils drops dramatically and significantly degrades the transfer efficiency and increases the sensitivity to misalignment. Therefore, in order to achieve sufficient link robustness and transfer efficiency, coils are usually in the cm range for implants.

Mid-field powering

Sandwiched between the near-field and far-field of the transmitter is mid-field. Mid-field wireless powering relies on the focusing of radiation and is shown to address the downfalls of the efficiency degradation when the implant is much smaller than its distance from the source [38, 39]. By combining inductive and radiatve mode, high efficiency can be achieved in the low-GHz range and mid-field enables efficient powering of miniature implant (or the case when the dimension is comparable to the distance from its source).

Mid-field powering, however, requires proper engineering of source current and phase distribution in the antenna, which depends on the knowledge of the channel a priori; the ability to focus energy at a desirable depth is sensitive to uncertainty in the channel properties. However, this method offers more efficient means of powering mm-sized implants compared to non-radiative methods as shown in Table 2.1.

Radiative powering

In order to couple energy efficiently to the implant, its wavelength, regardless of the modality of the incoming wave must match the dimensions of the implant aperture. The aperture mismatch between the transmitter (large) and the receiver (small) that is usually apparent in the case of biomedical implants (i.e., less size constraints on the TX placed outside the tissue) affects efficiency primarily due to low achievable radiation resistance in the RX. In the case of small mm-sized implant, operation in far-field and increasing the frequency to the mm-wave ($>$ 10 GHz) regime can be shown to be the optimal frequency of operation [103]. Detailed analysis can also be found in [5]. Although increase in the operation frequency can enable high efficiency power transfer and allow on-chip integration of antennas to reduce overall footprint, designing high-performance circuitry at 10's of GHz with increasing passive losses is not trivial.

Also, note that with all types of EM methods, the necessity of in-vivo coils or antennas in such implants make them inherently MRI-incompatible, presenting a major hurdle for some applications.

2.1.2 Optical power transfer

Power transfer at higher frequencies, in the near infrared, infrared, and optical regime can also be used. Optical charging methods typically rely on a photovoltaic cell on the implant, which receives power from an external source (e.g., laser diodes, LEDs, etc.).

Photovoltaic cell is usually composed of a p-n junction of a large band-gap semiconductor, which generates electron-hole pairs from incident photons. The size of the photovoltaic cell is determined by the operation frequency of the optical powering method. Two loss mechanisms determine the optimal frequency of operation. On the one hand, as light propagates through the medium, wavelength dependent scattering from many different types of particles in the tissue. On the other hand, due to the multi-layer structure of the human tissue, reflections at multiple interfaces of the layer causes additional degradation in the transfer efficiency. Taking these loss mechanisms into account, studies have shown [4, 70] that near-infrared region (NIR) region (also known as "therapeutic window") in the optical spectrum has minimal overall loss and can therefore achieve maximal efficiency.

These methods, unfortunately, suffer from similar limitations of solar-power harvesting, such as inherent low efficiency in the photon-conversion and short penetration depth due to light attenuation in tissue.

2.1.3 Ultrasonic power transfer

Acoustic waves can transmit energy between two piezoelectric transducers. Acoustic energy transmission has been used for various military applications, such as underwater and through-wall communication [44, 78]. Unlike electromagnetics, using ultrasound as an energy transmission modality never entered into widespread consumer application, and was often overlooked because the efficiency of electromagnetics for short distances and large apertures is superior.

However, ultrasound offers an attractive alternative for wirelessly powering mm-sized or sub-mm implantable devices [18, 56, 64, 78, 96, 98]. Ultrasound has two advantages. First, the speed of sound is $10^5\times$ lower than the speed of light in water, leading to much smaller wavelengths at similar frequencies; this yields excellent spatial resolution at these lower frequencies as compared to EM waves. Second, ultrasonic energy attenuates far less in tissue than EM radiation; this results not only in much higher penetration depths for a given power, but also significantly decreases the amount of unwanted power introduced into tissue due to scattering or absorption. In fact, for most frequencies and power levels, ultrasound is safe in the human body. These limits are well-defined and ultrasound technologies have long been used for diagnostic and therapeutic purposes. As a rough guide, about $72\times$ more power is allowable into the human body when using ultrasound as compared to radio waves[4] [46, 47].

2.1.4 Survey

The performances of previously published work using various wireless powering options discussed in this section are listed in Table 2.1. The table is not meant to be used as a

[4]Time-averaged acceptable intensity for ultrasound for cephalic applications, as regulated by the FDA, which is approximately $9\times$ (94 mW/cm^2) for general-purpose devices and $72\times$ (720 mW/cm^2) for devices conforming to output display standards (ODS) compared to EM which is limited to 10 mW/cm^2 [46, 47].

Method	Dimensions	Freq	Efficiency	Ref
EM (Inductive)	TX coil: 64 mm RX coil: 22 mm	700 kHz	82% (Air, 20 mm) 72% (Air, 32 mm)	[86]
EM (Inductive)	TX coil: 43.7 mm RX coil: 17.8 mm	13.56 MHz	75% (Air, 10 mm) 58.2% (Tissue, 10 mm) 0.44% (Air, 50 mm) 0.16% (Tissue, 50 mm)	[111]
EM (Inductive)	TX coil: 28 mm RX coil: 34 mm	13.56 MHz	13.5% (Air, 20 mm)	[58]
EM (Mid-field)	TX coil: 210 mm RX coil: 2 mm	1.5 GHz	0.075% (Air, 15 mm)	[39]
EM (Far-field)	TX coil: N/A RX coil: 2.4 mm	24 GHz	8.9e-4% (Air, 280 mm) 2.8e-4% (Air, 500 mm)	[103]
EM (Capacitive)	Plates: 22 mm	402 MHz	68.3% (Gel, 3 mm) 67% (Gel, 5 mm)	[48]
Ultrasonic	TX: 15 mm RX: 15 mm	650 kHz	39.1% (Tissue, 5 mm) 17.6% (Tissue, 40 mm)	[79]
Ultrasonic	TX: 13 mm RX: 1.1 mm	1 MHz	$>$ 50% (Oil, 30 mm)	[18]
Ultrasonic	TX: 6.3 mm RX: 0.85 mm	1.8 MHz	25% (Gel, 9 mm)	[98]

Table 2.1: The performance of various wireless powering options discussed in this section are summarized. Dimensions are listed in terms of its effective diameter, defined as $\sqrt{\frac{4A}{\pi}}$ where A is the area of the coil.

comprehensive list but to illustrate appropriate use case for various powering modalities.

2.2 Benchmark

Despite significant progress in wireless power transfer, most work, as outlined in Table 2.1 focuses on cm-size or mm-size implants. In this section, we are interested in how the efficiency of traditional wireless powering methods scale for transferring power to sub-mm devices. In particular, we will illustrate the limitation of EM methods by considering the problem of transmitting EM power to a very small implant (sub-mm) embedded a very short distance (2 mm) in tissue (or in the neocortex), with mm-sized transmitter. Efficacies of other methods discussed above are not treated here but similar calculations can be performed to show their limitations.

In our calculations and simulations, we will focus specifically on whether EM wireless

powering can address the following objectives:

- What is the achievable power transfer efficiency?
- What is the absolute maximum power we can harvest safely at the implant?
- Does this approach scale to allow high density neural recording?

2.2.1 Simulation framework

Regardless of the specific implementation, any EM powered implant will contain a resonant component that couples to the EM waves; such a system can be modeled as a series/parallel RLC[5]. Assuming that the primary (TX) and secondary (RX) coils are perfectly aligned and that an implant can accommodate capacitance density[6] of approximately 10 fF/μm^2 and a planar square loop inductor is used, where the inductance is given by

$$L = \frac{1.27\mu_0 n^2 d_{avg}}{2}[ln(\frac{2.07}{\phi}) + 0.18\phi + 0.13\phi^2] \tag{2.1}$$

where n is the number of turns, d_o and d_i are the outer and inner diameter of the coil, respectively, $d_{avg} = \frac{d_i+d_o}{2}$ and ϕ is a parameter known as a fill factor, defined as $\frac{d_o-d_i}{d_o+d_i}$ [69]. In order to compute the expression for the efficiency of the EM link, it can be shown mathematically that the efficiency η (derivations can be found in [49]) is

$$\eta = \frac{k^2 Q_{TX} Q_L}{1 + k^2 Q_{TX} Q_L} \cdot \frac{Q_L}{Q_{RX} + Q_L} \tag{2.2}$$

where k is the coil coupling coefficient defined as $\frac{M}{L_{TX}+L_{RX}}$, M is the coil mutual inductance which depends on coil geometry and distance, L_{TX} and L_{RX} are the inductances of TX and RX, respectively, Q_{TX} and Q_{RX} are the unloaded quality factor of the TX and RX coil, respectively, and Q_L is the loaded quality factor of the RX coil.

2.2.2 EM channel model

The attenuation of the EM signal as it propagates through brain tissue due to tissue absorption is well documented [46] and the parameters can be extracted to model the transmission channel. Figure 2.1 plots the modeled channel (2 mm of tissue) loss as a function of frequency and includes loss from tissue absorption as well as path loss (or beam spreading) based on the Friis equation ($20\cdot\log(\lambda/(4\pi r)$). We observe that there is an exponential relationship between the channel loss and the frequency, and at 10 GHz – the total combined loss for one-way transmission is approximately 20 dB.

[5]For the purposes of this exercise, one may presume that a suitable method exists for modulating the quality factor or mutual coupling of the RLC as a function of neural activity

[6]Optimistic assumption given that the typical capacitor density for 65 nm technology node is between 2 – 3 fF/μm^2

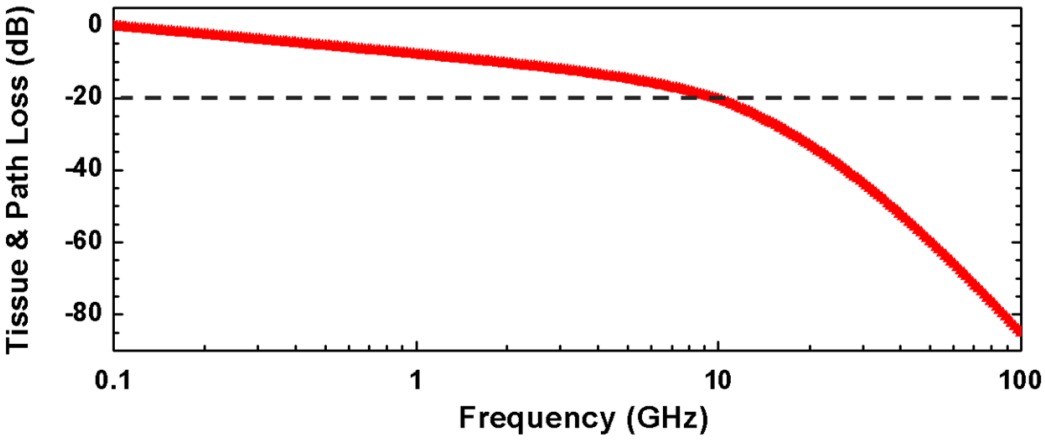

Figure 2.1: Total channel loss in 2 mm tissue, due to both tissue and propagation loss, increases exponentially with frequency, resulting in a 20 dB of loss at 10 GHz.

Moreover, at these very small footprints (compared to the wavelength, which is in millimeter range), the receive antenna efficiency becomes quite small, thereby easily adding roughly 20 dB of additional loss, resulting in a total gain of at most -40 dB. The tissue absorption loss penalty incurred by operating at a high frequency can be reduced by increasing the capacitance density using 3D inter-digitized capacitor layouts, for instance, but even then, eventual increase in the resonant frequency of the link causes an exponential increase in the tissue absorption loss and the overall channel loss.

2.2.3 Simulation result

An iterative solver that optimizes η in this channel model was written in MATLAB. Given this, the performance of electromagnetic power transfer suffers from two fundamental issues. First, the extreme constraint on the size of the node limits the maximum achievable values of the passives. Assuming a planar square loop inductor with 3-turn ratio, calculations predict the resonant frequency of a 100 μm neural dust would be $\sim$10 GHz as shown in Figure 2.2.

To make matters worse, the mutual coupling between the transmitter and receiver coils drops dramatically and significantly degrades the transfer efficiency and increases the sensitivity to misalignments [34, 92]. As shown in Figure 2.2, EM transmission with a 100 μm neural dust embedded 2 mm into the cortex results in 64 dB of transmission loss. Given a 1 mm^2 transmitter aperture outputting 100 μW of power – limited by the need to satisfy safety regulations on output power density[7] of 10 mW/cm^2 [46] – the resulting received power at the neural dust is $\sim$40 pW. This is orders of magnitude smaller than the power consumption imposed by noise requirements on the front-end amplification circuitry (refer

[7]Roughly, the upper limit for EM power density transiting through tissue is set by the minimum required to heat a model sample of human tissue by 1°C.

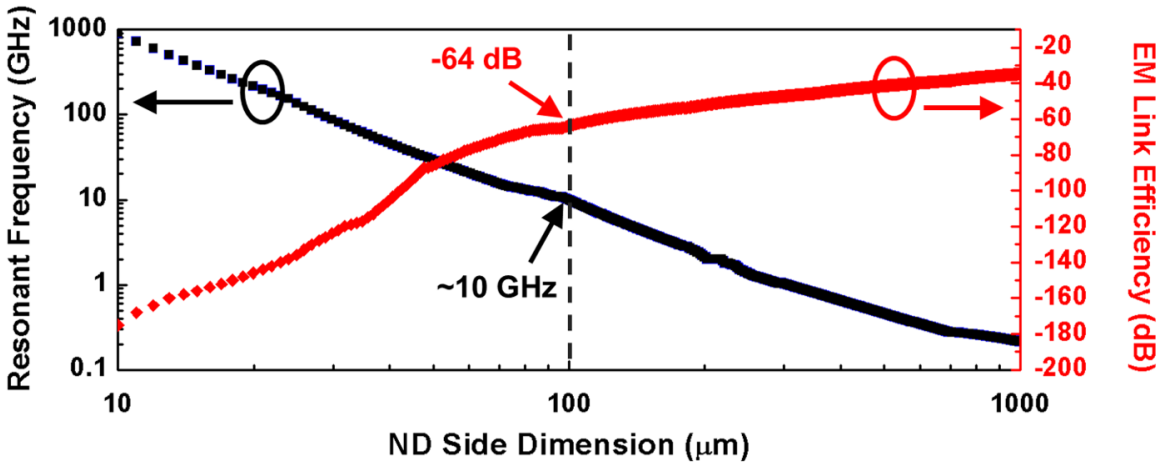

Figure 2.2: The mutual coupling, and therefore link efficiency, also reduces dramatically with the scaling of the implant dimensions.

to later sections for further discussion). As a result, prior work by [10], which features the most energy-efficient and smallest wirelessly EM powered neural recording system to date, at 2.5 μW/channel and 250 μm $\times$ 450 μm, is limited in terms of further dimensional scaling and increasing the range (the effective range within brain tissue for this work was 0.6 mm).

We conclude that due to the non-linear interplay of form factor, speed of light, and frequency spectra of tissue absorption, EM power transmission is not an appropriate energy modality for the powering of 10's of μm sized neural dust implants.

2.3 Conclusion

In this chapter, we examined a number of wireless powering techniques to couple energy to sub-mm sized implants. In particular, we evaluated scaling of commonly used electromganetics (EM) based approaches, but due to the inherent mismatch in the wavelength and the size of the implant, along with limited output power due to safety, EM-based WPT cannot provide sufficient power to sub-mm sized implants. According to Table 2.1, ultrasound appears to be a promising alternative that scales more favorably than EM. We will introduce a novel neural interface system based on ultrasonic power transfer and communication in the next chapter.

Chapter 3

Neural Dust: Distributed, Ultrasonic Backscattering System

In this chapter, we present a neural recording platform built from low-power electronics coupled with ultrasonic power delivery and backscatter communication. The system, called *neural dust* is an ultra-miniature, compliant, and distributed system that can enable significant scaling in the number of neural recordings from the nervous system. This can be achieved via two fundamental technology innovations: (1) 10 – 100 μm scale, free-floating, independent sensors (or neural dust motes) that detect and report local extracellular electrophysiological data, and (2) a transceiver[1] that establishes power and communication links with the neural dust mote. We examine both the theoretical foundation and fundamental system design trade-offs of neural dust and experimental verification of the predicted scaling effects.

3.1 Ultrasonic power link model

The design of neural dust is heavily constrained in both size and available power to the implant. As a result, it is imperative to accurately model the transmission channel to maximize the power efficiency.

3.1.1 Piezoelectric materials

Piezoelectricity refers to the phenomenon present in certain solid (usually crystalline) materials where there is an interaction between the mechanical and electrical states. For a crystal to exhibit the piezoelectric effect, its structure should have no center of symmetry, i.e., anisotropic, such that a stress (tensile or compressive) applied to such a crystal will

[1] In the context of recording from the central nervous system (CNS), it will be placed beneath the skull, i.e., sub-cranially, in order to avoid strong attenuation of ultrasound by bone and powered by an external reader via EM power transfer.

alter the separation between the positive and negative charge sites in each elementary cell, leading to a net polarization at the crystal surface. The effect is practically linear in linear elastic solids and governed by

$$T = cS + hE \tag{3.1}$$

$$D = \epsilon_r R + hS \tag{3.2}$$

where h is the piezoelectric coupling coefficient, strain (S) and stress (T) are related by the elastic stiffness (c) and the electric displacement (D) is related to the electric field (E) by the permittivity (ϵ_r) of the material.

Piezoelectric materials can transduce electrical energy into mechanical energy and vice versa by changing lattice structure, and this state change is accessible via either electrical stimulation or mechanical deformation. There is a wide range of piezoelectric materials, each suitable for different applications. Several parameters, such as piezoelectric strain constant (d-coefficient), piezoelectric voltage constant (g-coefficient), mechanical quality factor (Q), electromechanical coupling factor (k), etc. can be used to compare different piezoelectric materials while selecting for a specific application. In particular, k is the measure of conversion efficiency between mechanical and electrical energy and often higher k is desired.

As an example of choosing appropriate material, piezoelectric polymer compounds such as polyvinylidene (di)fluoride (PVDF) are primarily used to construct broadband, high-sensitive hydrophones due to their low quality factor and high piezoelectric voltage constant (g-coefficient). On the other hand, ceramic compound known as lead zirconate titanate (PZT) is a popular choice for high-power, high-performance, narrowband diagnostic ultrasonic imaging due to its greater sensitivity, higher operational temperature, and exceptional electromechanical coupling coefficient (k). When used in-body, however, the lead content of PZT makes it difficult to introduce into human tissue in chronic applications. A number of alternative, implantable piezoelectric materials, such as barium titanate ($BaTiO_3$), aluminum nitride (AlN) and zinc oxide(ZnO) [83], exist with material properties slightly inferior to PZT. As a result, initial study of the link efficiency assumes the use of $BaTiO_3$. Given the relative ease of obtaining PZT crystals with varying geometry and encapsulating it in biocompatible encapsulant[2], experiments were carried out with PZT.

3.1.2 Piezoelectric transducer model

Due to the importance of piezoelectric transducers in various applications, there are a number of equivalent circuit models to describe the electromechanical operation of a 1D piezoelectric crystal.

The KLM model by Krimholtz, Leedom, and Matthaei is arguably the most common equivalent circuit and is a useful starting point to construct a full link model with the intent

[2]PDMS silicone or UV-curable medical-grade epoxy is used to enable short-term implantation of PZT-based implant. Its effects are further discussed in subsequent sections.

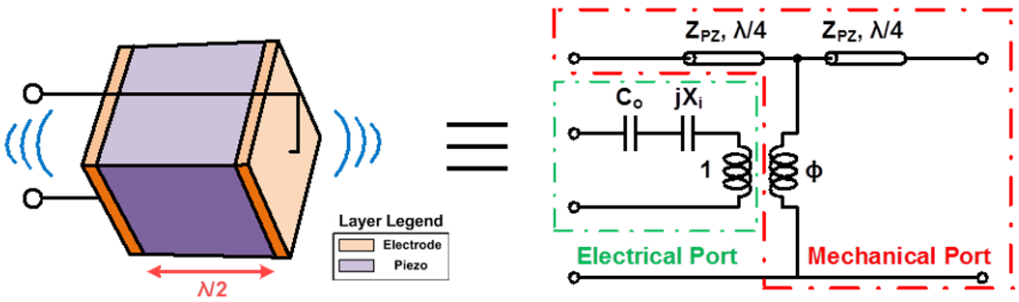

Figure 3.1: KLM model of a neural dust piezoelectric transducer, showing one electrical port and two mechanical ports. Coupling between the domains is modeled with an ideal electromechanical transformer.

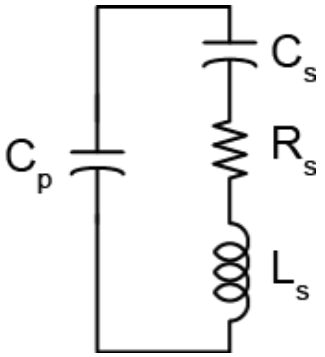

Figure 3.2: Transducer model can be simplified to a 1D series circuit model around the fundamental resonance.

of examining scaling and system constraints [54]. The basic model, shown in Figure 3.1, includes a piezoelectric transducer with electrodes deposited in parallel to the poling direction of the transducer. Across a wide range of frequencies, the entire transducer is modeled as a frequency-dependent three-port network, consisting of one electrical port (where electric power is applied or collected) and two acoustical ports (where mechanical waves are produced or sensed from the front and back faces of the transducer).

The parallel-plate capacitance due to the electrodes and the frequency-dependent acoustic capacitance are modeled as C and X_i, respectively, and the transduction between electrical and mechanical domains is modeled as an ideal electromechanical transformer with a turn ratio of Φ, connected to the middle of a transmission line of length $\lambda/2$, as shown in Figure 3.1. Assuming an infinite 2D plate piezoelectric transducer of thickness t, the resonant frequency is set by $t = \lambda/2$; at the resonant frequency, the ultrasound wave impinging on either the front or back face of the transducer will undergo a 180° phase shift to reach the other side, causing the largest displacement between the two faces. This observation implies that phase inversion only exists at the odd harmonics of the fundamental mode in a given geometry. Near the resonant frequency of a piezoelectric transducer, KLM model can be simplified to

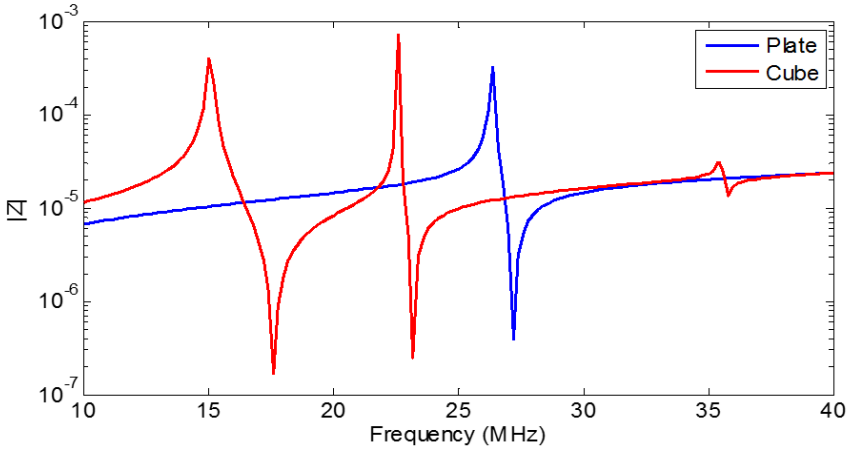

Figure 3.3: COMSOL simulation exhibits a resonant shift and spurious tones present in the frequency spectra of a cubic transducer.

the resonance model[3] as shown in Figure 3.2.

However, both models are derived under the assumption of pure one-dimensional thickness vibration, and therefore can only provide a valid representation for a piezoelectric transducer with an aspect ratio (w/t) greater than 10^4 that mainly resonates in the thickness mode where w and t are width and thickness of piezoelectric material, respectively [89]. Given the extreme miniaturization target for the neural dust, a cube dimension (aspect ratio of 1:1:1) is a better approximation of the geometry than a plate (aspect ratio > 10:10:1). Due to 2D effects, such as Poisson's ratio and the associated mode coupling between resonant modes along each of the three axes of the cube, changing aspect ratio alters the resonant frequencies among other parameters [41]. The piezoelectric transducers for both the transceiver and the neural dust mote must be designed to resonate at the same frequency to maximize the link efficiency. In the model below, we assume the neural dust motes are cubic and the transceiver is approximately planar (i.e., 2D).

In order to obtain an accurate estimate of KLM parameters for the piezoelectric transducer in the neural dust mote, we simulated a cube transducer using a 3D finite element package (COMSOL Multiphysics, Acoustic Module) to model anisotropies, resonant frequency shift, and mode coupling between several resonant modes. The resonant frequency of a 100 μm thick $BaTiO_3$ is shown in Figure 3.3. The effect of decrease in resonance by a factor of 1.7 is included in the modified KLM model by extracting the effective acoustic impedance of the neural dust mote from COMSOL. To match the resonant frequency of the transceiver and the neural dust mote, the thickness of the transceiver is varied to match the

[3]Since the model has both series and parallel resonances, there are both series resonance (short-circuit resonance or simply resonance) and parallel resonance (open-circuit resonance or anti-resonance). This will be evident in piezoelectric transducer measurement in subsequent sections and the separation between the two peaks will determine the Q of the resonator.

[4]Alternatively, where w/t is less than 1/10.

fundamental thickness mode of the neural dust. Approximately 66 % of the total output energy is contained in the main thickness resonance; this is modeled as a loss term. For $BaTiO_3$, coupling to other modes can be reduced by stretching it in the [110] direction because $BaTiO_3$ is both anisotropic and partially auxetic, exhibiting negative Poisson's ratio and therefore providing gain when stretched [6].

3.1.3 Mote placement

As the pressure field generated by a uniform continuous-wave excited piezoelectric transducer propagates through the tissue medium, the characteristics of the pressure field change with distance from the source. The varying field is typically divided into two segments, *near field* and *far field*. In the near field, the shape of the pressure field is cylindrical and the envelope of the field oscillates. At some point distal to the transducer, however, the beam begins to diverge and the pressure field becomes a spherically spreading wave, which decays inversely with distance. The transition between the near and far field is where the pressure field converges to a natural focus, and the distance at which this occurs is called the Rayleigh distance, defined as,

$$L = \frac{(D^2 - \lambda^2)}{4\lambda} \approx \frac{D^2}{4\lambda}, D^2 \gg \lambda^2 \tag{3.3}$$

where D is the aperture width of the transmitter (or transceiver) and λ is the wavelength of ultrasound in the propagation medium. In order to maximize the received power, it is preferable to place the receiver at one Rayleigh distance where the beam spreading is at a minimum. Therefore, with 2 mm of transmission distance assumed in the context of interrogating an implant in the cortex and a resonant frequency of 15 MHz ($\lambda = 100$ μm), the maximum dimension of the transceiver should be $\sim$1 mm.

3.1.4 Complete link efficiency parameters

A good model of the ultrasonic channel is crucial in order to assess the tradeoffs in optimizing systems for energy transfer through lossy brain tissue. The complete energy link model is shown in Figure 3.4 and can be divided into three parts: (1) the ultrasonic transceiver or *transmitter*, (2) tissue, and (3) the neural dust mote or *receiver*. A signal generator and amplifying stages produce power for the ultrasonic transmitter through an impedance matching circuit that provides conjugate matching at the input. The ultrasonic wave launched by the transceiver penetrates tissue, modeled as a lossy transmission line, and a fraction of that energy is harvested by the ultrasonic receiver, or neural dust mote. We evaluate embedding the receiver up to 2 mm into the tissue, which generates an AC voltage at the electrical port of the piezoelectric transducer in response to the incoming ultrasonic energy.

In order to compute the link energy transfer efficiency, the model can be decomposed to a set of linear and time-invariant two-port parameters, representing a linear relationship between the input and output voltage. Here, we choose to represent the input-to-output

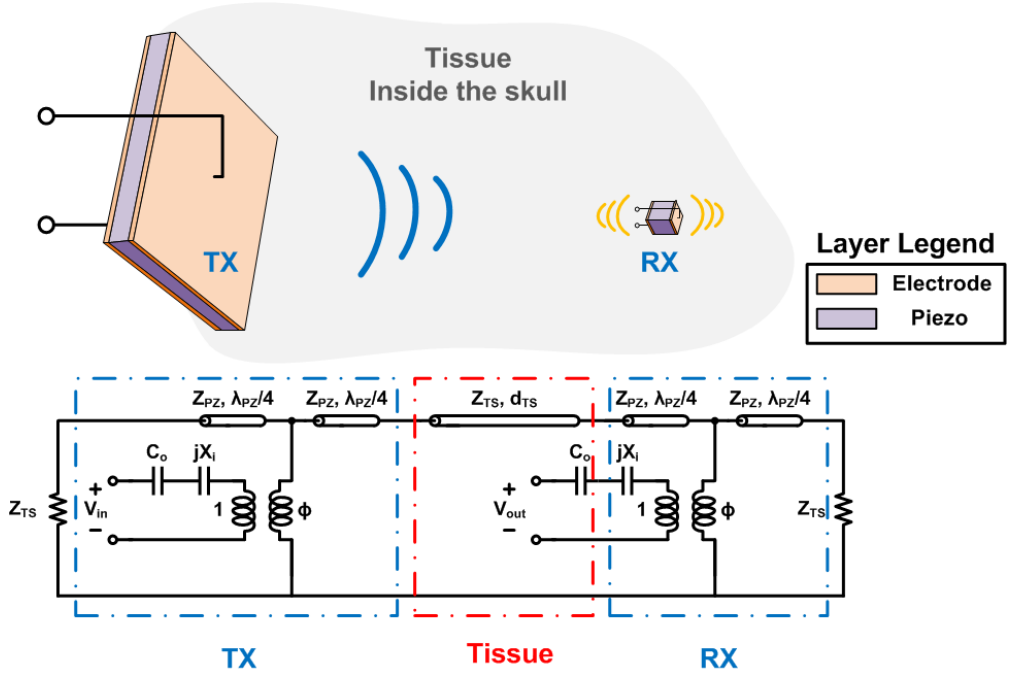

Figure 3.4: Complete single interrogator, single neural dust power and communication through link models.

relationship using ABCD parameters, which simplify analysis of cascades of two-port networks through simple matrix multiplication [82]. By representing the link model with the two-port network, we can come to conclusions concerning optimal power transfer efficiency (or "gain").

We can define power gain in many forms: transducer gain (G_t), power gain (G_p), available gain (G_a), and maximum gain (G_{max}). The distinction among these figures of merit results from the designers' ability to vary either input (transceiver) or output (neural dust) impedance or both. In a two-port network, the maximum power gain, denoted G_{max}, is achieved when a designer can conjugate match both the input and output impedances to source and load impedances, respectively. In the scenario that a designer can only adjust load impedance, source impedance, or neither, G_a, G_p, and G_t, respectively, are appropriate figure of merits. Note that $G_{max} \geq G_p$, $G_a \geq G_t$.

However, with a 100 μm neural dust mote, the output impedance level is such that in order to electrically match, it would require $\sim$100 μH of inductance to perfectly conjugate match the output of the two port link network. Given the compact form factor of the neural dust, it is completely infeasible to obtain such inductance with electrical means, and therefore G_{max} is an unachievable figure of merit. It may be possible to approach G_{max} by mechanical means such as the addition of material layers that perform an acoustic impedance transformation, or similarly, by electromechanical means such as utilizing micromachined acoustic resonators, but these add significant complexities in integration and packaging.

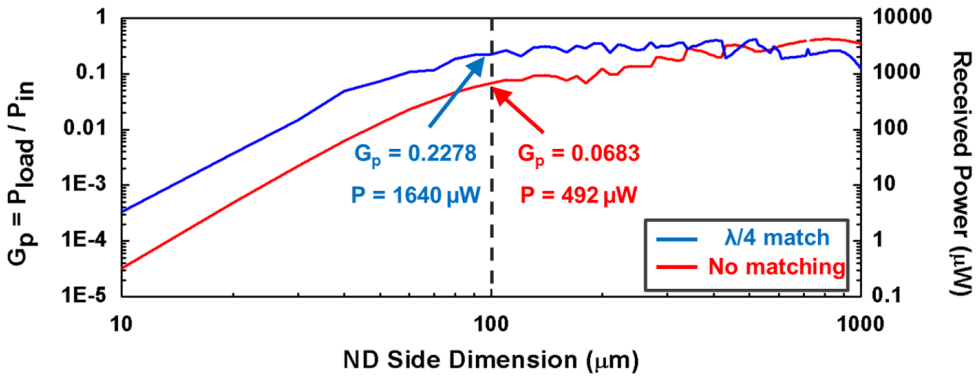

Figure 3.5: Link efficiency with and without a $\lambda/4$ mechanical matching layer as a function of the neural dust side dimension shows that a significant amount of energy can be harvested by the mote, even at 10's of μm's of dimensions. At the resonant frequency, ultrasonic link efficiency is $> 10^7$ more than EM transmission with 100 μm mote dimension.

Therefore, for comparison and scaling analysis, we assume we only have impedance control at the input, or the transceiver side, and therefore, power gain (G_p) is the suitable figure-of-merit.

3.1.5 Simulated link efficiency

The complete link model in Figure 3.4 with $BaTiO_3$ is implemented in MATLAB with the limitation of the KLM model (as outlined in previous subsection) corrected via COMSOL simulations. Given a 1 mm^2 transceiver, Figure 3.5 plots both the efficiency of the link and the received power at the neural dust mote as the size of the mote scales and the thickness of the transducers in the transceiver is adjusted to match the resonant frequency of the dust and the tissue, i.e., transmission line resonator. We note that the maximum efficiency of the KLM-adapted link model, where the transceiver is fully immersed in the tissue medium, is limited to 50% because both the back and front side of the interrogator are loaded by the tissue layer. We can direct the majority of the acoustic energy towards the front side (i.e., side facing the tissue), by loading the back side with either much lower or a much higher acoustic impedance compared to that of the tissue. Backing is generally done using a material with high attenuation and high density or air, which exhibits acoustic impedance ($\sim$400 Rayls) which is several orders of magnitude smaller than that of soft tissues ($\sim$1.5 MRayls) and $BaTiO_3$ ($\sim$30 MRayls). Using air as the backing material simplifies packaging [18].

Additionally, in order to maximize the link efficiency, proper impedance matching at the front side of the transceiver is needed to avoid significant reflection due to large impedance match between $BaTiO_3$ and soft tissue. Depending on the thickness of the neural dust mote and the resonant frequency of the network, ultrasonic wave launched by the transceiver

undergo varying phase changes through the lossy tissue. Thus, the efficiency of a system with smaller dust motes can be improved if the total propagation distance happens to be a multiple of a wavelength of the ultrasound. As a result, for dust motes greater than 100 μm, we note that the efficiency does not monotonically increase with the dimension. On the other hand, for a dust mote that is less than 100 μm in dimension, because the wavelength associated with the network's resonant frequency is much smaller than its tissue propagation distance, the link efficiency depends more heavily on the cross-sectional area of the dust. Therefore, we note that the efficiency will drop at least quadratically with the reduction of dust dimension. The efficiency of the link can be improved with a $\lambda/4$ matching layer for impedance transformation, but the improvement is limited due to the loss from the material (e.g., attenuation of graphite epoxy is $\sim$16 dB/(cm·MHz) [67] compared to that in brain tissue which is 0.5 dB/(cm·MHz) [43]) as shown in Figure 3.5. Note that for the case with this matching layer, the efficiency is worse for dust motes that are > 500 μm since the loss of the matching layer outweighs that of the tissue.

More specifically, simulation of the complete link indicates that for a 100 μm mote embedded 2 mm into the brain, ultrasonic power transmission can enable 7% efficiency power transmission (-11.6 dB). At the resonant frequency, we can receive up to $\sim$500 μW at the neural dust mote (resulting in nano-meters of total displacement) with a 1 mm^2 interrogator, which is $> 10^7$ more than EM transmission at the same size scale (see Chapter 2). Furthermore, scaling of neural dust also indicates that approximately 3.5 μW can be recovered by a dust mote as small as 20 μm through ultrasonic transmission, which is still in the realm of feasibility to operate a state-of-the-art CMOS neural front-end.

3.1.6 Scaling Limit

Free-floating extracellular recording at untethered, ultra-small dust motes, however, poses a major challenge in scaling. Unlike the needle-like microelectrode shanks that can measure time-domain electrical potential at each recording site in relation to a common electrode, placed relatively far away, both the recording and the common electrode must be placed within the same (very small) footprint. Although the two are interchangeable, the separation and therefore, the maximum differential signal between the electrodes are inherently limited by the neural dust footprint, and follow the dipole-dipole voltage characteristic that decreases quadratically[5] with increasing separation distance. Since the power available to the implant has a fixed upper bound, the reduction of extracellular potential amplitude as the neural dust dimensions are scaled down in the presence of biological, thermal, electronic, and mechanical noise (which do not scale), causes the signal-to-noise (SNR) ratio to degrade significantly. This places heavy constraints on the CMOS front-ends for processing and extracting the signal from extremely noisy measurements. Therefore, if we consider sufficient SNR at the

[5]Unless very near a cell body, in which case it appears to scale exponentially; see [36] for a more thorough review

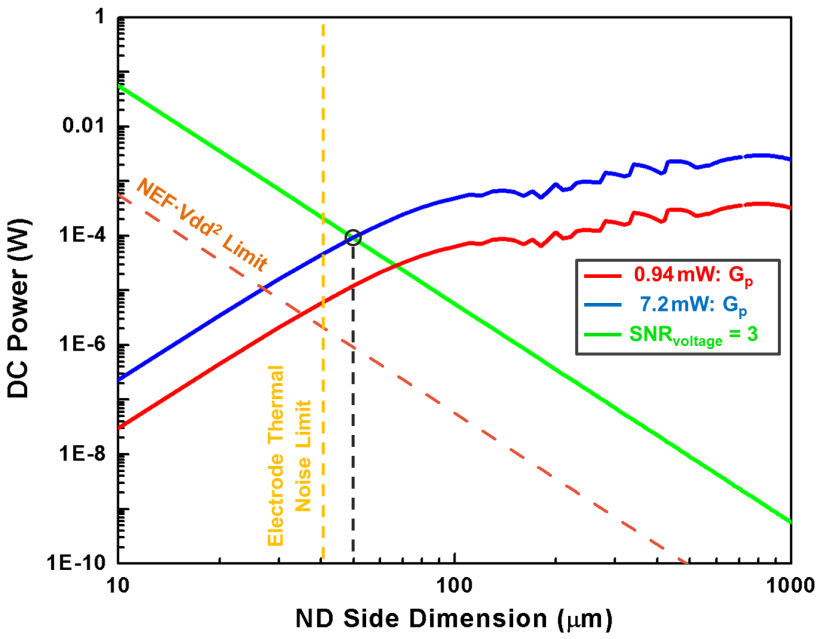

Figure 3.6: As we scale down the neural dust size, more power is needed to keep the noise floor down to maintain SNR while less power is captured. The intersection of these two trends is the smallest mote that will still operate. Scaling with an SNR of 3 shows operation down to 50 μm. The analysis assumes the use of $BaTiO_3$ and two different FDA-approved ultrasonic energy transfer protocols, and does not include the use of matching layers.

input of the neural front-ends as one of the design variables, the scaling of neural dust as depicted in Figure 3.5 must be revisited.

Focusing specifically on the scaling of a cubic neural dust, we run into the inherent limitation in the maximum achievable differential signal discussed above. At a separation distance of 100 μm between recording electrodes, we expect a 10 μV action potential (AP) amplitude[6] with the amplitude further reducing quadratically as the separation is reduced. Since the power available to the neural dust is limited, the design goal of a front-end architecture is to minimize the input-referred noise within this power budget. The power efficiency factor ($\text{NEF}^2 \cdot V_{dd}$) quantifies the tradeoff between power and noise [71] and extrapolating from the measurement result of a previous CMOS neural front-end design ($\text{NEF}^2 \cdot V_{dd}$ of 9.42 [10]), we can estimate the relationship between the input-referred noise level and the DC power consumption of an optimally designed front-end architecture as we scale. The fundamental limit to the $\text{NEF}^2 \cdot V_{dd}$ occurs at a supply voltage of at least $\sim 4\ k_B T/q$ or 100 mV, in order to reliably operate the FET, and by definition, the NEF of 1 for a single BJT amplifier [100]. In principle, one could push the supply voltage down to $\sim 2\ k_B T/q$, but in practice 100 mV is already extremely aggressive.

[6]Data is derived from [27]

Fixing the input SNR to 3, which should be sufficient for extracting neural signals, we can evaluate the scaling capability of neural dust as shown in Figure 3.6. We assumed the use of $BaTiO_3$ in the model described in the section above and do not include the use of matching layers. We also assumed that the transceiver's output power is constrained by the two different FDA-approved ultrasonic energy transfer protocols. We note that there exists an inherent tradeoff between the power available to the implant and the exponential increase in the power required to achieve an SNR of 3 with the reduction of spacing between the electrodes. The point of intersection in Figure 3.6 denotes the minimum size of neural dust that enables the operation of the complete link. For the stated assumptions, this occurs at 50 μm, which is greater than the dimension at which the thermal noise from the electrode (R = 20 kΩ and BW = 10 kHz) limits further scaling. This effectively means that, staying within FDA-approved ultrasound power limits, assuming an SNR of 3 is required, neural dust motes smaller than 50 μm cannot receive enough power to distinguish neural activity from noise. Note that the cross-over assumes 100 % efficiency in the rectifier and zero overhead cost in the remaining circuitry, both of which will not be true in practice (i.e., the actual size limit will be larger than this).

3.2 Ultrasonic backscatter communication

Given the stringent requirements on both the size and power, broadcasting neural recording data from the dust motes to the transceiver by building a fully active transmitter onto the tiny mote is infeasible from both power and size standpoint. Therefore, we adopt a communication method called *backscattering*, commonly used in radio frequency identification (RFID) technologies [31]. In RFID, *passive* and *semi-passive* sensor tags transmit the data by modulating the incoming RF energy (from which it harvests sufficient energy to operate the electronics) and re-radiating the modulated RF energy back to the reader. This modulation of the backscattered RF energy can be achieved by varying the load impedance, which changes the coefficient of reflectivity[7]. Backscatter communication is a more attractive choice than building a fully active transmitter on the implant because it does not need batteries or significant capacitive energy storage, thus extending lifetimes, eliminating the risk of battery leakage, and removing the significant impediment to size scaling that would be created by the dramatically reduced capacitance available on a small mote. Since this scheme can be applied to any link, regardless of the transmission channel modality, we investigate this strategy in the context of neural dust.

3.2.1 System consideration

Generally, the CMOS component of an active neural dust mote consist of at least a full-wave bridge rectifier to convert the harvested piezoelectric AC signal to a DC level and regulators to generate a stable and appropriate DC supply voltage for the rest of the CMOS

[7]Modulation can be encoded in amplitude, frequency, and/or phase of the impinging wave.

circuitry. The basic architecture of the CMOS front-ends will depend on the application. For the acquisition of the entire neural signal trace, we must capture both the LFP and action potentials. Given the relative amplitude, DC offset, and frequency range of these signals, the circuit must operate at a full bandwidth of 0 to 10 kHz with > 70 dB of input dynamic range [71]. Researchers have demonstrated a mixed-signal data acquisition architecture solution to extract LFP and action potentials, originally proposed in [71], which cancels the DC offset in the analog domain to alleviate the dynamic range constraints and to eliminate bulky passive components used in [112]. Therefore, the CMOS front-ends include rectifiers, voltage regulators, low-noise amplifiers, DC-coupled analog-to-digital converters (ADC) and modulators to communicate the decoded information back to the transceiver.

Co-integration and packaging challenges and – most importantly – the footprint of current CMOS neural front-ends present major roadblocks to the active implant approach. The smallest CMOS neural front-end system published to date, not including rectifiers and modulators, occupies approximately 100 μm of silicon real estate [71], and packing the same functionality onto a smaller footprint may not be plausible. Thinned, multi-substrate integration to meet the volume requirements while keeping the overall CMOS area constant may resolve this issue, but requires substantial further technology development to represent a viable solution. Scaling the active electronics to appropriate dimensions is clearly a bottleneck, but presents an enticing opportunity for further innovation to address the issue.

Ideally, the simplest neural dust mote would consist of a piezoelectric transducer with a set of surface electrodes that can record the occurrence of a neural spike, and the extracted measurement can be reported back to the transceiver by somehow encoding the information on top of the incoming ultrasound wave. The design methodology we adopt here is that of elimination: starting with current neural front-end architectures that consist of, but are not limited to, rectifiers, high-resolution ADC, amplifiers, regulators and modulators, we start eliminating each component to truly understand its impact on overall system performance, and therefore assess its necessity for inclusion on the dust mote itself. Rectifiers and voltage regulators are essential to provide a stable DC power supply for the transistors in the system. In order to prevent variations in the electrical response of the circuits with the variation of its power supply, it is important to have sufficient amount of capacitance to curb any supply ripple and filter out high frequency electrical noise. As a result, these two components tend to occupy the largest amount of space in the CMOS die footprint.

3.2.2 Simplified circuit implementation

Here, let us re-examine the need for a DC supply as we entertain the idea of completely eliminating both the rectifiers and the voltage regulators. In this scenario, the piezoelectric transducer harvests the incoming ultrasonic wave and directly converts it to an AC electrical voltage. At this point, the design goal essentially boils down to devising ways of encoding neural data on top of this incoming ultrasound wave, to be reported back to the transceiver via modulation.

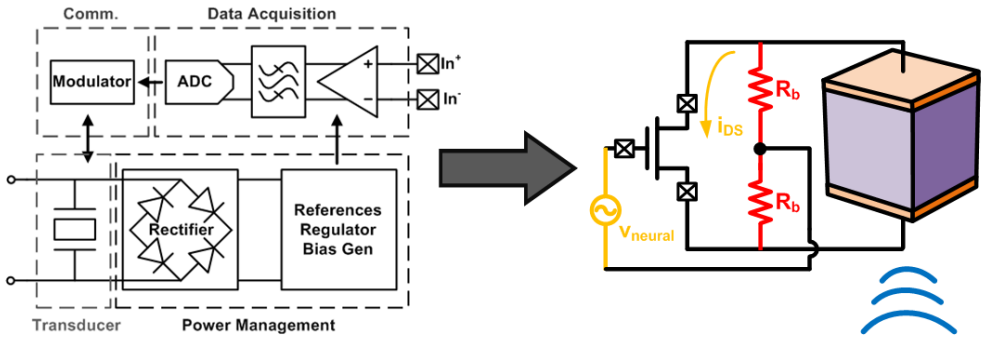

Figure 3.7: A process of elimination leads to a simple architecture (right) where we utilize a FET to vary the electrical load impedance, changing the ultrasonic wave reflectivity at the dust and modifying the backscattered wave.

We propose an implementation shown in Figure 3.7, where the drain (D) and source (S) of a single field-effect transistor (FET) sensor are connected to the two terminals of a piezoelectric transducer while the FET modulates the current I_{DS} as a function of a gate (G) to source voltage, V_{GS}. In this scheme, given that the supplied V_{DS} of the FET is an AC voltage that swings both positive and negative, the body (B) of the FET must be biased carefully. Normally, for a n-channel FET, the body is connected to the source voltage to prevent the diode at the B-S and B-D junctions from turning on. However, keep in mind that since a FET is a symmetric device, the source and drain are defined only by which terminal is at a lower potential. Therefore, the electrical source/drain terminals, or left/right for disambiguation (from a cross section of a FET), swap physical sides every half cycle of the harvested AC waveform. As a result, simply shorting the body to either physical terminal of the FET causes the diode formed at the B-S and B-D junctions to be forward-biased, so care must be taken to avoid neural signal from modulating the incoming sinusoid only half of the cycle.

As a result, we propose an alternative biasing scheme for the FET to modulate the entire sinusoid as shown in Figure 3.7. The resistors R_b act to cause the neural potential to appear between the gate and both of the left/right terminals of the transistors while superimposing the AC waveform from the ultrasonic transducer across these same two terminals. In this manner, even though the electrical source/drain terminals swap every half cycle, during both halves of the cycle the V_{GS} of the FET is modulated by the neural signal.

The circuit achieves this superposition by relying on the fact that the neural signals occupy a much lower frequency band than the ultrasound, and that the ultrasound transducer itself has a capacitive output impedance (C_{piezo}). Thus, R_b should be chosen so that $1/(R_b \cdot C_{piezo})$ is placed well above the bandwidth of V_{neural} (> 10 kHz) but well below the ultrasound frequency ($\sim$10 MHz). R_b along with the transistor width must also be chosen carefully to achieve the best reflectivity, as will be described shortly.

Since modulation of I_{DS} in turn modulates the impedance seen across the two piezoelec-

tric drive terminals, the FET effectively modulates the backscattered signal seen by a distant transmitter. The change in the nominal level of I_{DS} is a function of V_{GS}, which can be up to 10 μV (V_{neural}) for a 100 μm dust mote near an active neuron. The sensitivity, S, to the action potential, then, is defined as the change in I_{DS} with respect to V_{GS} normalized by the nominal I_{DS} (in addition to the current through R_b) and V_{neural},

$$S = \frac{V_{neural}}{I_{DS} + V_{DS}/2R_b} \cdot \frac{\partial I_{DS}}{\partial V_{GS}} = V_{neural} \cdot \frac{g_m}{I_{DS} + V_{DS}/2R_b} \tag{3.4}$$

Since g_m (transconductance of a FET) is directly proportional to I_{DS}, in order to maximize g_m/I_{DS} (i.e., achieves the largest g_m for a given I_{DS}), we would like to operate the FET in its steepest region – specifically, deep sub-threshold where it looks like a bipolar junction transistor (BJT). Therefore, the nominal V_{GS} bias can be 0 V, which simplifies the bias circuitry. The modulation of the current is equivalent to a change in the effective impedance of the FET, or the electrical load to the piezoelectric transducer. This variation in the load impedance affects the ultrasonic wave reflectivity at the neural dust and modifies the wave that is backscattered. Note that in order to maximize the sensitivity (i.e., operating the transistor in deep sub-threshold), the system should be constrained such that the piezoelectric voltage is never too large compared to the threshold voltage.

A SPICE simulation of a typical low-threshold voltage n-channel FET in a standard 65 nm CMOS technology was used in order to assess the nominal current level and the change in the effective impedance of the electrical load with V_{neural}. We assumed that we can implement suitably large R_b in sufficiently small area of the neural dust motes. As previously mentioned, in deep sub-threshold, the FET behaves as a BJT, where the physical limit on the achievable $g_m/I_{DS} = q/k_BT$, determined by the Boltzmann distribution of carriers. As a result, we can obtain S = 400 ppm for $V_{neural} = 10$ μV with a perfect BJT. Given the non-ideality factors associated with FETs, the sensitivity is reduced by a factor of 1.5 – 2, to roughly 250 ppm, which is confirmed by the simulation.

The implication of the modification in the electrical properties of the n-channel FET (output load of the piezoelectric transducer) on the change in the acoustic signal and the corresponding design specifications for the transceiver is discussed in detail below.

3.2.3 Transceiver receive sensitivity

A different set of challenges exist in implementing circuitry to generate, collect and process neural data. Namely, innovative approaches are essential to (1) ensure that the transceiver/sensor combination has sufficient sensitivity to meet the necessary data resolution and (2) allow for combination of various multi-mote interrogation strategies to distinguish among different neural dust motes. Techniques for multi-mote interrogation are detailed in Chapter 5.

We assume that the power and size constraints of the neural dust, and not the transceiver, are the major bottlenecks in the scaling of ultrasound-mediated neural dust system. In order to verify the validity of this assumption, we can examine, to the zeroth order, the power required by the transceiver to achieve certain receiver sensitivity for a passive implementation

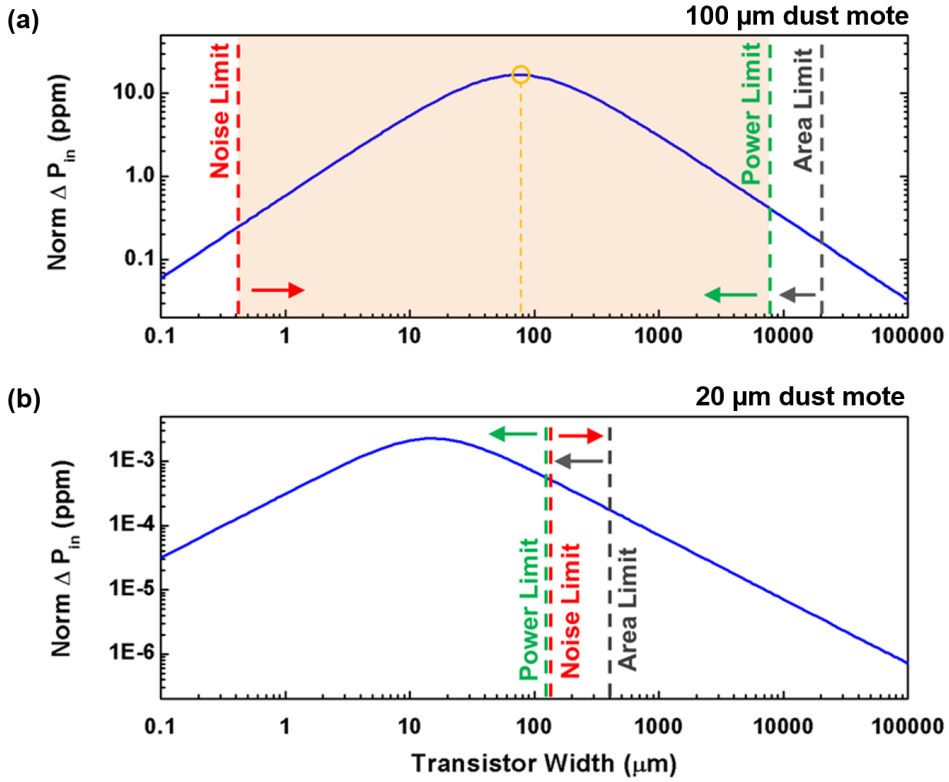

Figure 3.8: Change in the input power level (i.e., power at the transceiver) as a function of transistors width for a 65 nm CMOS process and with (a) 100 μm and (b) 20 μm neural dust motes.

of the neural dust mote. From the complete link model shown in Figure 3.4, we note that the change in the electrical impedance of the n-channel FET load induces a change in the input admittance (or the input power) of the two-port network. The transceiver (as a receiver) must be able to detect this change in the input power level in order to resolve the occurrence of a neural spiking event. Therefore, we need to determine the size of the FET sensor on the dust mote that maximizes this change in the input power level of the two-port network, or,

$$\Delta P_{in} \propto \left| \frac{Y_{in,spike} - Y_{in,nom}}{Y_{in,nom}} \right| \tag{3.5}$$

where $Y_{in,spike}$ and $Y_{in,nom}$ denote input admittance of the two-port network with and without a neural spike, respectively. Figure 3.8 shows the result of the optimization problem with a standard 65 nm CMOS technology. For 100 μm and 20 μm dust motes, 75 μm and 16 μm width FET maximize ΔP_{in}, respectively. Note that since the optimum transistor width (i.e., nominal impedance) for achieving the largest reflection is pretty flat, passive neural dust system is insensitive to the effects of threshold variability in the transistors and DC offsets in the neural electrodes.

The FET sensor design variable (transistor width), however, is constrained due to the thermal noise of the FET (which sets the lower limit) and the maximum available power at the mote and the neural dust form factor (which set the upper limits). Clearly, the small footprint of the neural dust restricts the maximum effective width of the FET sensor that we can pack on the dust, and we term this the *area limit*. More importantly, we need to ensure that the thermal voltage noise of the FET does not overwhelm the AP voltage. As a result, for a fixed bandwidth, in order to lower this voltage noise floor of the FET, it is necessary to increase the bias current, and hence the power consumption given a fixed output voltage. Given a simple single-ended transistor amplifier with a single dominant pole, a bias current of I_{DS}, and a transconductance of g_m, the minimum bias current required can be derived as

$$I_{DS} = \frac{\pi}{4} \cdot \frac{4k_BT}{v_n^2} \cdot \frac{k_BT}{q} \cdot BW \tag{3.6}$$

where v_n^2 is the input-referred voltage noise. As a result, the FET must be large enough to be able to sustain this minimum bias current. Therefore, for a BW = 10 kHz and voltage SNR at the input of the FET of 3 (which sets v_n^2 based on V_{neural}), we can compute the minimum allowable size of the FET, restricted by the *noise limit*. Finally, in order to reliably operate the FET, the drain-source voltage of the FET must be at least $\sim$4 k_BT/q or 100 mV. As a result, neural dust must capture enough power from the transceiver to sustain both 100 mV and the minimum current required to ensure that the thermal noise does not dominate the AP voltage. This is defined as the *power limit*.

With such restrictions, Figure 3.8 shows that for a 100 μm dust mote, we can design a FET sensor to generate a 16.6 ppm change in the input power with a measured V_{neural}. This results in $\sim$120 nW (-39 dBm) of backscattered power at the input given a 1 mm^2 transceiver aperture outputting 7.2 mW of power to satisfy safety regulations on output power density of 720 mW/cm^2. With such power levels, given a thermal noise spectral density of -174 dBm/Hz of input noise power, 10 kHz of BW, 10 dB of noise figure, and 10 dB of SNR, a traditional CMOS receiver should be sensitive enough to detect at minimum -114 dBm of input power. A number of highly-sensitivity receivers with $<$ mW of DC power consumption have been demonstrated (e.g., [76]).

For a 20 μm dust, however, Figure 3.8 shows that the upper limit on the FET size imposed by the power limit is lower than the lower limit set by the noise limit, indicating that the passive implementation of neural dust system scales roughly to 20 μm.

3.2.4 Re-design of neural dust mote

The scaling of neural dust mote is limited by the noise requirement of the front-end architectures, which is determined by the achievable differential signals between the electrodes. Decoupling the inherent tradeoff between the size of individual implants and the achievable SNR can improve the scaling of these implementations.

Since the trade-off derives directly not from the neural dust dimension, but from electrode separation, one approach may be to add very small footprint ($\sim$1 – 5 μm wide) "tails" which

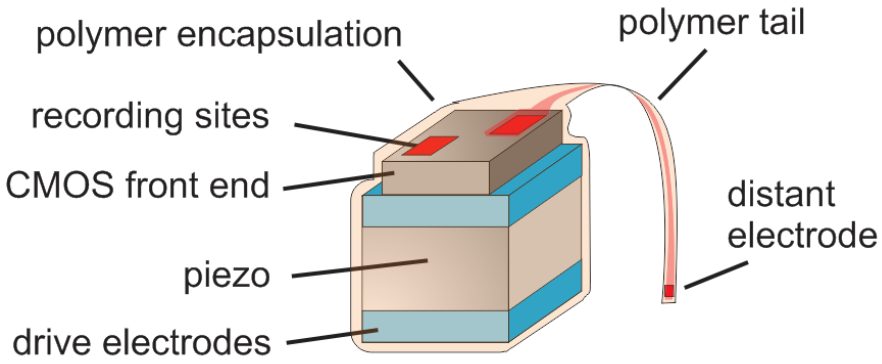

Figure 3.9: Neural dust with an ultra-compliant flexible polyimide "tail", populated with recording sites, can be envisioned to bypass the limits of the achievable differential signal between two electrodes placed on a neural dust footprint.

position a single (or multiple) electrode relatively far ($> 50 - 100$ μm) from the base of the neural dust implant. This would result in the design shown in Figure 3.9, where instead of placing a single differential surface electrode on neural dust, the neural dust can consist of a short strand of flexible and ultra-compliant substrate populated with recording sites. Assuming that the achievable electrode separation in the tail of a 20 μm mote is 100 μm, this implies that the noise limit, as shown in Figure 3.8, will set the lower bound to 0.4 μm of transistor width and allow the design of a FET sensor on the dust mote that achieves the optimal sensitivity, at 5.7e-2 ppm. This corresponds to 410 pW (-63.9 dBm) of backscattered power at the input, which is still in the realm of feasibility with a traditional CMOS receiver [76]. Therefore, this approach can address one of the major pitfalls with only a minor adjustment to the original idea as this neural dust still operates under the same principle as before, but has higher achievable SNR.

Note that the exact technology used for the previous analysis is not critical to the conclusion we drew. Although the absolute value of the impedance level is important since it determines the reflection coefficient, and therefore, the efficacy of the backscatter, as shown in Figure 3.8, the analysis above indicates that the optimal transistor width for the maximal sensitivity is small compared to the available neural dust footprint. Therefore, although the threshold voltage (hence the nominal impedance level per transistor width) may vary among different technology nodes, achieving the optimal impedance level within the footprint may not be an issue.

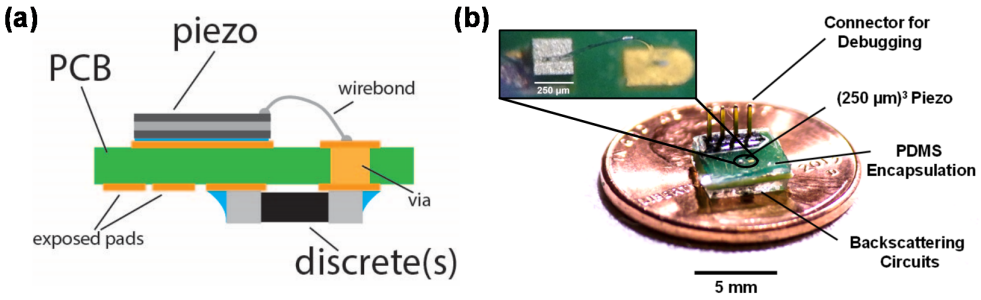

Figure 3.10: (a) Assembly prototype schematic (b) a picture of the complete prototype with a white light micrograph of PZT crystal mounted on board.

3.3 Experimental result

3.3.1 Sample preparation

The assembly prototype, shown in Figure 3.10, was realized on a 31 mil thick two-layer FR-4 board while metalized PZT coupons of various thicknesses (PSI-5A4E, Piezo Systems and PZT 841, APC International) were bonded to pre-soldered bumped electrodes on one side of the board using solder paste. The discrete FET (RV1C002UN, Rohm Semiconductor) and bias resistors for ultrasonic communication were assembled onto the side opposite to where the PZTs were mounted prior to bonding. The PZTs were then wafer saw diced, with non-bonded areas dropping off and leaving an array of small PZT crystals bonded to the PCB. Next, a single wirebond made the connection between the top plate of the PZT and an electrode on the PCB, completing the circuit. Finally, the entire assembly was coated in PDMS to protect the wirebond and provide insulation. The pitch between the unit cell is limited by the size of the discrete components and is roughly 2.3 mm$\times$ 2 mm.

3.3.2 Electrical characterization

Electrical properties of the PZT crystals on the assembled prototype were measured using a vector network analyzer (VNA). The device under test (DUT) was calibrated using open/short/load structures fabricated on the same board to de-embed the board and fixture parasitics. Figure 3.12(b) shows a representative impedance plot of a (250 μm)^3 PZT crystal compared to simulation. We note that the mechanical loading of the circuit board itself (FR-4), PDMS encapsulant, and water heavily dampened the electro-mechanical resonances as compared to the unloaded condition (air backing). The mechanical quality factor Q_m can be calculated from

$$Q_m = \frac{f_a^2}{2\pi f_r Z_r C_p (f_a^2 - f_r^2)} \tag{3.7}$$

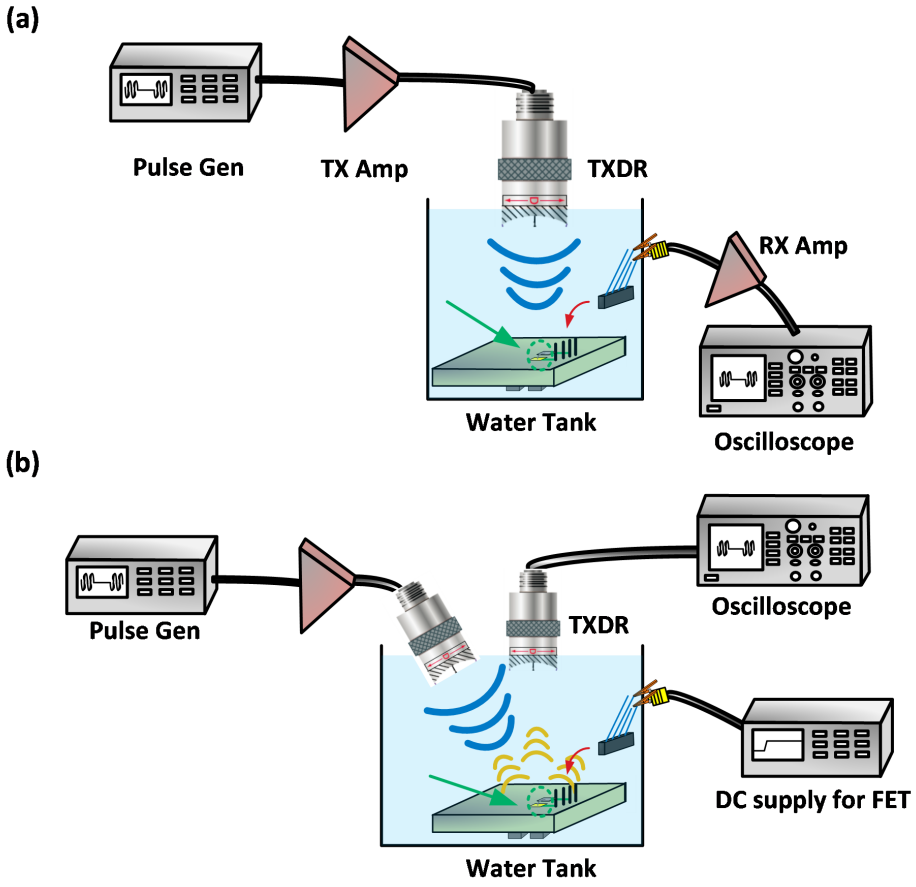

Figure 3.11: Acoustic characterization setup with a calibrated ultrasonic transducer for (a) power delivery and (b) backscatter communication verification.

where f_a and f_r represent anti-resonant (where impedance is maximized) and resonant frequency (where impedance is minimized), respectively, Z_r represents an impedance at resonance, and C_p is the low-frequency capacitance. The calculated quality factor from the measurement is roughly 4.2 compared to 5.1 in simulation. According to the datasheet, the unloaded Q_m of the PZT is ~500, indicating that FR-4 backing and wirebonds are causing significant degradation in Q_m. Despite this drastic reduction in Q_m of the PZT crystals, experiments showed that the backscattered signal level only decreased by roughly ~19% between the mechanically unloaded and loaded conditions.

3.3.3 Ultrasonic characterization

Ultrasonic power transfer and communication were performed using a home-built setup shown in Figure 3.11. A commercially available 5 MHz or 10 MHz single-element transducer with ~30 mm focal distance was mounted on a computer-controlled 2D translating

stage. The transducer's output was calibrated using a hydrophone. Assembly prototypes were placed in a water[8] container such that transducers could be immersed in the water at a distance of approximately 30 mm directly above the prototype. A programmable pulse generator and radio frequency amplifier were used to drive transducers at specified frequencies with sinusoidal pulse trains of 10-cycles and a pulse repetition frequency (PRF) of 1 kHz. The received signals were amplified with a preamplifier and a low-noise amplifier chain and displayed on the scope. For communication measurement, in order to eliminate feedthrough between transmit and receive stages and reflections from the board, separate transmit and receive transducers were used.

3.3.4 Measurement result

The total integrated acoustic output power of the transducer at various frequencies over the 6 dB bandwidth of the beam was measured using a calibrated hydrophone. Nominally, spatial-peak temporal-average (or I_{SPTA}) was kept at 29.2 μW/cm^2, resulting in a total output power of $\sim$1 μW at the focal spot, with a peak rarefaction pressure of 25 kPa and a mechanical index of 0.005. Both the de-rated I_{SPTA} and MI were far below the FDA regulation limit of 720 mW/cm^2 and 1.9, respectively [47].

Power link efficiency

Figure 3.12(a) shows the measured power delivery efficiency of the fully assembled prototype with cable loss calibrated out for various mote sizes as compared to analytical predictions made for this same setup. Measured results matched the simulated model behavior very closely across all mote sizes, with the exception of a few smaller mote dimensions, likely due to the sensitivity to transducer position and the ultrasound beamwidth. The measured efficiency of the link for the smallest PZT crystal (127 μm)^3 was 2.064×10^{-5}, which resulted in 20.64 pW received at the dust mote nominally. A maximum of 0.51 μW can be recovered at 720 mW/cm^2. Such low power level harvested by the PZT compared to what was predicted in the previous section is due to the extreme efficiency of broadband transducers and the beam-spreading at the interrogation distance of 30 mm for the transducer used for the experiment.

Backscatter sensitivity

The backscatter simulation framework was verified by measuring the difference in the backscattered voltage level and computing the ppm change, i.e., sensitivity, when the PZT crystal was electrically open versus shorted[9]. Backscatter measurement in Figure 3.13 matched the analytical model behavior very closely and the sensitivity of (127 μm)^3 dust mote was $\sim$5000

[8] Mineral oil can be used in place of water in order to eliminate conductance through the media.

[9] The maximal change in the backscatter should occur when the mote is conjugate matched ($Z_L = Z^*_{PZT}$) to either open or short.

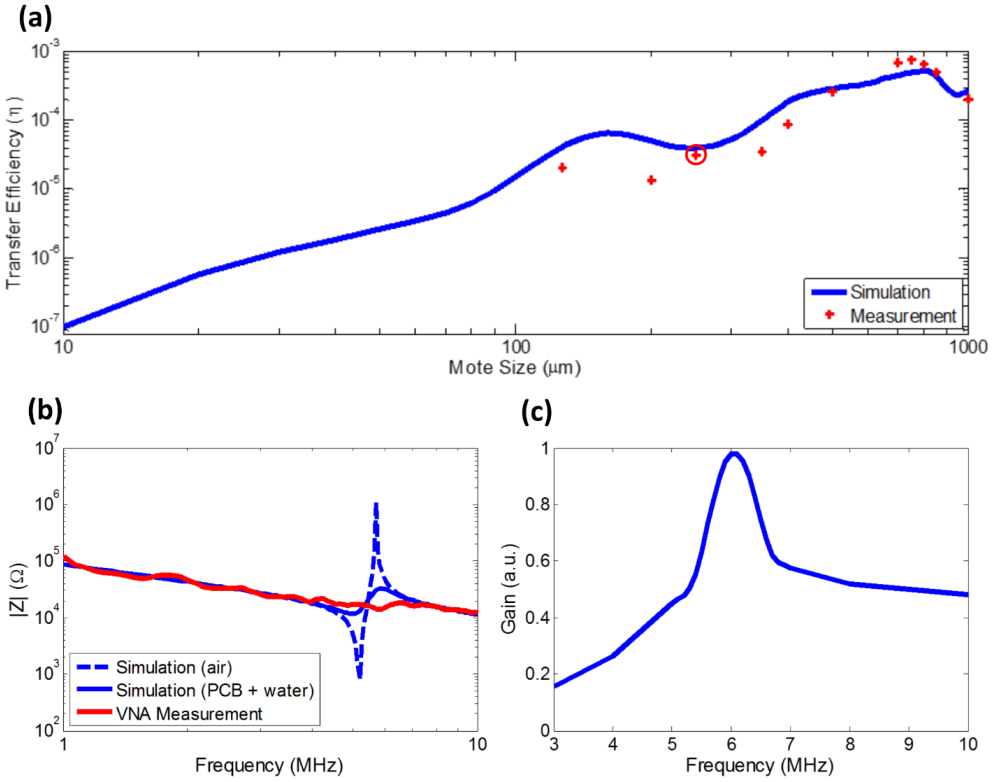

Figure 3.12: (a) Measured power transfer efficiency at various mote sizes matches simulated behavior. For each mote dimension, both (b) the impedance spectroscopy and (c) frequency response of harvested power on the PZT reinforce the reliability of the simulation framework.

ppm. The measurement of backscatter sensitivity was limited by heat-induced drift noise of the instruments and the inaccurate model of the broadband transducer. Therefore, properly tuned measurement system is required to measure much lower backscatter signals generated when a more realistic action potential voltage appears at the V_{GS} of the FET to modulate the impedance by less than 0.1%. Figure 3.13 also shows that the achievable simulated backscatter sensitivity substantially increase under a low-drift setup with a dedicated custom-made transducer that achieves optimal focal distance and electrical input impedance at each mote dimension[10].

3.4 Conclusion

In this chapter, we propose neural dust, which uses ultrasound to power and communicate with miniature sensors implanted inside the body. We analyzed fundamental system design trade-offs and ultimate size, power, and bandwidth scaling limits of such system from first

[10]Input of the two-port network is conjugate matched to extract $G_p \geq G_t$.

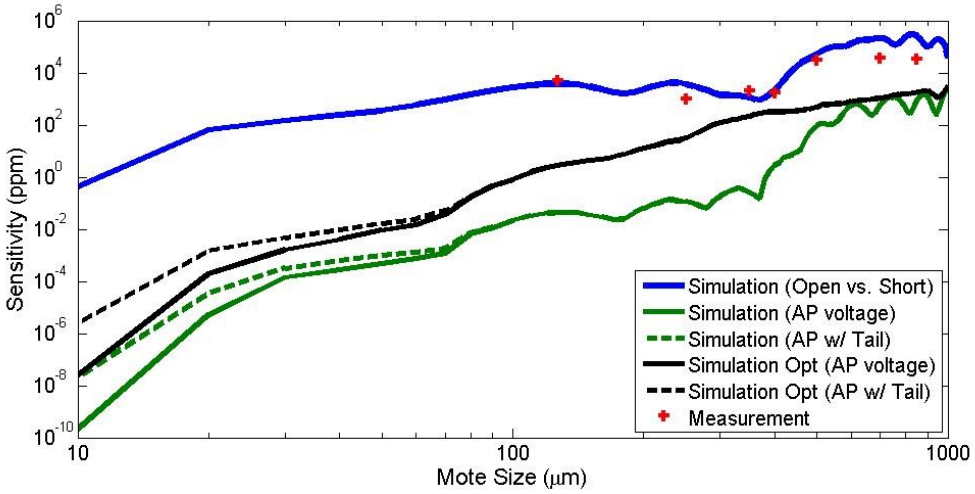

Figure 3.13: Simulated and measured backscatter sensitivity scaling plot for various impedance levels match for open vs. short modulation. Simulations indicate that for realistic neural spiking voltage, highly sensitive receiver (detecting 1e-8 ppm or less) would be needed.

principles and experimentally verified the model down to, at least, $\sim$100 μm scales (and likely lower). We also verified that our model can correctly capture the effects of changing the load impedance of a piezoelectric transducer on the backscatter signals at such scales.

While the analysis shown in this chapter pre-supposes a system for recording from the central nervous system (more specifically the neocortex), neural dust may also find utility in the peripheral nervous system, as discussed in the next chapter (Chapter 4).

Chapter 4

In-vivo Recordings with Neural Dust

The emerging field of bioelectronic medicine seeks methods for deciphering and modulating electrophysiological activity in the body to attain therapeutic effects at target site. As a result, there has been growing interest in the use of neural recording technologies to improve neurostimulation-based treatments as well as to develop new closed-loop neuromodulation therapies for disorders in both the central [55] and peripheral [29] nervous systems.

In particular, recent technological advances and fundamental discoveries have renewed interest in implantable system for interfacing with the peripheral nervous system. Early clinical successes with the peripheral neurostimulation devices, such as those used to treat sleep apnea [101] or control bladder function in paraplegics [22] have led clinicians and researchers to propose new disease targets ranging from diabetes to rheumatoid arthritis [29]. Because nerves carry both afferent and efferent signals to a variety of target organs, effective recording technologies will need high spatiotemporal resolution to record from multiple discrete sites within a single nerve. Current approaches to interfacing with peripheral nerves and muscles, however, rely heavily on wires, creating problems for chronic use, while emerging wireless approaches lack the size scalability necessary to interrogate small-diameter nerves.

In this chapter, we demonstrate wireless recordings from nerve (electroneurogram or ENG) and muscle (electromyogram or EMG) in a rodent model using neural dust.

4.1 Neural dust system

4.1.1 Assembly of neural dust implant

Figure 4.1 shows the assembly process for a neural dust implant mote integrated on a 50 μm thick polyimide flexible printed circuit board (PCB) where both the piezocrystal (0.75 mm $\times$ 0.75 mm $\times$ 0.75 mm) and the custom transistor (0.5 mm $\times$ 0.45 mm) are attached to the topside of the board with a conductive silver paste.

Electrical connections between the components are made using aluminum wirebonds and conductive gold traces. Exposed gold recording pads on the bottom of the board (0.2 mm $\times$

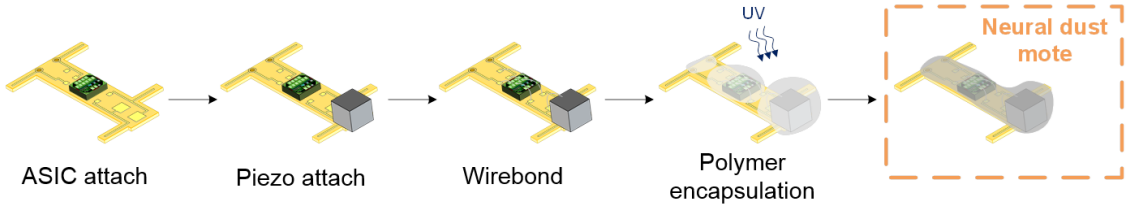

Figure 4.1: Robust, high-yield fabrication steps for the mote, which is encapsulated with medical grade, UV-curable epoxy.

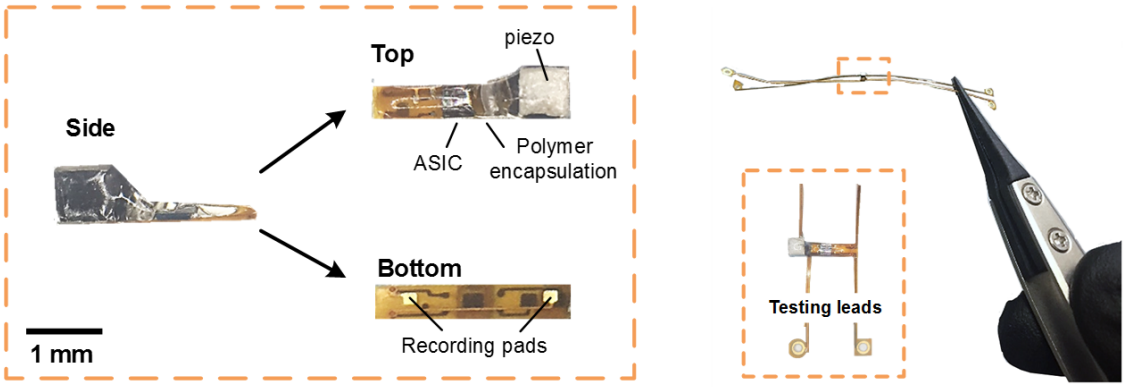

Figure 4.2: Close-up of neural dust mote on flexible PCB with testing leads to measure electrophysiological signals (ground truth) and voltages harvested on the piezoelectric transducer. During the in-vivo experiments, testing leads are removed.

0.2 mm) are separated by 1.8 mm and make contact on the nerve or muscle to record electrophysiological signals as shown in Figure 4.2. Recorded signals are sent to the transistor's input through micro-vias. Additionally, some implants were equipped with 0.35 mm wide, 25 mm long, flexible, compliant leads shown in Figure 4.2 with test points for simultaneous measurement of both the voltage across the piezocrystal and direct wired measurement of the extracellular potential across the electrode pair used by the mote (we refer to this direct, wired recording of extracellular potential as the ground truth measurement, which is used as a control for the ultrasonically reconstructed data). The entire implant is encapsulated in a medical grade UV-curable epoxy to protect wirebonds and provide insulation. A single neural dust mote implant measures roughly 0.8 mm $\times$ 3 mm $\times$ 1 mm. The size of the implants presented here is limited only by our use of commercial polyimide backplane technology, which is commercially accessible to anyone; relying on more aggressive assembly techniques with in-house polymer patterning would produce implants not much larger than the piezocrystal dimensions (yielding a < 1 mm^3 implant).

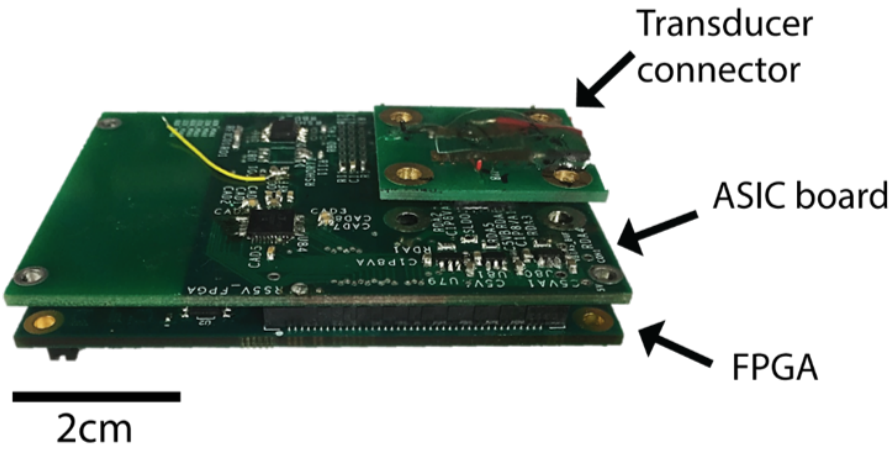

Figure 4.3: The transceiver board consists of Opal Kelly FPGA board, ASIC (see [105]), and the transducer connector board.

4.1.2 Ultrasonic transceiver module

An external, ultrasonic transceiver board shown in Figure 4.3 interfaces with neural dust motes by both supplying power (transmit (TX) mode) and receiving reflected signals (receive (RX) mode). This system is a low-power, programmable, and portable transceiver board that drives a commercially available external ultrasonic transducer (V323-SU, Olympus, Waltham, MA).

The transceiver board consisted of a custom ASIC in a QFN-64 package that achieved an on-chip 1.8 to 32 V charge pump efficiency of 33% and system latency of 20 ns, while consuming 16.5 μJ per each transmit cycle [104, 105]. In addition, the ASIC has 7 identical channels, each with 6 bits of delay control with 5 ns resolution for transmit beamforming. During the receive mode, the high voltage switch was closed, and the signal was amplified by 28 dB; both operations were performed on chip. The output signal from the chip was digitized by an off-chip 10-bit, 100 MHz analog-to-digital converter (ADC). The outputs of the ADC were fed back into the field-programmable gate array (FPGA) and USB 3.0 integration module (XEM6310-LX45, Opal Kelly) and transferred to the laptop. The FPGA-USB module was also used to serially program the ASIC.

4.1.3 Sequence of signal flow

The neural dust mote was placed one Rayleigh distance ($t_{Rayleigh}$) from the transducer (at ~8.9 mm), which corresponded to 5.9 μs of transit time, assuming an acoustic velocity of ~1500 m/s in water.

During operation, the external transducer alternates between (1) emitting a series of six 540 ns pulses with peak voltage of 5 V every 100 μs (or pulse repetition frequency (PRF) of

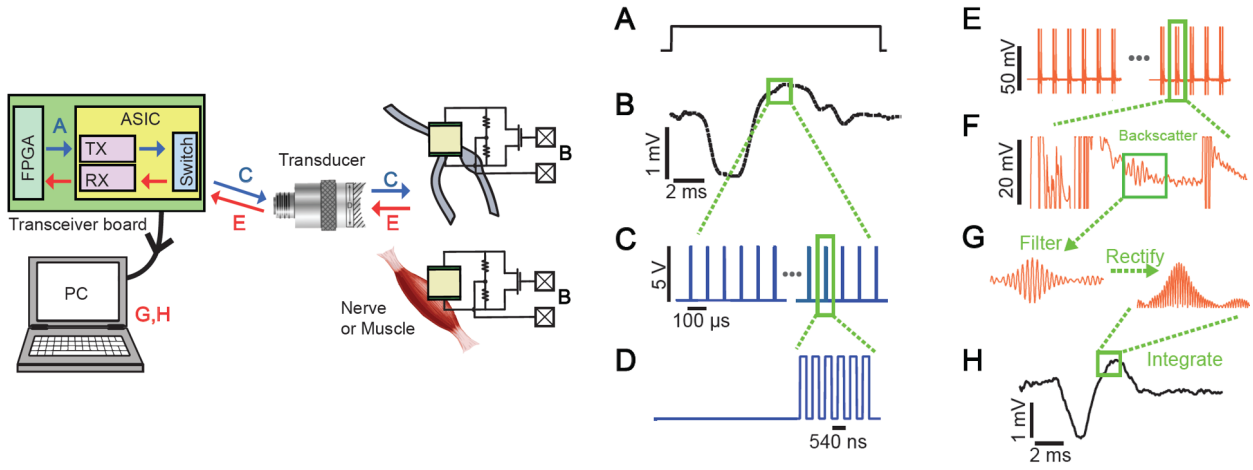

Figure 4.4: (Left) Schematic flow of information; (Right) representative time traces of signals at each step. The sequence is for reconstruction at one time point. (a) The FPGA generates a trigger signal to initiate recording. (b) An extracellular, electrophysiological potential is presented to the recording electrodes on a neural dust mote. (c) Upon receiving the trigger from the FPGA, the transceiver board generates a series of transmit pulses. At the end of the transmit cycle, the switch on the ASIC disconnects the transmit module and connects the receive module. (d) Zoomed-in transmit pulse sequence, showing 6 pulses at 1.85 MHz. (e) Backscatter from the neural dust mote reaches the transducer approximately $2t_{Rayleigh}$. (f) Zoomed-in backscatter waveforms, aligned in time with (e). Note the large, saturating signal which overlaps with the transmit pulses is electrical feedthrough and is ignored. The returning, backscattered pulses can be seen subsequent to the transmission window (green box). A close up of the backscatter pulses is shown in Figure 4.10 and discussed in the text. (g) These backscattered pulses are filtered and rectified, and the area under the curve is computed in order to produce reconstructed waveforms. (h) Reconstructed waveform is sampled at 10 kHz. Each point of the reconstructed waveform is computed by calculating the area under the curve of the appropriate reflected pulses, received every 100 μs.

10 kHz)[1] and (2) listening for any reflected pulses. The entire sequence of transmit, receive, and reconstruction events are detailed in Figure 4.4; this sequence (steps A - H) is repeated every 100 μs during operation. Briefly, pulses of ultrasonic energy emitted by the external transducer impinge on the piezocrystal and are, in part, reflected back toward the external transducer. In addition, some of the ultrasonic energy causes the piezocrystal to vibrate; as this occurs, the piezocrystal converts the mechanical power of the ultrasound wave into electrical power, which is supplied to the transistor. Any extracellular voltage change across

[1]Given that the first reflection back to the transducer (e.g., backscatter) occurred at approximately 11.8 μs (twice the transit time) and persisted until for 3.3 μs, the maximum PRF (e.g., in this context, the sampling rate) was ~66 kHz. Given that a typical bulk peripheral nerve responses occur below 1 kHz [66], a PRF of 10 kHz was chosen to sufficiently capture the dynamics.

the two recording electrodes modulates the transistor's gate, changing the amount of current flowing between the terminals of the crystal. These changes in current, in turn, alter the vibration of the crystal and the intensity of the reflected ultrasonic energy. Thus, the shape of the reflected ultrasonic pulses encodes the electrophysiological voltage signal seen by the implanted electrodes and this electrophysiological signal can be reconstructed externally.

4.1.4 Received data processing

In order to sample the backscatter waveform at 1.85 MHz without losing signal fidelity, the off-chip ADC on the transceiver board was heavily oversampled at 50 MHz. This resulted in ∼8 Mbits of data in a 20 ms neural recording, which was stored in a 128 MByte, 16-bit wide, synchronous DDR2 DRAM (MT47H64M16HR-3, Micron Technology). The raw waveforms were transferred to the laptop via the USB interface post-recording. The raw waveforms were simultaneously recorded using an 8-bit digitizer (USB-5133, National Instruments) for comparison.

Raw backscatter waveforms from each experiment were sliced and time aligned to be averaged over eight samples. The averaged signals were band-pass filtered with a symmetric fourth order Butterworth filter from 10 Hz to 1 kHz. The distinct characteristics of the backscatter waveform, as shown in Figure 4.10, were used as a template to locate the region of interest. The signals were then rectified, and the integral of the region was computed to estimate the input voltage signal, which exhibited a linear response as shown in Figure 4.12(a). Multiplication factor for the signal was extracted from the ground truth measurement.

4.2 Neural dust characterization

4.2.1 Piezoelectric impedance measurement

To characterize the piezocrystal prior to assembly, an impedance plot was obtained with an impedance analyzer (4285A, Agilent) using two-terminal measurements with open/short/load calibration scheme.

Simulated impedance spectrums using various models of the piezocrystal, such as the KLM, resonance, and COMSOL models described in Chapter 3, matched the measured resonant frequency at 1.85 MHz with the impedance magnitude of ∼100 Ω as shown in Figure 4.5. Given the aspect ratio of 1, the measurement of 0.75 mm × 0.75 mm × 0.75 mm piezocrystal used in the prototype showed a splitting of the anti-resonant peak due to mode coupling, at 2.25 MHz and 2.6 MHz, which was captured by the COMSOL model. Both KLM and the resonance model, however, did not capture this effect. Although the COMSOL model of the piezocrystal was more accurate, in order to reduce the computational complexity, KLM model was used to simulate the link behavior near the operation frequency of 1.85 MHz.

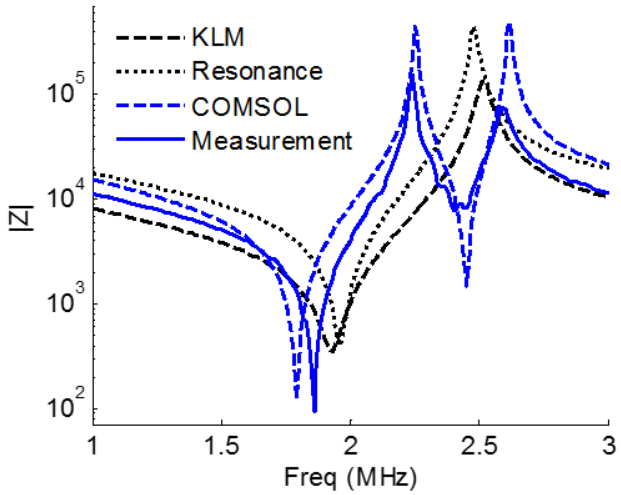

Figure 4.5: Measured impedance spectrum of a 0.75 mm × 0.75 mm × 0.75 mm PZT crystal matched impedance estimated by the resonance, KLM, and COMSOL models.

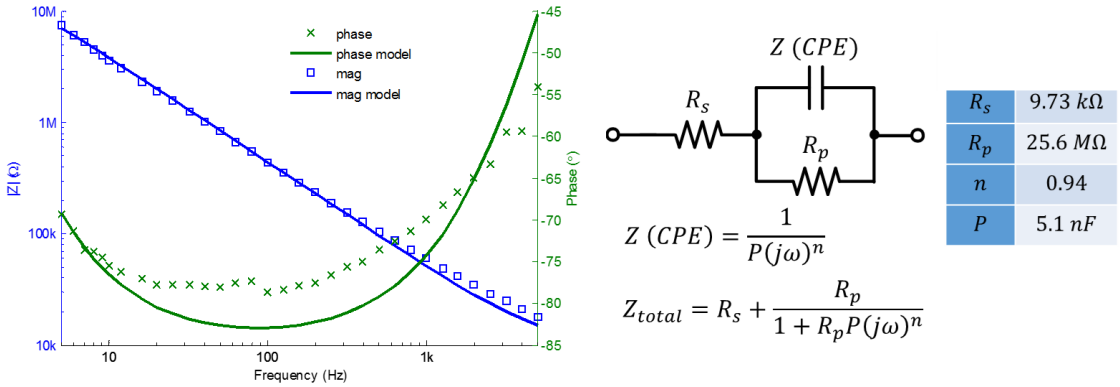

Figure 4.6: Impedance spectroscopy of the gold electrodes on a flexible PCB and the fit using Randles Cell model.

4.2.2 Recording electrode modeling

A recording electrode pair was made of immersion gold by a flexible PCB vendor (Altaflex, Santa Clara, CA) and measured 0.2 mm × 0.2 mm. We characterized the electrical properties of the surface electrode by measuring the recording site impedances in Phosphate Buffered Solution (PBS 1×) with an electrochemical impedance spectroscope (nanoZ, White-Matter LLC, Mercer Island, WA). The device formed the active electrode and a silver wire formed the reference electrode. The electrode/electrolyte interface can be fitted to a Randles Cell model [87] to extract the line resistance (R_s = 9.73 kΩ), charge transfer resistance (R_p = 25.6 MΩ), and the parameters of the constant phase element (CPE: n = 0.94, P = 5.1 nF·s^n); the MATLAB package Zfit was used to fit these parameters as shown in Figure 4.6.

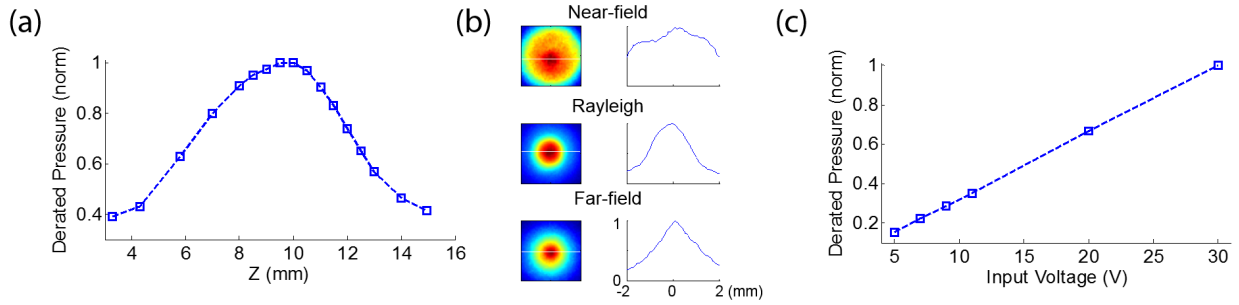

Figure 4.7: (a) A de-rated, normalized peak pressure as a function of distance from the surface of the transducer showed a de-rated focus at ∼8.9 mm at 1.85 MHz. (b) The XY cross-sectional beampatterns and the corresponding 1D voltage plot at y = 0 at near-field, Rayleigh distance, and far-field showed beam focusing at the Rayleigh distance. (c) The transducer's output pressure was a linear function of input voltage (up to 32 V peak-to-peak).

4.2.3 Ultrasonic measurement setup

Ultrasonic characterization of the transducer was performed in a custom-built water tank, similar to the one described in Chapter 3. A capsule hydrophone (HGL-0400, Onda) with 20 dB preamplification (AH-2020, Onda) was mounted on a computer-controlled 2D translating stage (XSlide, VelMex) and was used to calibrate the output pressure and characterize beam patterns of a 2.25 MHz single-element transducer (V323-SU, Olympus). Verification of ultrasonic power transfer and communication sensitivity was performed in a smaller water tank with the transducer mounted on manual translational and rotational stages (Thorlabs). The outline of the neural dust mote was patterned on an extruded acrylic piece with UV laser, and the mote was clamped to the acrylic stage with nylon screws. The position and angle of the transducer with relative to the mote were manually adjusted until the maximum voltage was measured across the piezocrystal. Cable capacitances and parasitics were carefully calibrated by adjusting the series capacitance in the high-impedance probes (N2863B, Agilent).

For initial calibration of the system, a current source (2400-LV, Keithley, Cleveland, OH) was used to mimic extracellular signals by forcing electrical current at varying current densities through 0.127 mm thick platinum wires (773000, A-M Systems, Sequim, WA) immersed in the tank. The neural dust mote was submerged in the current path between the electrodes. As current was applied between the wires, a potential difference arose across the implant electrodes. This potential difference was used to mimic extracellular electrophysiological signals during tank testing.

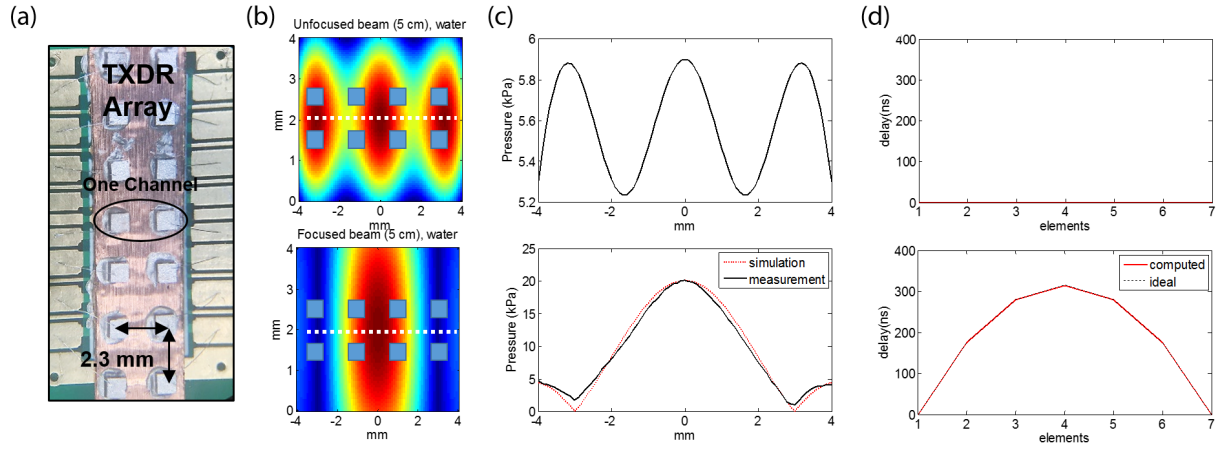

Figure 4.8: (a) 7 groups of 2 × 1 elements formed an array. (b) 2D and (c) 1D beam patterns of unfocused and focused beam at the Rayleigh distance. (d) Applied time delay to each element.

4.2.4 Transceiver characterization

The transceiver board exhibited a de-rated focus at ∼8.9 mm as shown in Figure 4.7(a). The XY cross-sectional beam-pattern clearly demonstrated the transition from the near-field to far-field propagation of the beam, with the narrowest beam at the Rayleigh distance as shown in Figure 4.7(b). The transducer was driven with a 5 V peak-to-peak voltage signal at 1.85 MHz. The measured de-rated peak rarefaction pressure was 14 kPa, resulting in a mechanical index (MI) of 0.01. De-rated spatial pulse peak average (I_{SPPA}) and spatial peak time average (I_{SPTA}) of 6.37 mW/cm^2 and 0.21 mW/cm^2 at 10 kHz pulse repetition were 0.0034% and 0.03% of the FDA regulatory limit, respectively [47]. The transceiver board was capable of outputting up to 32 V peak-to-peak and the output pressure increased linearly with the input voltage as shown in Figure 4.7(c).

Beamforming measurement

In order to verify the beamforming capabilities of the transceiver module, 7 groups of 2 × 1 PZT elements, with the pitch of $\sim 5/2\lambda = 2.3$ mm were formed as an array as shown in Figure 4.8(a). The array measured approximately 14 mm × 3 mm and the resulting focal depth of the array was 50 mm.

The transducer array's 2D beam pattern and output were calibrated using a capsule hydrophone (HGL-0400, Onda, Sunnyvale, CA). The measured XY cross-sectional beam pattern with the overlay of the array and the applied delay are shown in Figure 4.8. The -6 dB beamwidth at the focal point is 3.2 mm $\sim 3\lambda$. The flexibility of the ASIC allowed for both wide and granular programming of the delays. The peak pressure level of the array at 50 mm before and after beamforming was ∼6 kPa and ∼20 kPa, respectively. The 3× in the

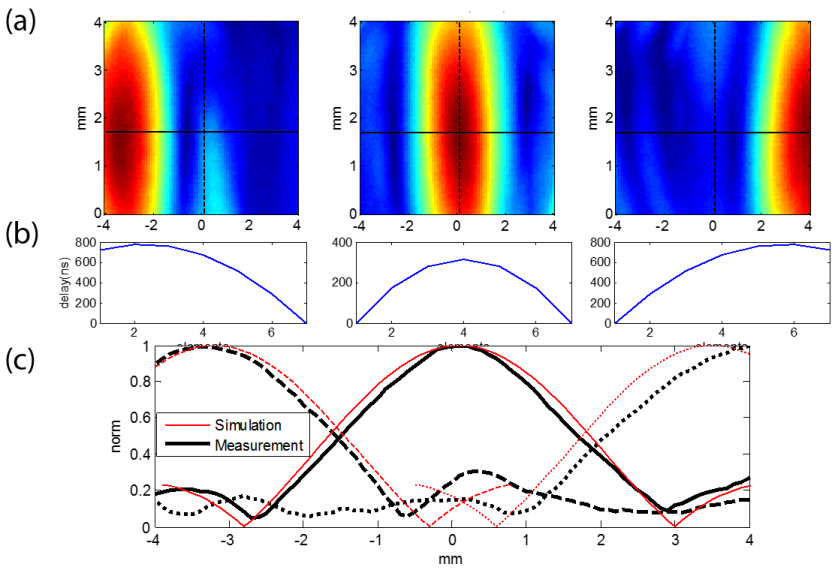

Figure 4.9: (a) Demonstration of beam steering. (b) Applied time delay for each direction. (c) 1D beam pattern in X-axis.

transmitted output pressure wave after beamforming matched the simulation.

Additionally, in order to verify the capability to interrogate multiple neural dust motes, we verified the beam steering capability of the array as shown in Figure 4.9. The 1D beam steering matched very closely with the simulation[2].

4.2.5 Backscatter signal property

The emitted pulses from the transceiver reflect off the neural dust mote and produce backscatter pulses. Reflected backscatter pulses are recorded by the same transceiver board. The signal flow is detailed in Figure 4.4.

The received backscatter waveform exhibits four regions of interest; these are pulses reflecting from four distinct interfaces as shown in Figure 4.10: (1) the water-polymer encapsulation boundary, (2) the top surface of the piezoelectric crystal, (3) the piezo-PCB boundary, and (4) the back of the PCB. As expected, the backscatter amplitude of the signals reflected from the piezoelectric crystal (second region) changed as a function of changes in potential at the recording electrodes. Reflected pulses from other interfaces did not respond to changes in potential at the recording electrodes. Importantly, pulses from the other non-responsive regions were used as a signal level reference, making the system robust to motion or heat-induced artifacts (since pulses reflected from all interfaces change with phys-

[2]The beam steering range was limited to ±4 mm due to the mechanical construct of the array, rather than the electronic capability.

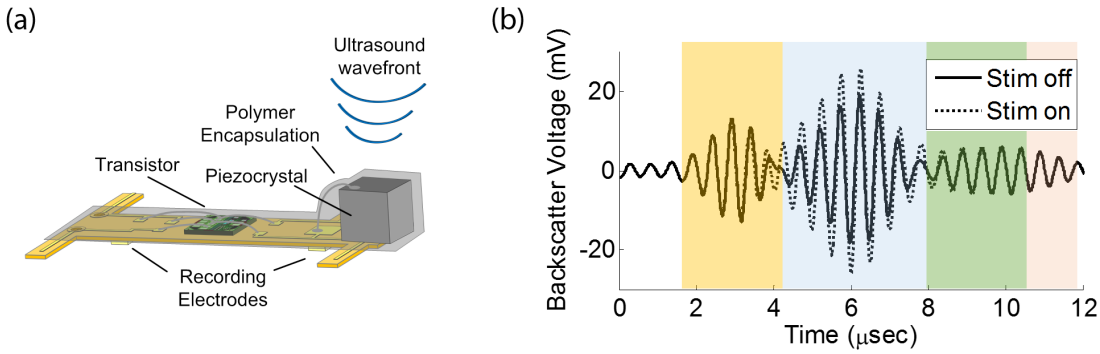

Figure 4.10: (a) Cross-section of the neural dust mote. (b) Example backscatter waveform showing different regions of backscatter. The backscatter waveform is found flanked (in time) by regions which correspond to reflections arising from non-responsive regions; these correspond to reflected pulses from other device components shown in (a). The measurement from the non-responsive regions, which do not encode biological data, can be used as a reference. As a result of taking this differential measurement, any movements of the entire structure relative to the external transducer during the experiment can be subtracted out.

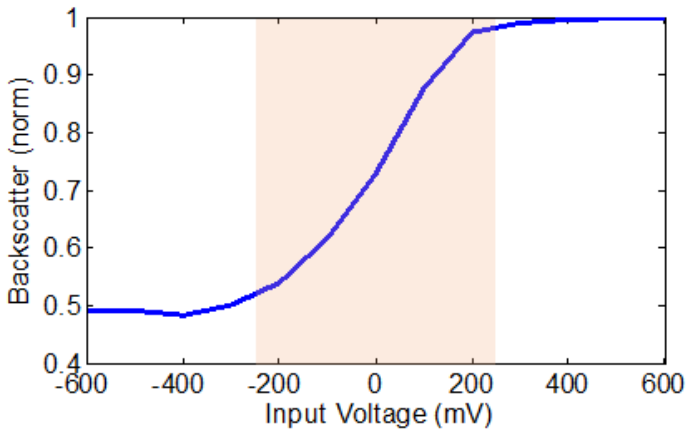

Figure 4.11: Calibration curve of neural dust showed that the overall dynamic range of the system was greater than >500 mV, which was substantially larger than the input range of neural signature.

ical or thermal disturbances of the neural dust mote but only pulses from the second region change as a function of electrophysiological signals).

4.2.6 Noise floor and effects of misalignment

In a water tank, the system showed a linear response to changes in recording electrode potential and a noise floor of ∼0.18 mV_{rms} as shown in Figure 4.12(a). The overall dynamic

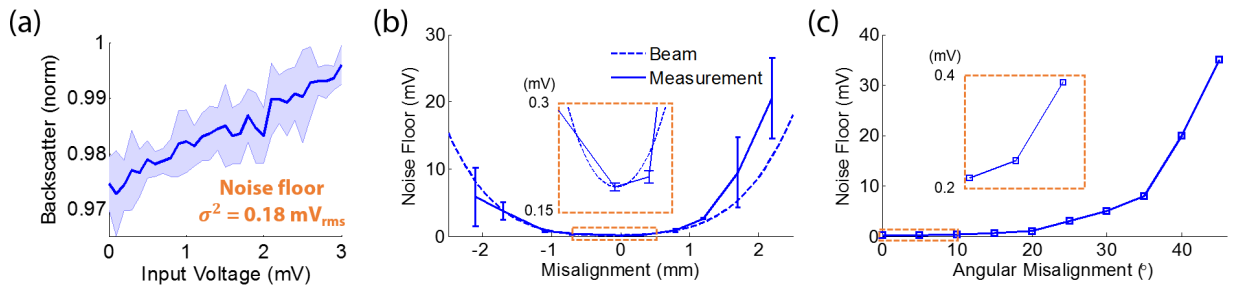

Figure 4.12: (a) Calibration curve obtained in the custom water tank setup showed the noise floor of 0.18 mV_{rms}. (b) The effect of noise floor as a function of lateral misalignment followed the beampattern power fall-off. (c) Plot of drop in the effective noise floor as a function of angular misalignment. Angular misalignment resulted in a skewed beam pattern: ellipsoidal as opposed to circular. This increased the radius of focal spot (spreading energy out over a larger area); the distortion of the focal spot relaxed the constraint on misalignment.

range of the system was limited by the input range of the transistor and was greater than > 500 mV as shown in Figure 4.11(i.e., there was only an incremental change in the current once the transistor was fully on (input exceeded its threshold voltage) or fully off). The noise floor increased with the measured power drop-off of the beam; 0.7 mm of misalignment degraded it by a factor of two (N = 5 devices) as shown in Figure 4.12(b). This lateral misalignment-induced increase in the noise floor constituted the most significant challenge to neural recordings without a beam-steering system (that is, without the use of an external transducer array that can keep the ultrasonic beam focused on the implanted dust mote and, thus, on-axis). On axis, the neural dust mote converted incident acoustic power to electrical power across the load resistance of the piezo with $\sim$25% efficiency. Figure 4.12(c) plots the change in effective noise floor as a function of angular misalignment.

4.3 In-vivo measurement

4.3.1 Surgical procedures

All animal procedures were performed in accordance with University of California Berkeley Animal Care and Use Committee regulations. Adult male Long-Evans rats were used for all experiments. Prior to the start of surgery, animals were anesthetized with a mixture of ketamine (50 mg/kg) and xylazine (5 mg/kg) intraperitoneally (i.p.). The fur surrounding the surgical site was shaved and cleaned. For EMG recordings, a patch of gastrocnemius muscle roughly 10×5 mm in size was exposed by removing the overlying skin and fascia. The neural dust mote was then placed on the exposed muscle, the skin and fascia were replaced, and the wound was closed with 5/0 surgical suture. For ENG recordings, the sciatic nerve was exposed by making an incision from the sciatic notch to the knee, and separating the

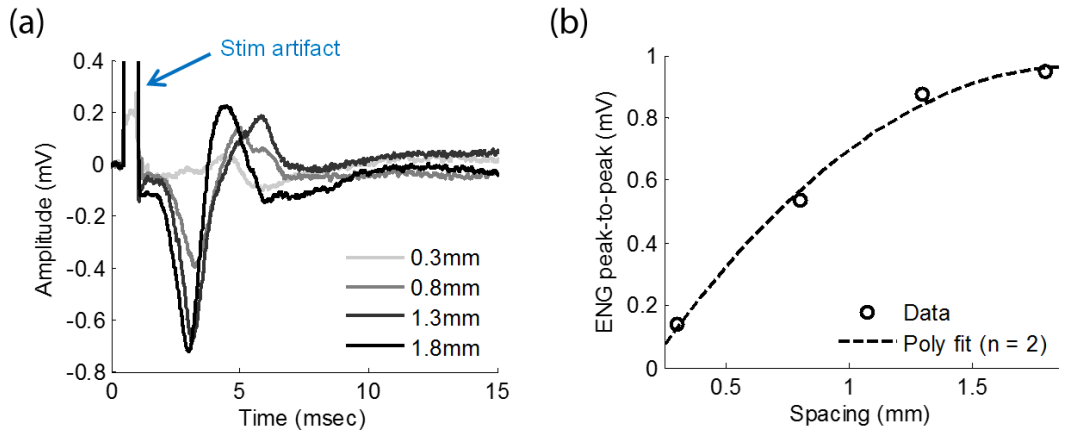

Figure 4.13: (a) Recorded time-domain ENG responses. (b) Peak-to-peak ENG with varying electrode spacing.

hamstring muscles. The mote was then placed in contact with the epineurium of the main branch of the sciatic nerve bundle and sutured to the nerve using 10/0 microsurgical suture. Animals were euthanized at the conclusion of the experiments.

4.3.2 Wired measurement

Constant-current stimulation was delivered using an isolated pulse stimulator (2100, A-M Systems). Single biphasic pulses with a 2 ms pulse width were used to deliver stimulation at various current amplitudes. For each experiment, electrophysiological responses from ten stimulations (i.e., samples) were recorded. The FPGA-USB module generated a trigger for the stimulator every 6 s. For EMG experiments, bipolar Ag-AgCl hook electrodes placed around the trunk of the sciatic nerve were used for stimulation. To evoke ENG activity, 28G stainless steel needle electrodes were placed in the foot with an inter-electrode distance of approximately 5 mm.

The wired signals were amplified (100×) by a battery-powered differential amplifier with a built-in band-pass filter (DAM50, WPI) set at 10 Hz to 1 kHz. The ground reference for the amplifier was a 28G stainless steel needle electrode placed in the contralateral foot relative to the recording setup. The output of the amplifier was connected to a multi-channel digitizer, sampled at 100 kHz, and recorded on computer.

In order to verify the recording setup, recording electrodes with various spacing were fabricated on a 50 μm thick polyimide flexible printed circuit board (PCB) and used for ENG recordings. There were a total of 5 electrodes, each measuring 0.2 mm × 0.2 mm, and one of them was used as the reference electrode. Other electrodes were spaced 0.3 mm, 0.8 mm, 1.3 mm, and 1.8 mm, respectively, apart from the reference electrode.

The spacing board was placed in contact with the epineurium of the main branch of the sciatic nerve bundle (distal) and sutured to the nerve. Bipolar Ag-AgCl hook electrodes

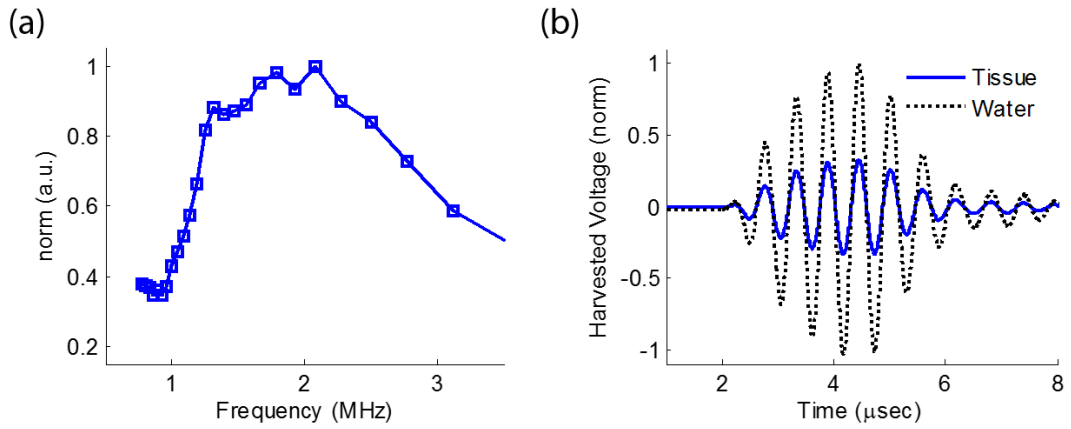

Figure 4.14: (a) Frequency response of the transducer. (b) Ultrasonic attenuation in 8.9 mm of tissue.

placed around the trunk of the sciatic nerve (proximal) were used for stimulation. Constant-current simulation of a single biphasic pulse with a duration of 0.5 ms every 1 second was delivered using an isolated pulse stimulator.

As expected, the peak-to-peak voltage recorded on the electrode increased with the spacing at least quadratically as shown in Figure 4.13. The amplitude saturated after the spacing of 1.3 mm, confirming that the electrode spacing of 1.8 mm on the recording sensor was sufficient to capture the maximum, saturated ENG response.

4.3.3 Wireless measurement

In-vivo ultrasonic transmission

A 2.25 MHz single element transducer (V323-SU, Olympus NDT, Waltham, MA) was used to generate 6 pulses at 1.85 MHz. The transducer had a measured half-power bandwidth (HPBW) of more than 2.5 MHz as shown in Figure 4.14(a). In order to measure the transmission loss through the tissue, various thicknesses of skin found near the gastrocnemius muscle of a male Long-Evans rat was placed in between the transducer and the neural dust prototype. The harvested voltage on the piezocrystal with and without tissue was obtained and the 8.9 mm of tissue resulted in 10 dB of tissue attenuation as shown in Figure 4.14(b).

EMG recordings

We recorded evoked EMG responses from the gastrocnemius muscle of adult Long-Evans rats under anesthesia using the neural dust system. The mote was placed on the exposed muscle surface, the skin and surrounding connective tissue were then replaced, and the wound was closed with surgical suture as shown in Figure 4.15(a). The ultrasonic transducer was positioned 8.9 mm away from the implant (one Rayleigh distance of the external transducer)

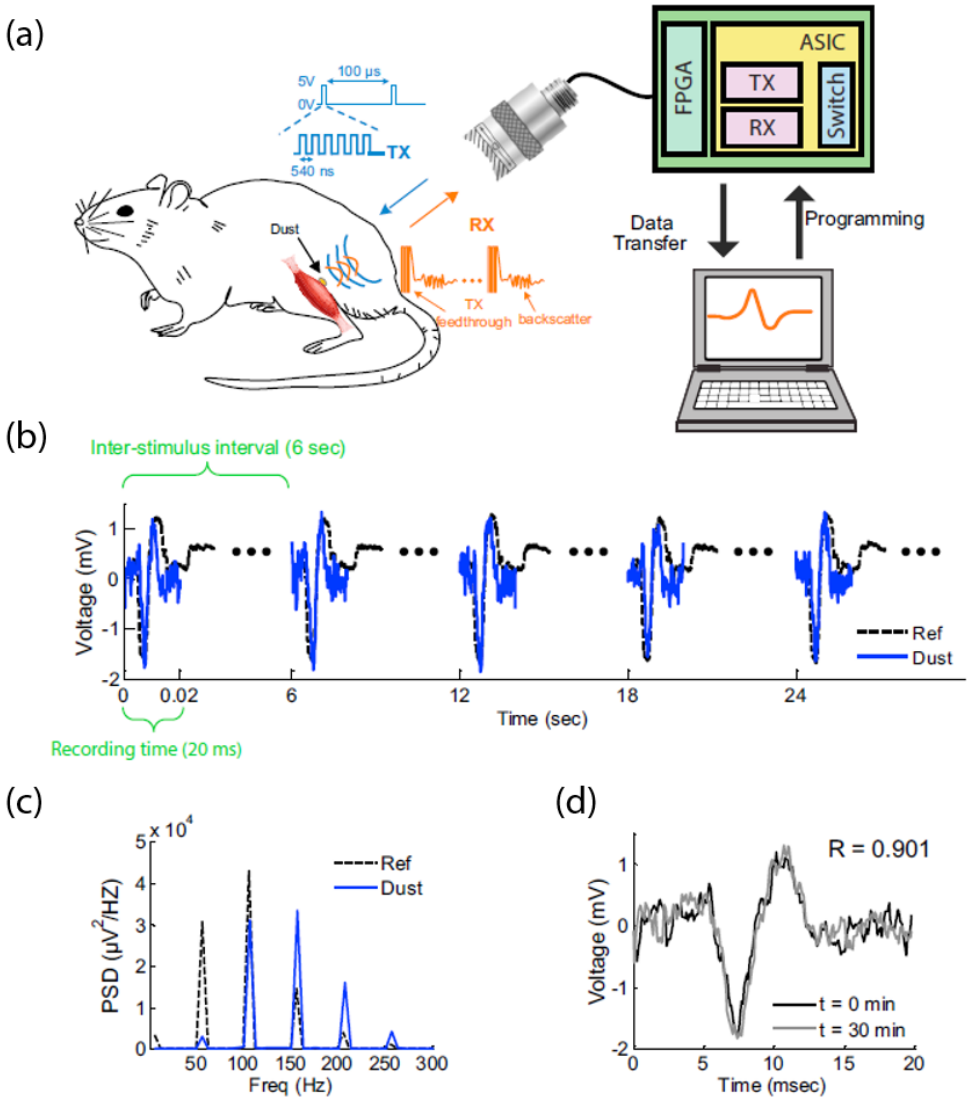

Figure 4.15: Tether-less neural dust rodent EMG. (a) In-vivo experimental setup for EMG recording from gastrocnemius muscle in rats; the neural dust mote was placed on the exposed muscle surface and the wound was closed with surgical suture. The external transducer couples ultrasound to the mote and the wireless data is recorded and displayed on the laptop. (b) Comparison between ground truth measurement and the reconstructed EMG signals over a number of trials. 20 ms samples were recorded and the inter-stimulus interval was 6 sec. (c) Power spectral density (PSD) of the recorded EMG signal showed 4.29e4 μV^2/Hz and 3.11e4 μV^2/Hz at 107 Hz for ground truth and the reconstructed dust data, respectively, and several harmonics due to edges in the waveform. (d) The wireless backscatter data recorded at t = 0 min and t = 30 min matched with R = 0.901.

and commercial ultrasound gel (Aquasonic 100, Parker Labs, Fairfield, NJ) was used to enhance coupling. The system was aligned using a manual manipulator by maximizing the harvested voltage on the piezocrystal measured from the flexible leads. Ag/AgCl wire hook electrodes were placed approximately 2 cm distally on the trunk of the sciatic nerve for the bulk stimulation of muscle fiber responses. Stimulation pulses of 200 μs duration were applied every 6 seconds and data was recorded for 20 ms around the stimulation window as shown in Figure 4.15(b). The power spectral density (PSD) of the reconstructed data with several harmonics due to edges in the waveform is shown in Figure 4.15(c). This process could be continued indefinitely, within the limit of the anesthesia protocol. Figure 4.15(d) shows a comparison of data taken after 30 minutes of continuous recording showed no appreciable degradation in recording quality.

We obtained EMG recruitment curves with both ground truth and wireless dust backscatter by varying stimulation amplitude as shown in Figure 4.16(a) and (b). Reconstruction of the EMG signal from the wireless backscatter data was sampled at 10 kHz, while the wired, ground truth measurement was sampled at 100 kHz with a noise floor of 0.02 mV. The two signals at response-saturating stimulation amplitude (100%) matched with R = 0.795 as shown in Figure 4.16(c). Figure 4.16(d) shows that the difference between the wireless and wired data was within 0.4 mV. The salient feature of the neural dust mote EMG response was approximately 1 ms narrower than the ground truth, which caused the largest error in the difference plot, shown in Figure 4.16(c) and (d). The responses from skeletal muscle fibers occurred 5 ms post-stimulation and persisted for 5 ms. The peak-to-peak voltage of the EMG shows a sigmoidal response as a function of stimulation intensity, shown in Figure 4.16(e), as expected [37]. The error bars indicate the measurement uncertainties from two rats and 10 samples each per stimulation amplitude. The minimum signal detected by the neural dust mote is approximately 0.25 mV, which is in good agreement with the noise floor measurement made in a water tank.

ENG recordings

A similar setup was prepared to measure the electroneurogram (ENG) response from the main branch of the sciatic nerve in anesthetized rats. The sciatic nerve was exposed by separating the hamstring muscles and the neural dust mote was placed and sutured to the nerve, with the recording electrodes making contact with the epineurium. We measured a similar graded response on both ground truth and wireless dust backscatter by varying stimulation current amplitude delivered to bipolar stainless steel electrodes placed in the foot as shown in Figure 4.17(a) and (b). The two signals at response-saturating stimulation amplitude (100%) matched with R = 0.886, shown in Figure 4.17(c); the average error was within $\pm$0.2 mV as shown in Figure 4.17(d). The peak-to-peak ENG voltage showed a sigmoidal response with the error bars indicating uncertainties from two rats and 10 samples each per stimulation amplitude. The minimum signal detected by the neural dust mote was again at 0.25 mV as shown in Figure 4.17(e).

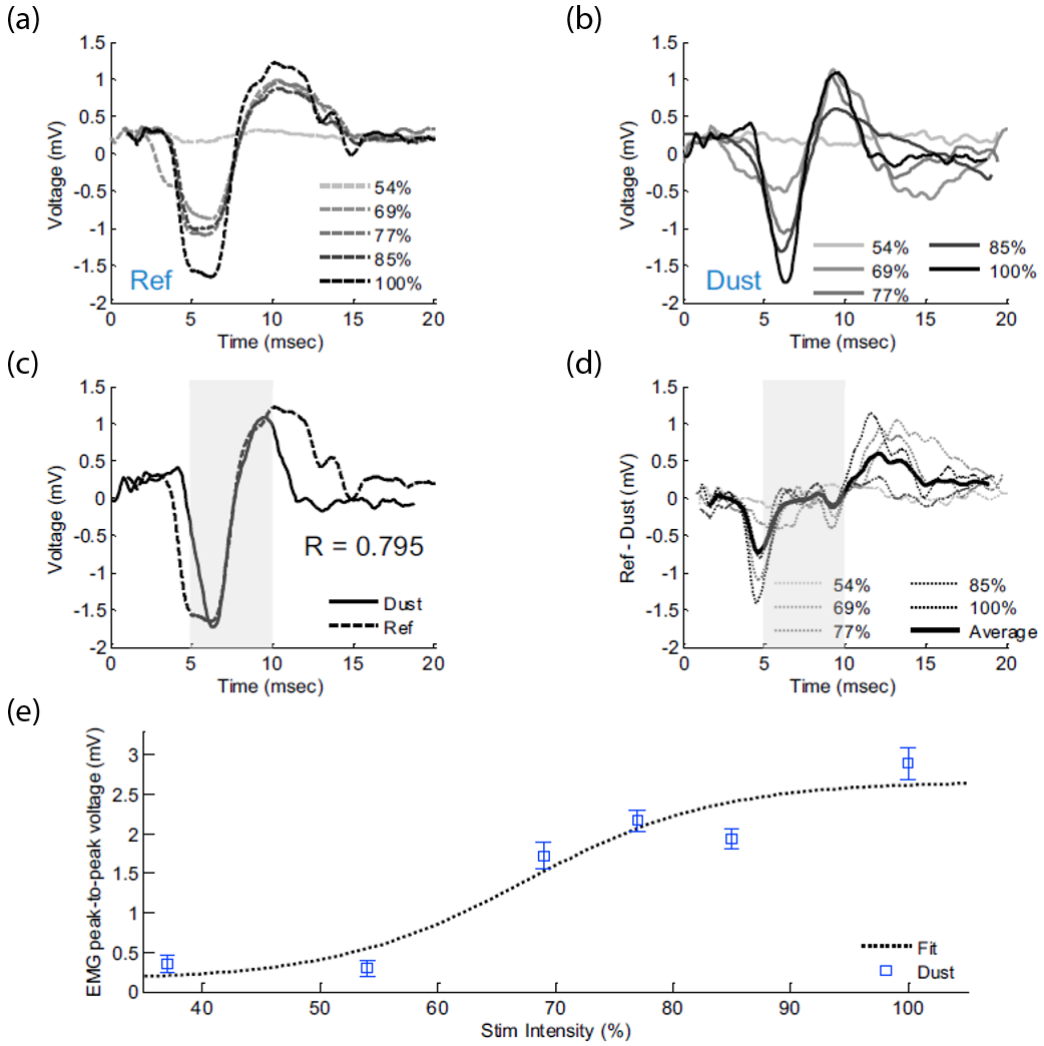

Figure 4.16: Tether-less neural dust rodent graded EMG. (a) Different intensities of EMG signals were recorded in-vivo with the electrodes on the PCB with varying stimulation intensities. (b) Similar gradient EMG responses were recorded wirelessly with the mote. (c) Ground truth and reconstruction of EMG signal from the wireless backscatter data at response-saturating stimulation amplitude (100%) matched with R = 0.795 (R = 0.60, 0.64, 0.67, 0.92 for 54%, 69%, 77%, 89%, respectively). (d) Quantitative comparison showed $<$ 0.4 mV match of the salient feature (shaded regions). (e) EMG peak-to-peak voltage showed an expected sigmoidal relationship with the stimulation intensity.

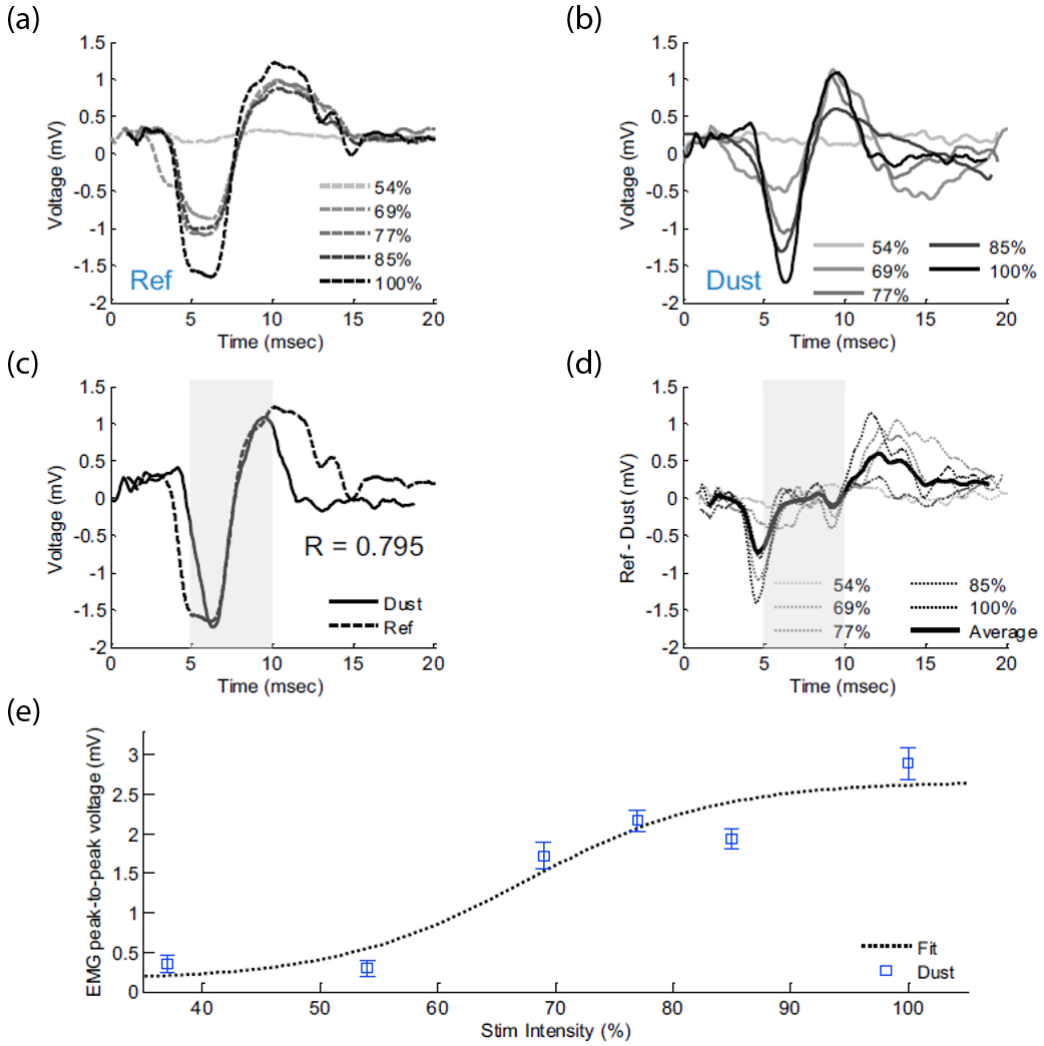

Figure 4.17: Tether-less neural dust rodent graded ENG. (a) Different intensities of ENG signals were recorded in-vivo with the electrodes on the PCB with varying stimulation intensities. (b) Similar gradient ENG responses were recorded wirelessly with the mote. (c) Ground truth and reconstruction of ENG signal from the wireless backscatter data at response-saturating stimulation amplitude (100%) matched with R = 0.886 (R = 0.822, 0.821, 0.69, 0.918, 0.87 for 44%, 61%, 72%, 83%, 89%, respectively). (d) Quantitative comparison showed < 0.2 mV match of the salient feature (shaded regions). (e) ENG peak-to-peak voltage showed an expected sigmoidal relationship with the stimulation intensity.

4.4 Conclusion

We designed, built, and implanted a wireless, ultrasonic neural sensor and communication system that enables neural recordings in the peripheral nervous system. In-vivo, acute recordings in a stationary, anesthetized rodent model was used to collect compound action potentials from the main branch of the sciatic nerve as well as evoked EMG from the gastrocnemius muscle. The performance of the neural dust system was equivalent to conventional electrophysiological recordings employing microelectrodes and cabled electronics.

One of the principal strengths of the demonstrated technology is that, unlike conventional radio frequency technology, ultrasound-based systems appear scalable down to < 100 μm sizes (see Chapter 3), opening the door to a new technological path in implantable electronics. However, a number of technical challenges remain open. The power levels used in this in-vivo study were limited by the specifications of commercially-available transducers; custom transducers will reduce the overall external device footprint, lower the noise floor (by producing higher power densities at the focal spot), and allow for selection of the focal depth to suit specific applications. For example, a flat, low-profile piezo-transducer with proper impedance matching would enable a wearable neural dust transceiver board small enough for awake, behaving rodent neurophysiology. Additionally, the development of wearable, battery-powered multi-element arrays would allow for beam-steering of the ultrasonic beam to enable multi-mote interrogation and the next chapter delves into the theoretical treatment of design tradeoffs in such beamforming systems.

Chapter 5

Interrogating Multiple Neural Dust Motes

In the previous chapters, we discussed the hardware implementation of neural dust (ND) system focused primarily on single-transceiver and single-neural dust mote (NDM) and demonstrated the capabilities of the transceiver module to perform beamforming to interrogate multiple neural dust motes in time-domain multiplexing (TDM) fashion. This chapter explores more in-depth analysis of cooperative beamforming approaches with multiple transceivers to enable multi-mote interrogation. We discuss the mathematical channel model of the ND system and perform simulations in MATLAB to compare the performance of two particular beamforming (BF) techniques: delay-and-sum (DAS) and linearly constrained minimum variance (LCMV) BF. We investigate whether the interference from other NDMs can be sufficiently mitigated to successfully identify neural signatures from each NDM. Furthermore, we examine spatial multiplexing to increase the overall throughput and consider a hierarchical processing flow to reduce the processing and communication burden for future hardware implementation of proposed BF systems.

5.1 Mathematical framework

Our model [8] simplifies the ND system to a 1D-grid as shown in Figure 5.1. A linear array of transceivers (assumed to be 1 mm in size), each containing multiple ultrasound transducers (TDs) to ensure far-field operation, transmits ultrasound waves to a grid of 100 μm neural dust motes (NDMs) at a depth of 2 mm in the neocortex (i.e., as motivated in Chapter 3). The spacing between transceivers is assumed to be 0.1 mm (i.e., equivalent to $\sim 0.66\lambda$ at the resonant frequency of 10 MHz) in order to maximize spatial coverage and to facilitate implantation.

We assume that the ultrasound signal $S_{kq}(t)$ received at the k-th NDM sent by the q-th

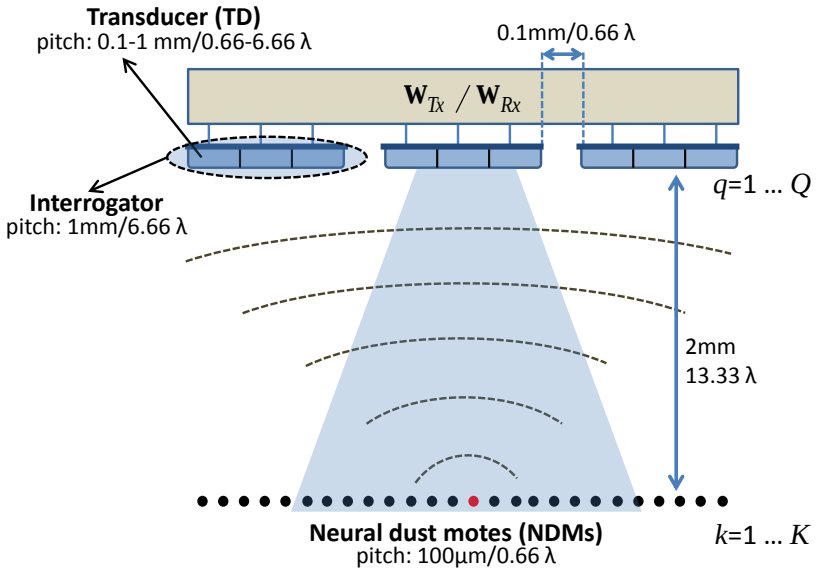

Figure 5.1: 1D simplification of the scaled neural dust system envisioned in Chapter 3, with transceivers consisting of a total of Q transducers interrogating K NDMs, where $Q < K$.

TD is modeled as

$$S_{kq}(t) = H_{kq} \cdot X_q(t) \tag{5.1}$$

where

$$H_{kq} = \theta(k,q) \cdot g(d_{kq}) \cdot e^{-j\frac{2\pi d_{kq}}{\lambda}} \tag{5.2}$$

and where

- d_{kq} is the distance between NDM k and TD q.
- $g(d_{kq})$ is a real-valued attenuation over the distance d_{kq}, based on the path loss constant α in brain tissue. The path loss of ultrasound in brain tissue is relatively small, and is typically in the range 0.3 – 1.2 dB/(cm·MHz) [96].
- $\theta(k,q)$ is a real-valued directivity gain factor, which depends on the shape and size of the TD. For a given transducer shape, the actual value of $\theta(k,q)$ varies with the angle between the frontal (maximum gain) direction of the TD, and the straight line between the k-th NDM and the q-th TD. The directivity gain function is assumed to be normalized such that $\theta = 1$ in the frontal direction.
- λ is the wavelength of the ultrasound carrier wave.

- $X_q(t)$ is the ultrasound signal transmitted by TD q in time-domain. We assume that $X_q(t)$ is a narrowband signal with a carrier frequency of f, e.g., $X_q(t) = \cos(2\pi f t)$.

Let $S_k(t)$ denote the signal that is picked up by the k-th NDM, containing the contribution from each transmitting TD, i.e.,

$$S_k(t) = \sum_{q=1}^{Q} H_{kq} \cdot X_q(t) = \mathbf{h}_k^T \mathbf{x}(t) \tag{5.3}$$

where Q is the total number of TDs (over all transceivers), the superscript T denotes the transpose operator, $\mathbf{x}(t)$ is a Q-dimensional vector where the q-th entry is defined as $X_q(t)$, and where $\mathbf{h}_k$ is a Q-dimensional vector where the q-th entry is defined as H_{kq}. Let $\mathbf{s}(t)$ denote the K-dimensional vector where the k-th entry is defined as $S_k(t)$, and where K is the total number of NDMs. We can then write the complete transmission model in a single matrix equation as

$$\mathbf{s}(t) = \mathbf{H} \cdot \mathbf{x}(t) \tag{5.4}$$

where $\mathbf{H}$ is a $K \times Q$ matrix where the k-th row is equal to $\mathbf{h}_k^T$. If TD q is silent at time t, we set the q-th entry in $\mathbf{x}(t)$ to zero.

The signal $S_k(t)$ are modulated by the measured neural signal $V_k(t)$ at the k-th NDM and the modulated signal $V_k(t) \cdot S_k(t)$ is backscattered with an omnidirectional reflection pattern.

Let $\mathbf{V}(t) = Diag\{V_1(t), \ldots, V_K(t)\}$ be a $K \times K$ diagonal matrix containing the neural signals of the different NDMs on its diagonal entries, where K is the total number of NDMs. Let $R_q(t)$ denote the signal that TD q observes when all the NDMs reflect their respective signal $V_k(t) \cdot S_k(t)$, $\forall\, k \in \{1, \ldots, K\}$, and define $\mathbf{r}(t)$ as the Q-dimensional vector where the q-th entry is defined as $R_q(t)$, where Q is the total number of TDs (over all transceivers). By reciprocity, the complete transmit-receive model can then be written as

$$\mathbf{r}(t) = \mathbf{H}^T \cdot \mathbf{V}(t) \cdot \mathbf{H} \cdot \mathbf{x}(t) + \mathbf{n}(t) \tag{5.5}$$

where the $(k, q)^{th}$ element of $\mathbf{H}$ in (5.5) is given by (5.2) and where $\mathbf{n}(t)$ represents added channel and receiver noise.

We are interested in extracting each diagonal element of $\mathbf{V}(t)$, i.e., all the neural signals of the individual NDMs. However, due to the double mixing process with the matrix $\mathbf{H}$, each TD signal in $\mathbf{r}(t)$ will consist of a mixture of the signals in $\mathbf{V}(t)$. To obtain a good estimate of the neural signals, we will apply beamforming techniques to reduce the interference from other NDMs.

In order to reduce the complexity of the problem, let us first assume that each NDM is excited with the same amount of ultrasound energy, i.e., $\mathbf{H} \cdot \mathbf{x}(t) = \mathbf{1}$, where $\mathbf{1}$ denotes the

all-ones vector. In this case, and assuming that the receiver noise power in $\mathbf{n}(t)$ is negligible, (5.5) reduces to

$$\mathbf{r}(t) = \mathbf{H}^T \cdot \mathbf{v}(t) \tag{5.6}$$

where $\mathbf{v}(t)$ is a K-dimensional vector where the k-th entry is defined as $V_k(t)$. The goal is to obtain the source signals in $\mathbf{v}(t)$ by applying a linear transformation on the observations in $\mathbf{r}(t)$. This corresponds to a linear demixing problem as commonly encountered in multi-channel or sensor array signal processing literature.

In general, the demixing problem can only be exactly solved if $Q \geq K$ (i.e., $\mathbf{H}^T$ is a tall matrix), and if it is not rank deficient (i.e., it has K non-zero singular values). In this case, a demixing matrix $\mathbf{D}$ should be chosen as the (pseudo-)inverse of $\mathbf{H}^T$ such that $\mathbf{D} \cdot \mathbf{r}(t) = \left(\mathbf{H}^T\right)^{-1} \cdot \mathbf{H}^T \cdot \mathbf{v}(t) = \mathbf{v}(t)$. If the entries of $\mathbf{H}$ are not known, the problem is often referred to as a blind source separation (BSS) problem. The BSS problem can be solved if the signals in $\mathbf{v}(t)$ satisfy certain conditions, such as independency, non-negativity, sparseness, etc. For example, the well-known independent component analysis (ICA) algorithm is able to find the signals in $\mathbf{v}(t)$ under the condition that they are statistically independent [45].

However, in the case of neural dust, the total number of transducers is typically smaller than the number of neural dust motes (NDMs) (i.e., $Q < K$), and therefore the mixing process cannot be inverted[1]. In this case, we have to settle for approximate solutions that aim to extract a particular signal from $\mathbf{v}(t)$ while minimizing the interference from the other NDMs (as well as from the noise in $\mathbf{n}(t)$ if this noise contribution is significant). One way to achieve this, is by using spatial filtering or beamforming (BF) approaches.

5.1.1 Tensor-based model

In the ultrasonic power and communication link, impedance mismatch at the input and output terminals of the channel can have a significant effect on the link efficiency. This loss factor strongly depends on the distance between the transceiver and the NDM, and therefore includes an extra directional dependency in the model. In order to compute this directional dependency, we calculate the transducer's power sensitivity in the receive (RX) mode (in ppm) for different TD-to-NDM distances. We incorporate the ppm value as a function of the distance as an extra real-valued gain factor shown in Figure 5.2.

However, unlike the KLM-based link model proposed in Chapter 3, which is a coupled one-to-one link between a single-TD and a single-NDM, the model in (5.5) explicitly decouples the transmit (TX) and receive (RX) signal path, where the TX TD and the RX TD can be

[1]By increasing the number of TDs per transceiver, the problem typically becomes more tractable since Q gets closer to K. However, there is still a fundamental limit which may hamper the design of an exact demixing process, even when $Q \approx K$. Indeed, if the spatial separation between the TDs is small, their signals will also become more similar. Although mathematically this may yield a mixing matrix $\mathbf{H}$ with K non-zero singular values, it will probably be numerically ill-conditioned (i.e., the number of singular values that are *significantly* larger than zero is still $\ll Q$). Due to unavoidable noise influences, this may again result in an underdetermined mixing problem.

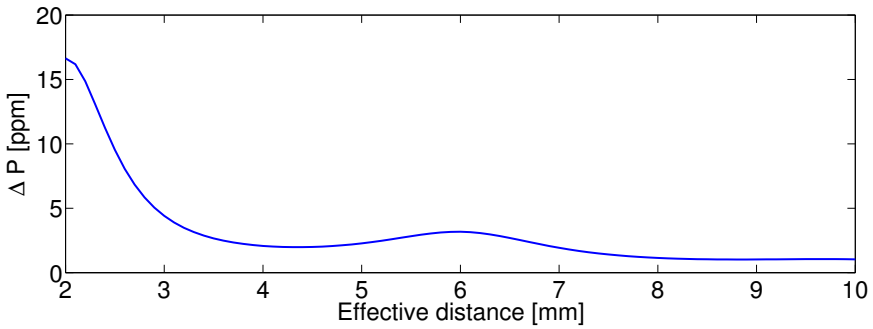

Figure 5.2: Change in the TD input power level during a spiking event (in ppm) as a function of the distance between the NDM and the TD [96] can be used to estimate directional dependency in the model.

different (they may even belong to different transceiver). As a result, losses due to impedance mismatch cannot be directly included in this model.

In order to adapt to the one-to-one link model, we compute the average effective distance $d = \frac{d_1+d_2}{2}$ where d_1 is the distance between the TX TD and the NDM and d_2 is the distance between the NDM and the RX TD. This distance is then used in the coupled one-to-one link model from described in Chapter 3, and we assume that the corresponding loss factor is representable for the decoupled link.

It is therefore necessary to build a 3-way tensor $\mathcal{H} \in \mathbb{C}^{K\times Q\times Q}$, where the entry H_{k,q_1,q_2} represents the (normalized) channel response for the signal $V_k(t)$ when TD q_1 is receiving and TD q_2 is transmitting. The entry H_{k,q_1,q_2} is then defined as (compare with (5.2))

$$H_{k,q_1,q_2} = \sqrt{\Delta P(d)} \cdot \theta(k,q_1) \cdot \theta(k,q_2) \cdot e^{-j\frac{2\pi(d_{kq_1}+d_{kq_2})}{\lambda_c}} \tag{5.7}$$

where

$$d = \frac{d_{kq_1} + d_{kq_2}}{2} \tag{5.8}$$

and where $\Delta P(d)$ denotes the change in the TD input power level during a spiking event for the effective distance of d after normalizing it to unity gain in the frontal direction (i.e., it is equal to 1 at an effective distance of 2 mm). Note that the energy link model that generates the ppm curve depicted in Figure 5.2 includes a worst-case path loss of 1.2 dB/(cm·MHz), and therefore a distance-dependent path loss, $g(d_{kq})$ is not explicitly added in (5.7).

In the subsequent sections, unless stated otherwise, all simulation results are obtained using the more accurate tensor-based model in (5.7). However, for the sake of simplicity, we will usually refer to the explicit model in (5.2) to describe various beamforming approaches.

5.2 Beamforming approaches

Beamforming is a widely used sensor array processing technique that exploits spatial coherence between multiple sensor or transducer signals to suppress interference [107]. The transceiver of the ND system can apply beamforming in transmit as well as receive mode.

Transmit (TX) beamforming

To apply transmit beamforming, the transmitting TDs will transmit the same carrier wave $X(t)$, but each with a different complex scaling factor. By carefully choosing these scaling factors (or beamforming coefficients), we can focus the transmission energy towards a target NDM, such that the other (interfering) NDMs have less influence in (5.5). To this end, we rewrite (5.5) as

$$\mathbf{r}(t) = \mathbf{H}^T \cdot \mathbf{V}(t) \cdot \mathbf{H} \cdot \mathbf{w}_{\mathrm{TX}}^* \cdot X(t) \; . \tag{5.9}$$

where the superscript $*$ denotes the complex conjugate[2], $\mathbf{w}_{\mathrm{TX}}$ is a complex-valued vector containing the beamforming gains for each TD transmission signal, and where $X(t)$ is a common carrier wave, which is the same in all TDs, e.g.,

$$X(t) = \cos\left(2\pi f_c t\right) \; . \tag{5.10}$$

In the sequel, we will always work on the demodulated signals, and therefore, we will set $X(t) = 1$ to simplify the equations.

Ideally, if we want to read out the signal $V_k(t)$ from the k-th NDM, we aim for

$$\mathbf{H} \cdot \mathbf{w}_{\mathrm{TX}}^* \approx \mathbf{e}_k \tag{5.11}$$

where $\mathbf{e}_k$ is an all-zero vector, except for its k-th entry, which is 1. This would mean that only the k-th diagonal element in $\mathbf{V}(t)$ is excited such that there is no interfering reflection from any other ND node. Note that (5.11) is an overdetermined system of equations (in the unknown variables in $\mathbf{w}_{\mathrm{TX}}$), hence it has no exact solution.

Receive (RX) beamforming

When the TDs are in receive mode, each of them observes the superimposed reflections from the different NDMs. By linearly combining the different TD signals in $\mathbf{r}(t)$ with carefully chosen complex weights, we can perform spatial filtering to extract the signal(s) coming from a pre-defined direction. Assume we want to extract the signal $V_k(t)$ from the k-th NDM, then we should apply a beamformer $\mathbf{w}_{\mathrm{RX}}$ such that

$$\mathbf{w}_{\mathrm{RX}}^H \mathbf{H}^T \approx \mathbf{e}_k \tag{5.12}$$

[2]It is noted that, by definition, we use the complex conjugate of the vector $\mathbf{w}$ as the actual beamformer, rather than the vector $\mathbf{w}$ itself.

where the superscript H denotes the conjugate transpose operator. Note that, by reciprocity, the RX and TX beamformers are essentially targetting the same objective (compare (5.11) and (5.12)), and can therefore be chosen equal. However, RX beamforming has an additional advantage that it can first observe the received signals and based on the RX signal statistics, determine the optimal beamformer to extract the target source. This allows for more advanced approaches, such as the linearly constrained minimum variance (LCMV) beamformer, which can optimize its BF coefficients to the interference pattern (see Subsection 5.2.2). On the other hand, TX beamformers typically have to be designed a priori (offline).

5.2.1 Delay-and-sum (DAS) beamforming

DAS BF is the easiest form of beamforming, and it can be applied for both TX BF and RX BF. It applies a delay or phase shift to each signal in the transceiver to create constructive interference in the target direction [107], i.e.,

$$\mathbf{w} = \begin{bmatrix} e^{j\phi_1} \\ \vdots \\ e^{j\phi_Q} \end{bmatrix} \tag{5.13}$$

where the ϕ_q's are well-chosen phase shifts.

This approach relies on the assumption that the amplitude of the target signal is approximately the same[3] in all sensors (far-field assumption). Note that trade-offs between beamwidth and sidelobe levels are possible by also scaling each individual signal with a real-valued coefficient.

When applying DAS BF in the RX BF mode to the received TD signals in $\mathbf{r}(t)$ in order to interrogate the k-th NDM, we compute the BF output signal

$$z(t) = Re\{\mathbf{w}_{\mathrm{RX}}^H \mathbf{r}(t)\} \tag{5.14}$$

where

$$\mathbf{w}_{\mathrm{RX}} = \Phi\{\mathbf{h}_k\} \tag{5.15}$$

with $\mathbf{h}_k$ denoting the k-th column of $\mathbf{H}^T$, $Re\{z\}$ denoting the real component of a complex number z, and where the operator $\Phi\{\mathbf{z}\}$ replaces each complex entry in $\mathbf{z}$ by the closest complex number on the unit circle, i.e., $\Phi\{z(n)\} = z(n)/|z(n)|$. Note that the conjugation of $\mathbf{w}_{\mathrm{RX}}$ in (5.14) basically inverts the phase shift applied by $\mathbf{H}^T$ such that the inner product $\mathbf{w}_{\mathrm{RX}}^H \mathbf{h}_k$ results in a real number, i.e., in-phase addition. By reciprocity, the DAS TX BF is chosen equal to (5.15).

The main advantage of DAS BF is the fact that it is computationally cheap, and that it is less sensitive to modeling errors in $\mathbf{h}_k$ compared to optimal beamformers (see, e.g., Subsection 5.2.2). However, DAS beamformers are determined a-priori, i.e., they cannot

[3]DAS BAF may still work if this assumption is violated, but performance generally drops compared to the case where all signals have a similar signal-to-noise ratio (SNR).

adapt to the actual interference pattern. As a result, in the worst-case, the main and sidelobes may capture a significant amount of interference and unable to achieve sufficiently high SNR.

5.2.2 Linearly constrained minimum variance (LCMV) beamforming

LCMV BF is a beamformer that adapts its beam shape to the interference pattern, by using knowledge of the second-order statistics of the signals at the receiver [107]. It can therefore only be applied in RX BF. Consider a general sensor array where the different sensor signals $y_1(t)$, ..., $y_Q(t)$ are stacked in the vector $\mathbf{y}(t)$, then the goal is to optimize the BF coefficients such that the variance of the BF output signal is minimized, subject to a set of linear constraint(s). These linear constraints are used, e.g., to obtain a unity gain in a target direction, or to steer a null towards interfering sources. The single-constraint LCMV BF is defined as (assuming zero-mean signals)

$$\mathbf{w}_{\mathrm{RX}} = \arg\min_{\mathbf{w}} \left(E\{|\mathbf{w}^H \mathbf{y}(t)|^2\}, \text{ s.t. } \mathbf{w}^H \mathbf{h} = 1 \right) \tag{5.16}$$

where $E\{\cdot\}$ denotes the expected value operator (taken over the full signal length), and where $\mathbf{h}$ contains the channel responses from the target source to the Q sensors. The closed-form solution of expression (5.16) is

$$\mathbf{w}_{\mathrm{RX}} = \frac{\mathbf{R}_{yy}^{-1}\mathbf{h}}{\mathbf{h}^H \mathbf{R}_{yy}^{-1}\mathbf{h}} \tag{5.17}$$

where $\mathbf{R}_{yy} = E\{\mathbf{y}(t) \cdot \mathbf{y}(t)^H\}$ is the sensor signal covariance matrix.

In the ND system, we will set $\mathbf{y}(t) = \mathbf{r}(t)$. To interrogate the k-th NDM, we should set $\mathbf{h} = \mathbf{h}_k$, where $\mathbf{h}_k$ is the k-th column of $\mathbf{H}^T$ in (5.2), such that the BF response $\mathbf{w}_{\mathrm{RX}}^H \mathbf{h}_k = 1$. The LCMV beamformer output is then given by

$$z(t) = Re\{\mathbf{w}_{\mathrm{RX}}^H \mathbf{r}(t)\} \, . \tag{5.18}$$

LCMV beamforming is optimal in the sense that it automatically adapts to the scenario and removes as much interference energy as possible, without removing the target signal (due to the unity-response constraint). It also automatically takes circuit or biological noise into account.

However, the interference cancellation by the LCMV BF makes it also very susceptible to errors in the steering vector $\mathbf{h}$. Indeed, errors in $\mathbf{h}$ would mean that the LCMV beamformer is steered off-target, and it may then consider the actual target signal as an interferer and hence try to remove it. A good estimate of $\mathbf{h}$ is therefore crucial, as errors in the channel model may result in significant performance degradation. Note that obtaining a good estimate of $\mathbf{h}$ may be non-trivial in the neural dust system (due to heterogeneity of the brain tissue medium,

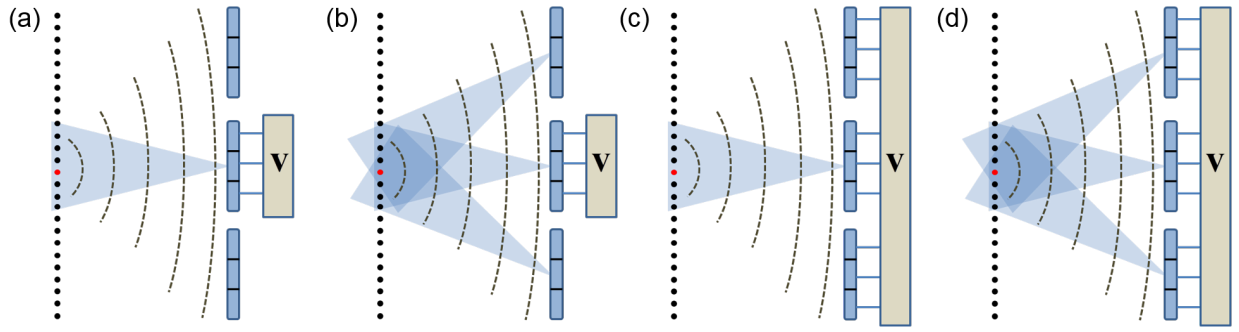

Figure 5.3: Different cooperative beamforming modes exist for TX and RX for TX and RX (a) single-TX and single-RX (single-to-single) (b) multiple-TX and single-RX (all-to-single) (c) single-TX and multiple-RX (single-to-all) (d) multiple-TX and multiple-RX (all-to-all).

blood vessels, micromotions, etc.). A good channel estimation procedure (preferably on-line) will therefore be an important ingredient when using LCMV BF.

Fortunately, there exists several methods to reduce its sensitivity to such errors in the steering vector $\mathbf{h}$ (e.g., overview of different techniques in [61]). The simplest approach is to apply a regularization term to $\mathbf{R}_{yy}$, i.e.,

$$\mathbf{R}_{yy} = E\{\mathbf{y}(t) \cdot \mathbf{y}(t)^H\} + \sigma\mathbf{I} \tag{5.19}$$

where $\mathbf{I}$ denotes the identity matrix, and where σ is a small non-negative number. σ will then introduce a trade-off between steering vector sensitivity and interference cancellation. Note that, if $\sigma \to \infty$, we find from (5.17) that $\mathbf{w}_{\mathrm{RX}} \to \gamma\mathbf{h}$ (with γ a real-valued scalar), such that (5.18) becomes equivalent to applying a DAS BF (except for the fact that DAS uses $\Phi\{\mathbf{h}\}$, i.e., it does not take the signal attenuation into account, whereas $\mathbf{h}$ does). It can also be viewed as a spatial matched filter.

Note that the choice of σ in (5.19) will strongly depend on the signal power in $\mathbf{y}(t)$. Therefore, we will use a slight modification to make the choice of σ less signal-dependent:

$$\mathbf{R}_{yy} = E\{\mathbf{y}(t) \cdot \mathbf{y}(t)^H\} + \sigma \cdot \gamma_y \cdot \mathbf{I} \tag{5.20}$$

where γ_y is the sum of the variance of all the signals in $\mathbf{y}(t)$, divided by the number of signals in $\mathbf{y}(t)$. By including this 'averaged signal variance' γ_y, the amount of regularization will scale with the signal power, without having to increase σ.

5.2.3 Different beamforming configurations

As shown in Figure 5.3, we can define four cooperative BF configurations:

- A single transceiver creates the TX beam in transmit mode, and the same transceiver also creates the RX beam in receive mode (*single-to-single*, see Figure 5.3(a)).

- All transceivers jointly create the TX beam in transmit mode, and only one transceiver creates the RX beam in receive mode (*all-to-single*, see Figure 5.3(b)).
- A single transceiver creates the TX beam in transmit mode, and all transceivers jointly create the RX beam in receive mode (*single-to-all*, see Figure 5.3(c)).
- All transceivers jointly create the TX beam in transmit mode, and all transceivers jointly create the RX beam in receive mode (*all-to-all*, see Figure 5.3(d)).

5.3 Performance measures

For the simulations in the subsequent sections, the signals $V_k(t)$ consist of (uncorrelated) artificial spike signals with a signal-to-noise ratio (SNR) of 0 dB, as shown in Figure 5.4. We scale this signal to 10 μV amplitude recorded on the NDM and resulting 16 ppm change in the received power at the 1 mm transceiver (as detailed in Chapter 3). If the full array of TDs in a transceiver transmits a nominal power of 7.2 mW (100% FDA limit), then each individual TD observes a difference in RMS signal voltage of

$$V_{\mathrm{RX}} = \sqrt{R\frac{0.0072}{N}16 \cdot 10^{-6}} \tag{5.21}$$

where R is the impedance of an individual transducer, and where N is the number of transducers on a 1 mm transceiver.

Based on these signals, we compare the performance of the beamformer to remove interference from neighboring NDMs based on three different performance metrics: signal-to-error ratio (SER), spike misdetection rate (MDR) and false discovery rate (FDR). In the sequel, we will mostly use the SER to assess the performance of the BFs, because it is less dependent on the signal content, and directly measures the amount of interference. The MDR and FPR are both indirect measures in the actual beamforming context, but they are of direct importance in a brain-machine-interface context as discussed below.

5.3.1 Signal-to-error ratio (SER)

The SER quantifies the total amount of noise or interference that is added by the ultrasound interrogation process, i.e., how much the BF output signal $z_k(t)$ differs from the actual signal $V_k(t)$ that is recorded at a specific k-th NDM. Assuming $z_k(t)$ and $V_k(t)$ are zero-mean signals (no DC component), then the SER is defined as

$$\mathrm{SER}_k = 10 \cdot \log_{10} \frac{E\{V_k(t)^2\}}{E\{(V_k(t) - z_k(t))^2\}} \tag{5.22}$$

where $z_k(t)$ is scaled such that its signal component from the k-th NDM has the same amplitude as $V_k(t)$, i.e., the BF coefficients are normalized such that they observe $V_k(t)$ with

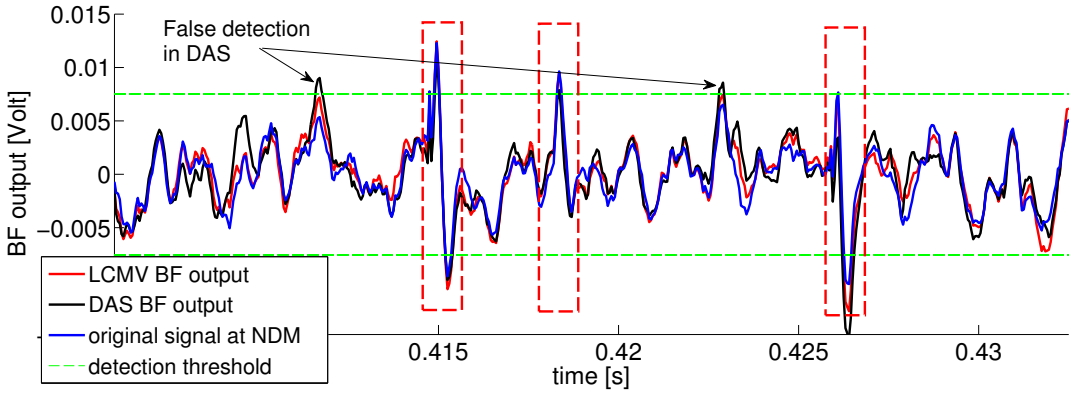

Figure 5.4: BF output signal $z_k(t)$ compared to the original neural signal $V_k(t)$. Dashed boxes indicate actual spikes.

unity gain. The SER can be viewed as an SNR measure where the noise component is defined as the difference between the target signal $V_k(t)$ and the BF output. It therefore accounts for interference due to other NDMs, as well as circuit noise at the receiver. However, it does not capture noise statistics in the neuronal spike signal, i.e., it only measures noise added *after* recording $V_k(t)$ at the NDM.

5.3.2 Spike misdetection rate (MDR) and false discovery rate (FDR)

The interference from neighboring NDMs degrades the quality of the observed neural signals at the transceiver, which may influence the performance of post-processing algorithms such as spike detection or spike sorting. As a first attempt to quantify this effect, we have implemented a spike detection algorithm, based on a simple thresholding[4], combined with a removal of detected spikes that violate a certain minimum refractory period of 1.5 ms [74]. The threshold is optimally chosen using prior knowledge of the spike positions, such that the FDR is minimized, while guaranteeing that both the FDR and MDR[5] are below a value of 30%. This threshold is computed on the original $V_k(t)$ signals as well as on the BF output at the transceiver. Any increase in MDR or FDR is then due to the additional interference during the transmission from the NDM to the transceiver.

Note that the resulting MDR and FDR performance measures should be viewed as a relative measure, rather than absolute number, merely metrics to investigate performance degradation compared to the case where we would have direct access to the recorded signals $V_k(t)$ at the NDM itself.

[4]A good overview of more sophisticated spike detection and sorting algorithms can be found in [88]

[5]MDR=FN/(TP+FN) and FDR=FP/(TP+FP) where FN, FP, and TP denote the number of false negatives, false positives and true positives, respectively.

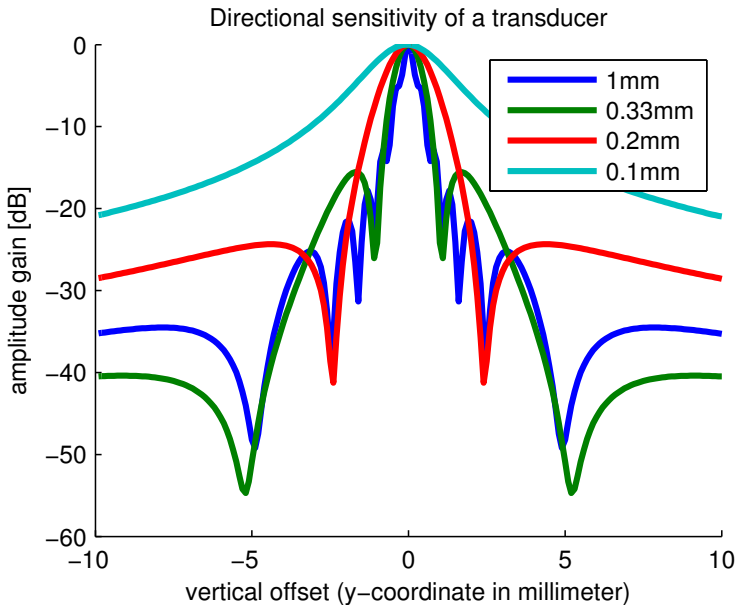

Figure 5.5: Directional gain for square planar transducers of different sizes shows that larger TDs have a more narrow response.

5.4 Sequential interrogation

5.4.1 Effect of transducer size

We assume each transducer in the transceiver to be square of varying sizes, for which the directivity pattern can be computed using numerical simulation software [42]. The normalized directional gain θ, as used in (5.2) is shown in Figure 5.5 for TDs with a surface of 1 mm^2, 0.33 mm^2, 0.2 mm^2, and 0.1 mm^2, as a function of the vertical offset between the NDM and the TD with the fixed transmission distance of 2 mm as shown in Figure 5.1. We note that the directional sensitivity decreases if the TD size decreases (large TDs have a more narrow response).

Decreasing the TD size has several implications. First, more TDs fit within a 1 mm transceiver, and hence we have more degrees of freedom for beamforming (the dimension of $\mathbf{w}_{\mathrm{TX}}$ and $\mathbf{w}_{\mathrm{RX}}$ increases in (5.9) and (5.12). However, the increase in the density of TDs require a substantially larger processing power as the LCMV processing power increases quadratically with the number of input channels. Second, the wider response of each individual TD allows us to steer the beam in a larger angle with respect to the frontal direction. As a result, larger spatial coverage can be achieved with smaller TDs. The increased spatial coverage, however, implies that each TDs captures more interference from neighboring NDMs due to their wider accepting angles. Substantial decrease in SER can therefore result in the inability to extract signals from the desired NDM.

As another illustration of the influence of TD size, Figure 5.6 shows the spatial covariance or correlation matrix between the signals received at the different TDs in a single-to-all BF

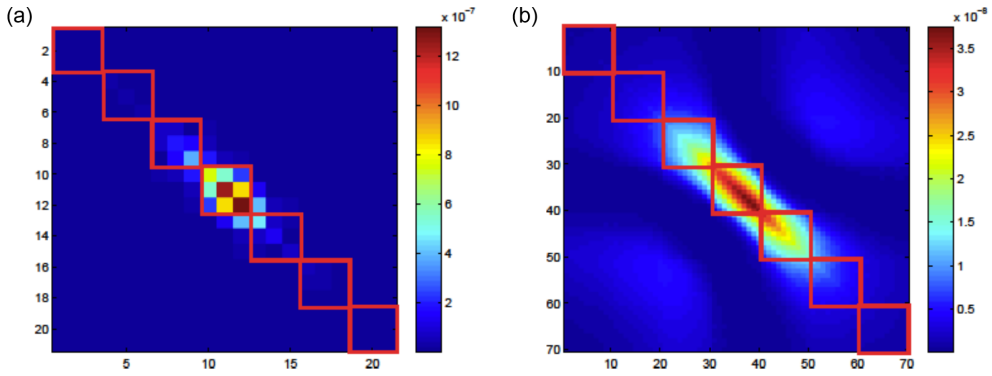

Figure 5.6: Spatial covariance/correlation matrix between the received signals at (a) 0.33 mm^2 and (b) 0.1 mm^2 TDs in a single-to-all BF configuration.

configuration, i.e., the absolute value of the coefficients of the entries in $\mathbf{R}_{yy}$ in (5.17) (the transceiver in the middle alone transmits the TX beam). The submatrices indicated by the red boxes correspond to the local covariance or correlation at each particular transceiver[6]. This demonstrates that, in the case of 0.1 mm^2 TDs, there is more cross-correlation between the different transceivers compared to the case of 0.33 mm^2 TDs.

Given the tradeoffs described above, unless stated otherwise, we assume 0.33 mm^2 TDs for simulation results.

5.4.2 Comparison of DAS vs. LCMV in the four beamforming configurations

Figure 5.7(a) and Figure 5.7(b) demonstrate the benefit of using LCMV BF over DAS BF when single-to-all BF configuration with 0.33 mm^2 TDs are used. The BF response of LCMV is much sharper since it optimizes its BF coefficients to minimize the amount of interference energy captured by its main beam and/or its side lobes. The DAS BF cannot adapt its beam shape to the scenario, and therefore the reflections from interfering NDMs are less attenuated, in particular those that also fall within the main beam. Note that the LCMV BF can only be applied in receive mode, i.e., both cases use DAS BF in transmit mode.

We show the performance of LCMV and DAS in different beamforming configurations in Figure 5.8. In both cases, we observe that the single-to-single configuration cannot sufficiently suppress the interference and result in a significant decrease in spike detection performance. This means that cooperation between transceivers is crucial for the RX beam. Interestingly, we observe that single-to-all configuration works better than all-to-all. This is because the interrogators are separated by more than $\lambda/2$ (i.e., sub-sampling) and 0.33 mm^2 TDs are very directional, which makes it difficult for a neighboring transceivers to steer a

[6]Note that the single-to-single BF configuration only exploits the covariance or correlation in one of these boxes.

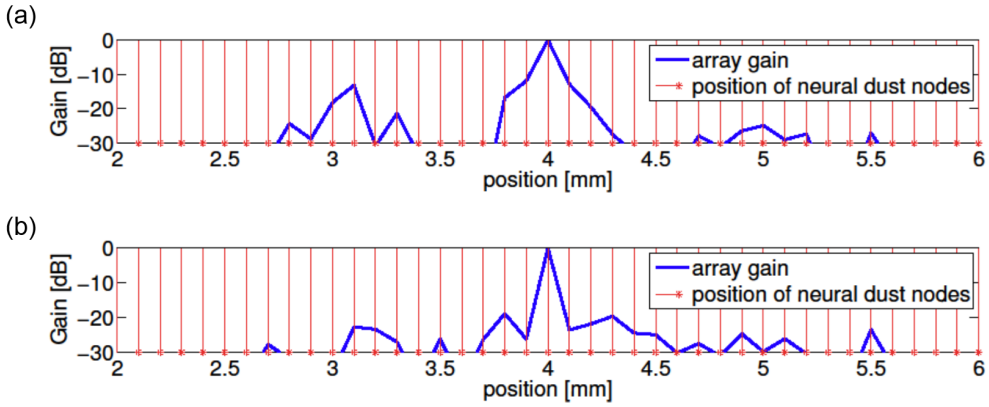

Figure 5.7: Beam pattern of the (a) DAS - SER=6.06 dB, MDR=27.2%, FDR = 45.8% (b) LCMV - SER=10.34 dB, MDR = 27.2%, FDR = 32.9%.

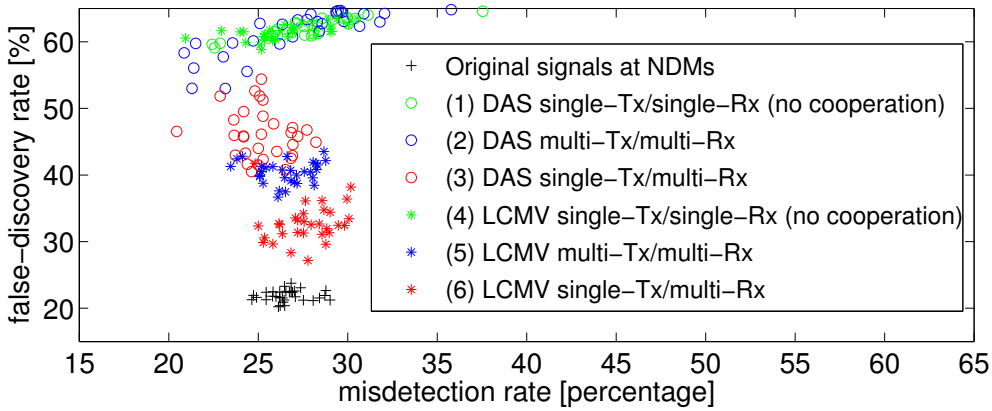

Figure 5.8: Comparison between LCMV, DAS, and TX/RX BF config for 0.33 mm-size TDs. Different points correspond to signals from different NDMs.

sidewards TX beam towards a NDM that is not in the frontal direction. This will only create more interfering backscatter from other NDMs. Although this effect diminishes and eventually vanishes for sufficiently small TDs, the single-to-all configuration is never significantly outperformed by the all-to-all configuration.

The time-domain trace of the DAS and LCMV BF output in Figure 5.4 compared to the original signal $V_k(t)$ (in blue) show some false detections as reflected in the MDR/FDR plot of Figure 5.8

5.4.3 Sensitivity to receiver noise

The results shown in the previous sections assume the RMS value of the thermal noise in each transducer signal to be

$$V_{\mathrm{T}} = \sqrt{4 \cdot 4 \cdot 10^{-21} \cdot R \cdot 10000}. \tag{5.23}$$

where 10000 denotes an operating bandwidth of 10kHz and R is the impedance of an individual transducer. Figure 5.9 shows the effect of receiver noise for different SNR levels, where SNR level is defined as the RMS voltage ratio between the received signal from a *single* NDM at 2 mm distance from the TD, and the temporally white noise added at the RX TD. We observe that unless the power of the receiver noise is significantly increased, it hardly influences the BF performance. This is because the amount of interference due to reflections of nearby NDMs is much larger than the circuit noise at the receiving transducers.

For the LCMV beamformer, receiver noise noise is implicitly included in $\mathbf{R}_{yy}$. Figure 5.10 shows the effect of the LCMV beamformer coefficients in $\mathbf{w}_{\mathrm{RX}}$ for different SNR levels. It can be shown that, if SNR$\rightarrow -\infty$, the LCMV beamformer coefficients will converge to $\mathbf{w}_{\mathrm{RX}} \rightarrow \mathbf{h}$, i.e., the LCMV beamformer will become equal to the steering vector. This is because the receiver noise is assumed to be spatially uncorrelated, such that an increase of the receiver noise floor can be modeled as the addition of a scaled identity matrix to $\mathbf{R}_{yy}$. Therefore, receiver noise has a regularization effect, similar to (5.20). As explained in Subsection 5.2.2, the steering vector $\mathbf{h}$ is then obtained in the limit case. However, this effect will probably hardly be noticable with realistic noise floors.

5.4.4 Sensitivity to model parameters

As mentioned earlier, one of the most important drawbacks of LCMV beamforming is its high sensitivity to steering errors, i.e., errors in the steering vector $\mathbf{h}$. If the LCMV BF is not exactly on-target, it may treat the target source as an interfering source and try to remove it, which may have a substantial effect on the performance.

We introduce mismatch in the channel model parameters to assess its impact on the performance of the LCMV BF. Specifically, we investigate the influence of errors on two model parameters: the speed of sound c and the path loss constant α. It is noted that the simulations in this subsection do not incorporate the effect of impedance mismatch, i.e., we use the simple model (5.2), rather than the semi-black box model described in (5.7) since α is incorporated in the semi-black box model and cannot be modified.

We assume the nominal values of c and α to be $c = 1540$ m/s and $\alpha = 0.5$ dB/(cm·MHz). We observe that the uncertainty in the model parameters has two adverse effects on the LCMV BF. First, there is an error in the LCMV steering vector $\mathbf{h}$ in (5.16), since $\mathbf{h}$ is set to $\mathbf{h} = \mathbf{h}_k$ where $\mathbf{h}_k$ is constructed based on a wrong model. Second, uncertainty in c can result in phase mismatch at the target NDM (i.e., $\mathbf{w}_{\mathrm{TX}}^H \mathbf{h}_k$ is not a real number) and significantly degrade the performance of LCMV BF.

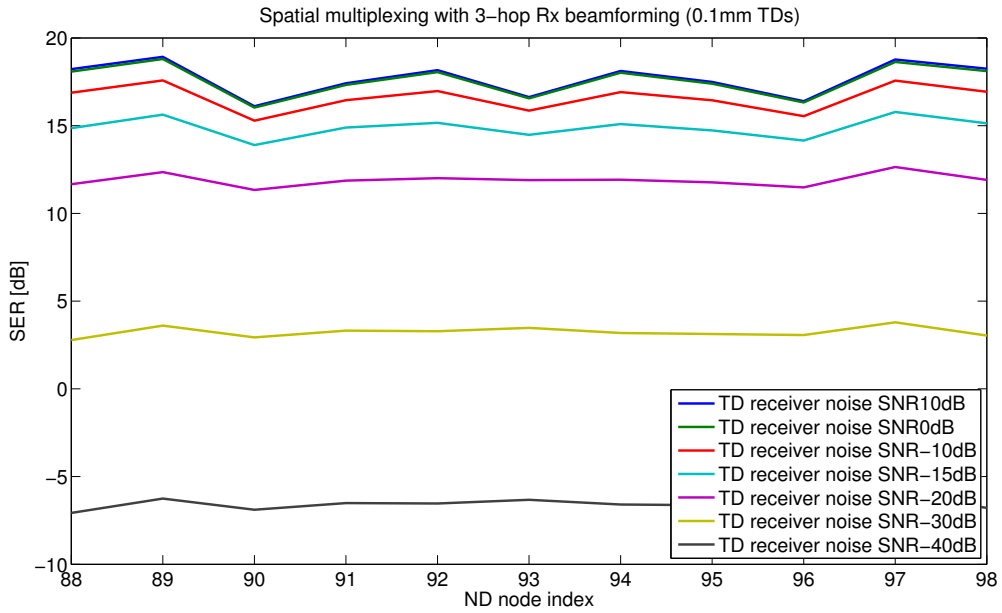

Figure 5.9: SER of BF output for different SNR levels of receiver noise (0.1 mm^2 TDs, single-to-all LCMV).

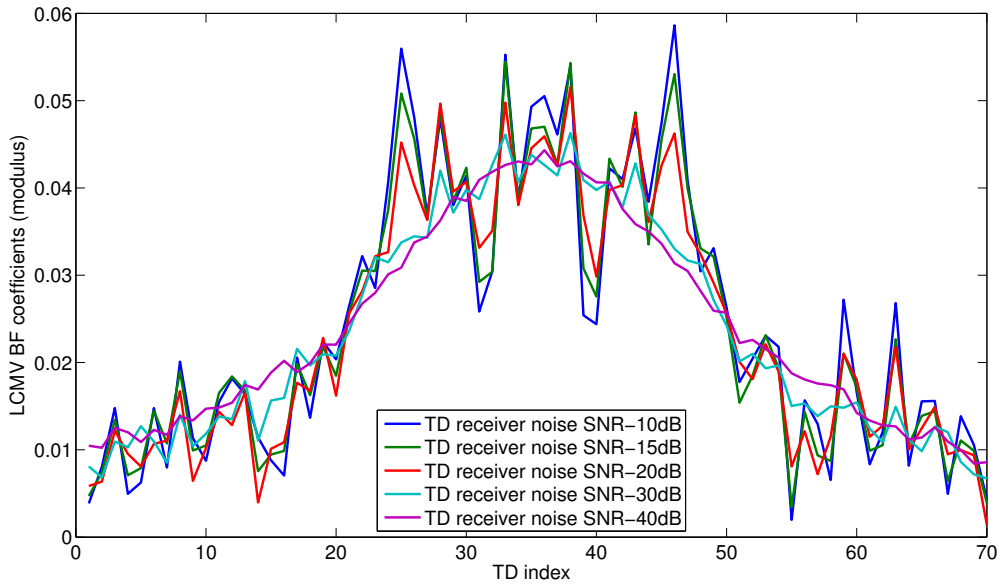

Figure 5.10: LCMV beamformer coefficients in $\mathbf{w}_{\mathrm{RX}}$ for different SNR levels of receiver noise (0.1 mm^2 TDs, single-to-all LCMV).

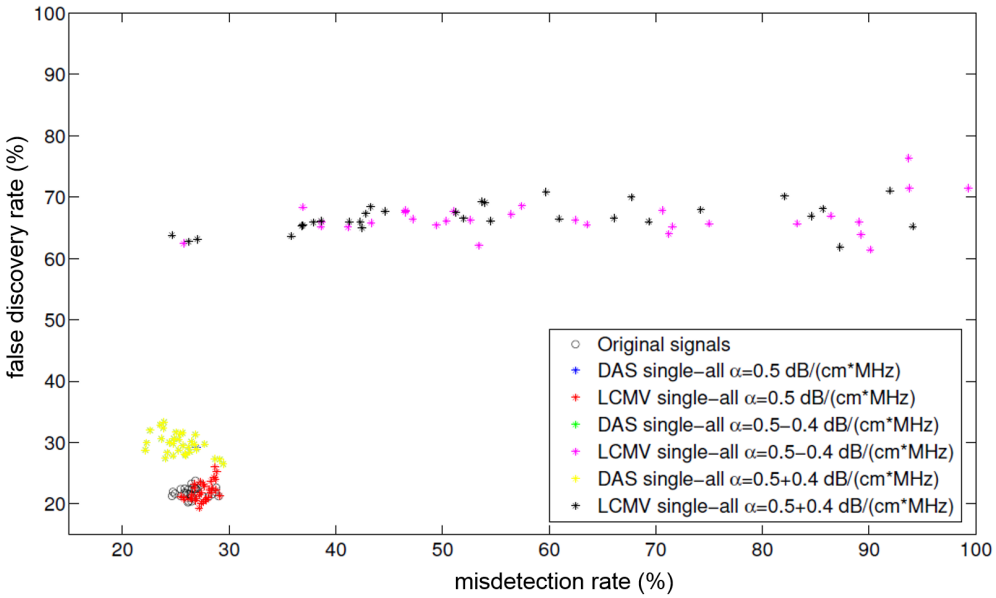

Figure 5.11: Influence of uncertainty in the path loss constant α on the performance of LCMV beamforming.

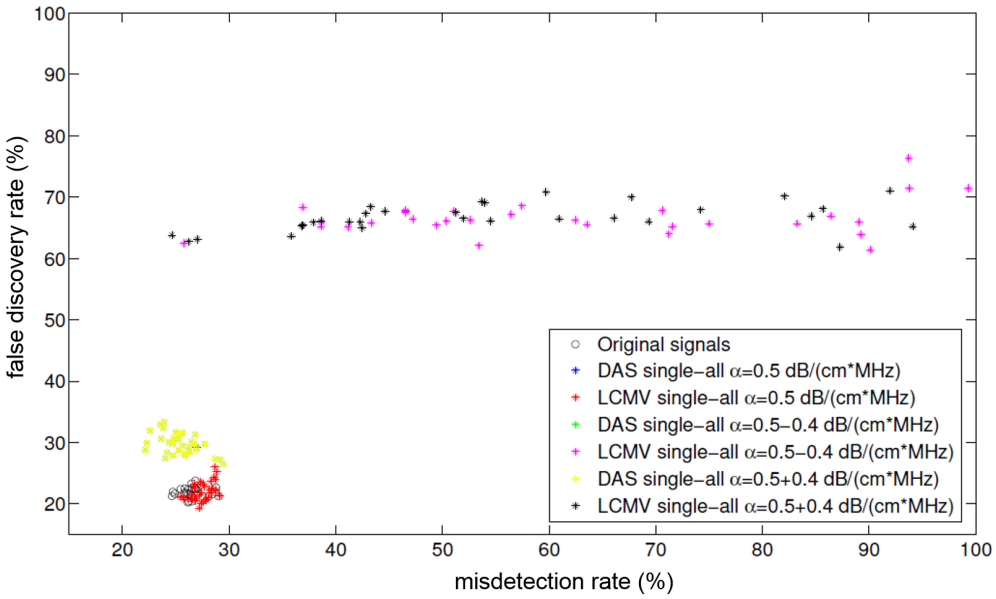

Figure 5.12: Influence of uncertainty in the speed of sound c on the performance of LCMV beamforming.

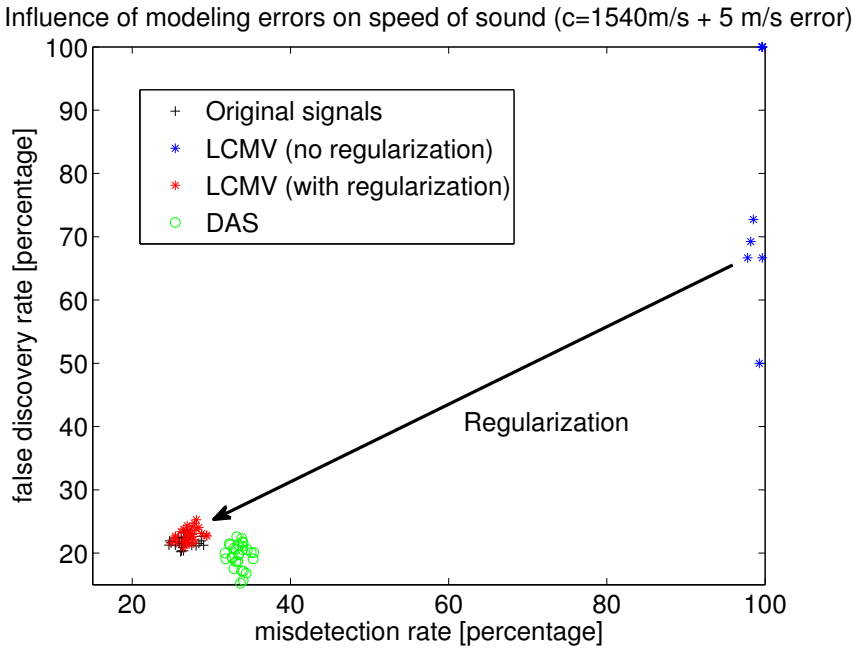

Figure 5.13: Sensitivity to model mismatch of DAS and (regularized) LCMV BF for 0.1 mm-size TDs.

Figure 5.11 shows the influence of errors in the path loss constant α in a single-to-all BF configurations with 0.1 mm^2 TDs. We observe that the model mismatch in the path loss α significantly reduces the performance of the LCMV BF, whereas the DAS BF is almost unaffected. Note that these effects are somewhat exaggerated since errors of 80% of the nominal value of α are applied here. However, model mismatch with respect to c has a more dramatic effect, as demonstrated in Figure 5.12. In this case, even a slight error of less than 5% of the nominal value of c results in a useless LCMV BF output signal, whereas the DAS BF is only marginally affected.

Fortunately, as explained in Subsection 5.2.2, the LCMV BF can be robustified against steering errors by applying regularization (or other techniques outlined in the subsection). Figure 5.13 shows the improvement in the performance of the LCMV BF after applying relaxation for c. Intuitively, regularization shifts the LCMV BF coefficients closer to the DAS BF coefficients, which is less sensitive to the uncertainty in the model parameters.

5.5 Simultaneous interrogation

In the previous simulations, we looked into the case where all transceivers dedicate their resources to the interrogation of one particular NDM. Multiple NDMs can then be interrogated by time-multiplexing, where in each time slot, the transceivers focus on a different NDM as previously discussed. The minimum amount of time needed to collect one sample of $V_k(t)$, i.e., the neural signal recorded by the k-th NDM, will depend on the transit time

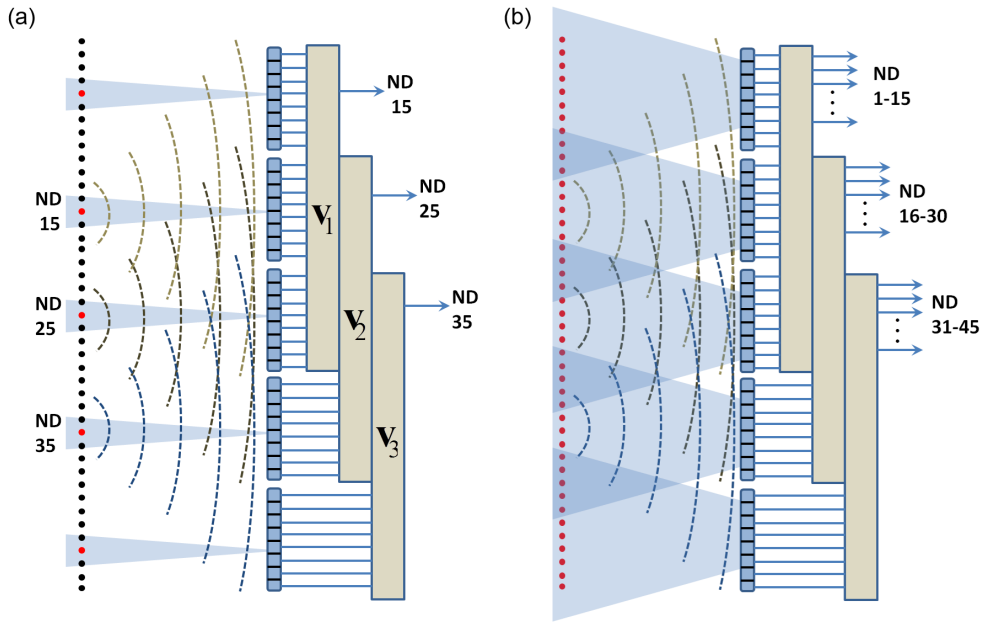

Figure 5.14: Spatial multiplexing with (a) per-transceiver TX BF (only one NDM per transceiver is interrogated simultaneously), and 1-hop RX beamforming and (b) without TX beamforming (all NDMs are interrogated simultaneously), and 1-hop RX beamforming.

of the transmitted ultrasound wave. As a concrete example, let us assume a single-to-all BF configuration, where all the transceivers within a 2 mm radius[7] of the TX transceiver are used to form the RX beam. Given the speed of sound in water, the worst-case transit time of the ultrasound wave is approximately 6 μs, which represents the length of one time slot when interrogating multiple NDMs using time-division multiplexing (TDM). Assuming that each recorded neural signal $V_k(t)$ has to be sampled at 20 kHz, then we will need 20,000 time slots per NDM per second, or 0.12 seconds per NDM. This means that the subset of interrogators can continuously read out the data of 8 NDMs. This roughly corresponds to 8 NDMs per 10 interrogators (assuming a 2D-grid with 1 mm^2 interrogators), which is not much, considering the fact that 100 μm^2 ND nodes and 1 mm^2 interrogators yields a ratio of roughly 10 ND nodes per interrogator in a 1D-grid, or 100 ND nodes per interrogator in a 2D-grid.

5.5.1 Spatial multiplexing in a 1D-grid

In this section, we explore the use of spatial multiplexing, where each transceiver simultaneously transmits a TX beam to a different NDM and allows it to interrogate multiple NDMs within the same time slot. Note that for the RX BF, each transceiver can use the data from

[7]This approximately covers all transceivers that are direct neighbors of the transmitting transceiver. This number is based on Figure 5.6.

neighboring transceivers to extract the NDM signal. We only investigate the single-to-all LCMV BF, where the number of transceivers used to construct the RX BF is expressed in hops, where a single hop means that 3 transceivers (or 1 nearby neighbor) are used to construct the RX BF, i.e., two hops would correspond to the usage of 5 transceivers (transmitting transceiver plus the two neighbors on each side). In this context, we can define two extreme cases of spatial multiplexing[8]:

- Case 1: Each transceiver steers a focused TX beam to one NDM in its close neighborhood (see Figure 5.14(a)). In this case, we can interrogate one NDM per transceiver per time slot, or 8 NDMs per transceiver in total when sampled at 20 kHz. In each time slot, the spacing between different target NDMs of the different transceivers is maximized.
- Case 2: All NDMs are interrogated without a dedicated TX BF, i.e., we set $\mathbf{w}_{\mathrm{TX}} = \mathbf{1}$ (see Figure 5.14(b)). In this case, time-multiplexing can be fully omitted, since each transceiver simultaneously reads out the data from the set of NDMs that are assigned to it (roughly 10 NDMs per transceiver in a 1D-grid).

Figure 5.15 shows the results for Case 1, for the 10 target NDMs associated with the most central transceiver in the scenario, for different TD sizes. It is observed that 0.33 mm^2 TDs do not provide sufficient signal separation, and result in a very weak performance in terms of spike detection. If 0.2 mm^2 TDs are used, the performance is better, but still much poorer compared to the original neural signals recorded at the NDMs. When using 0.1 mm^2 TDs, the performance is almost as good as in the previous sections when there was no spatial multiplexing. Note that a 1-hop neighborhood is generally sufficient to have a good performance. This is not surprising, considering Figure 5.6, showing that most of the correlation can be captured in such a 1-hop neighborhood.

Figure 5.16 shows the results for Case 2, where the TX BF is omitted, i.e., $\mathbf{w}_{\mathrm{TX}} = \mathbf{1}$, and compares the performance with the best solutions in Case 1. It is observed that, although Case 2 is much more efficient and requires no TDM, it substantially degrades the performance. This suggests that an in-between solution (between Case 1 and Case 2) may be the best alternative.

5.6 Conclusion

In this chapter, we propose a general framework to analyze system design tradeoffs in the neural dust system in a simplified 1D-grid. Our analysis demonstrates that cooperation between different transceivers is unavoidable to achieve sufficient interference suppression. The choice for hardware implementations of such BF systems is determined by the available

[8]Note that even though we confined outselves to the above two cases, there are many intermediate possible configurations, where the number of slots can be varied both in the time-dimension (number of time slots per second) and in the spatial-dimension (number of simultaneously interrogated NDM per transceiver.)

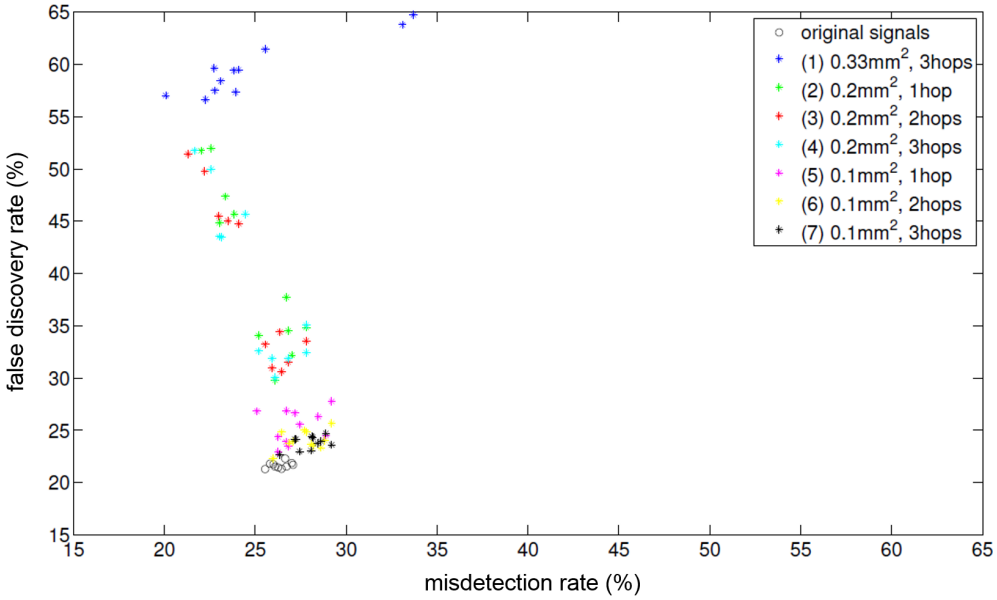

Figure 5.15: Comparison of BF configurations in spatial multiplexing scenario with TX BF. Note that a 1-hop neighborhood is generally sufficient to have a good performance.

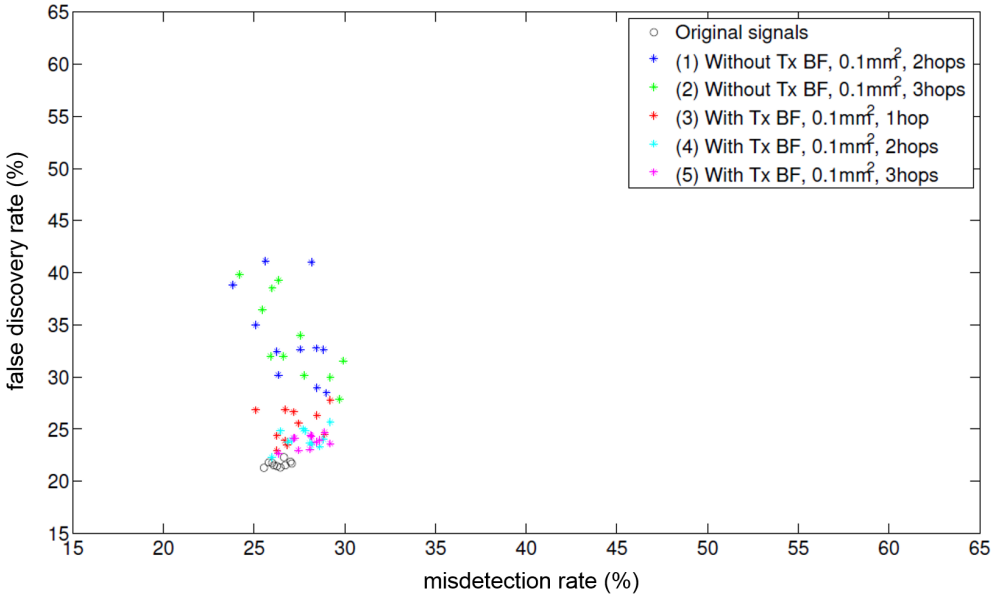

Figure 5.16: Comparison of spatial multiplexing scenario with and without TX BF suggests that in-between solution may be the best alternative.

communication bandwidth and the processing power. In order to reduce the processing and communication burden, we can consider a hierarchical processing flow where a BF is computed in two stages, i.e., each transceiver locally computes a BF signal, which is then combined with the BF signals of other transceivers by a global 2nd stage BF. In general, such an approach removes many degrees of freedom, and therefore the level of hierarchy should be carefully optimized. However, there also exist distributed realizations of the LCMV BF, which can be shown to be equivalent to a centralized realization, at the cost of a slower tracking.

Furthermore, as opposed to the current time-multiplexing method, which limits the rate of NDM interrogation, one could explore spatial multiplexing where multiple NDMs are interrogated simultaneously by the same TX beam(s). However, it is important to consider the additional interference caused by simultaneously interrogating the NDMs.

Finally, all simulations in this paper were applied to a 1D-grid of NDMs and transceivers, but the model can be extended to 2D and 3D-grids. Furthermore, the degree of realism in the model can be improved by adding uncertainty in the orientation of the NDMs (i.e., random directional reflectivity patterns) and adding time-variations in the signal statistics due to micro-motion of the cortex, changes in position or orientation of the NDMs, etc. We believe that these variations are sufficiently slow to track with adaptive algorithms. However, all this remains an open challenge.

Chapter 6

Conclusion and Future Research Directions

6.1 Conclusion

In this thesis, we present a wireless, ultrasonic neural sensor and communication system called *neural dust* that enables neural recordings in the central and peripheral nervous system. We analyzed the fundamental system design tradeoffs and ultimate size, power, and bandwidth scaling limits of neural dust. In brief, physics limits how small a good electromagnetics (or radio frequency) based receiver can be due to the long wavelengths of the wave-front (millimeters to centimeters) and the high degree of absorption of radio frequency energy into tissue (which heats up the tissue and limits the total power that can be sent to an implant). Ultrasonic systems fare much better in both areas, allowing for the design of extremely small receiver devices. In addition, the extreme miniaturization of lower power electronics and communication module based on backscattering allow for useful recording electronics to be incorporated into such small packages.

In order to verify the functionality of neural dust, we designed, built, and implanted neural dust in a stationary, anesthetized rodent model to collect compound action potentials from the main branch of the sciatic nerve as well as evoked electromyogram from the gastrocnemius muscle. We show that ultrasound is effective at delivering power to mm-scale devices in tissue; likewise, passive, batteryless communication using backscatter enables high-fidelity transmission of peripheral nerve signatures. The performance of the neural dust system was equivalent to conventional electrophysiological recording employing microelectrodes and cabled electronics.

Additionally, we discussed both theory and hardware implementation of a wearable, battery-powered, multi-element transceiver module that allows for beam steering of the ultrasonic beam. Several advantages of the platform include: (1) neural dust motes can be maintained on axis even in the face of relative motion between mote and external transducer; (2) multiple motes can potentially be interrogated by sweeping the focused beam electron-

ically; (3) post-surgical identification of mote location would be made easier. Our analysis of the scaled neural dust system with multiple transceivers and multiple neural dust motes implanted in the neocortex demonstrate that cooperation among transceivers is unavoidable to achieve sufficient interference suppression.

6.2 Future research directions

A number of technical challenges remain open in the realization of miniature, chronic, high-density, ultrasound-based neural recording systems. Current and future research efforts are described below.

Reduction of noise floor

Current neural dust prototype described in Chapter 4 achieves a noise floor of $\sim$180 μV_{rms} (averaged over 8 samples) and a dynamic range of $>$ 500 mV. On the other hand, extracellularly recorded signals from neurons in the neocortex and in the peripheral nerves range from 10's of μV to $\sim$10 mV. As a result, the current system cannot achieve sufficient signal-to-noise (SNR) ratio to reliably resolve neural spikes or compound action potentials. Given that our current setup operates at 0.03% of the FDA regulatory limit, increasing the power levels can improve the overall SNR. Alternatively, since the current neural front-end (i.e., single-transistor passive backscatter circuit) under-utilizes the available dynamic range, low-noise amplifier can be added to the front-end to increase the input range.

As a result, we[1] taped-out ultrasonically-powered neural front-end circuit in TSMC 65 nm low-power (LP) process. The design is largely adopted from [10] and [71] and achieves a simulated input referred noise of $<$ 6 μV_{rms}, variable gain up to 46 dB, 20 kHz of bandwidth with 10 bits of resolution, and digital downlink and miller-modulated uplink backscatter communication, all under $\sim$5 μW of power consumption. Low-noise, low-power front-end significantly reduces the noise floor of the system and digital communication alleviates issues that arise from misalignment.

Microassembly of motes

The calculated scaling predictions in Chapter 3 suggest that 100 μm scale motes are able to capture sufficient power and backscatter sensitivity. In order to build sub-mm motes, a number of material and microfabrication challenges exist, including the use of microfabricated backplanes, solder microbumping assembly of components (instead of the conventional wire-bonding approach used previously), and a robust, wafer-scale processing flow. Furthermore, the fabrication of a "tail" discussed in Chapter 3, which can break the inherent tradeoff between the size of individual motes and the achievable SNR, presents an additional fabrication challenge.

[1] In collaboration with Kyoungtae Lee.

Chronic encapsulation

Mechanically, the total displacement of the piezoelectric transducer when actuated is in the nanometer regime, which means that thin film encapsulation is suitable for packaging the system (keeping in mind, of course, the caveats presented by thin film encapsulation, including biocompatibility, water penetration, inertness, etc.). Common thin films used for chronic implantation of this kind include parylene, medical grade polyimide, and increasingly, more groups are investigating the use of silicon carbide [7, 52, 60]. In addition, independent of the thin film encapsulant used, biocompatible alternatives to PZT, such as $BaTiO_3$, can be used for chronic implantation.

Delivery

The most direct approach would be to implant neural dust motes at the tips of fine-wire arrays similar to those already used for neural recording. In this scenario, neural dust motes would be fabricated or post-fab assembled on the tips of array shanks, held there by surface tension or resorbable layers and inserted into the cortex. Once inserted and free, the array shank would be withdrawn, allowing the tissue to heal.

Kinetic delivery might also be an option, but there is no existing data to evaluate what effect such a method would have on brain tissue or the device themselves. Additionally, as demonstrated in [77], motes can potentially be delivered via the vasculature, where motes would be post-fabricated on commercially available stents and record from the vessel wall. Alternatively, motes can be inserted in the cisterna magna which can allow ready access to the cerebral spinal fluid (CSF), which has a generally well-mapped path circulating the cortex [11]. Finally, macrophages can engulf foreign structures up to at least 20 μm in diameter [13] and can be used as potential delivery vehicles to deliver tiny motes across the barriers.

Beamforming transceiver

Hardware implementation of sophisticated beamforming algorithms that are making use of techniques such as beam steering, multi-input, multi-output (MIMO) system theory, and deep learning is underway. As discussed in Chapter 5, when employing multiple embedded dust motes, interrogating and identifying the signals from an individual neural dust mote are challenging due to interference from surrounding motes. This necessitates a transceiver with multiple, independently addressable transducer elements acting in an array.

Furthermore, implementation can take the form of a hierarchical or distributed processing flow, where multiple signals are fused into a smaller set of signals before transmission to the next processing stage. As an example, for a beamformer (BF) to be computed in two stages, each transceiver locally computes a BF signal then combined with the BF signals of other transceivers by a global 2nd stage BF. Optimization at both algorithm and hardware implementation levels must be fully explored to achieve sufficient interference suppression to resolve simultaneous signals from different motes via spatial or time multiplexing.

Stimulation

The design and fabrication of ultrasound-powered neural stimulation systems is in progress. Stimulation can either be done electrically based on charge release through electrodes on the dust motes [9, 56, 90], chemically by precisely controlling drug release [19, 23, 57], ultrasonically by enhancing the transport of molecules into or through biological tissue [51, 65, 106], or with hybrid techniques such as opto-genetic [15] and photo-acoustic [30] stimulation. Combination of recording and stimulating dust motes can enable chronic, real-time closed-loop neuromodulation.

Non-neural applications

Beyond interfacing with the nervous system, miniature, ultrasound-based implantable devices can enable a number of non-neural applications. One of the principal strengths of neural dust is that ultrasound is significantly more efficient at powering miniature sensors embedded deep within the body compared to conventional radio frequency technology.

As this platform presents a generalized power delivery and communication module, sensors (i.e., electrodes) as well as the front-end can be modified to detect non-electrical, yet viable biological signatures such as oxygen, temperature, glucose, or hormone levels. A suite of these sensors can be implanted anywhere in the body to monitor and precisely deliver necessary therapy at the desired target site.

All remains an open yet exciting opportunity.

Bibliography

[1] A.P. Alivisatos et al. "The Brain Activity Map". In: *Science* 339.6125 (2013), pp. 1284–1285. ISSN: 0036-8075. DOI: 10.1126/science.1236939.

[2] V.E. Amassian et al. "Simultaneous recording of the activities of several individual cortical neurons". In: *Transactions of the New York Academy of Sciences* 21.5 Series II (1959), pp. 395–405. ISSN: 2164-0947. DOI: 10.1111/j.2164-0947.1959.tb01676.x.

[3] O. Aquilina. "A brief history of cardiac pacing". In: *Images Paediatr Cardiol* 8.2 (2006), pp. 17–81. ISSN: 1729-441X. URL: http://www.ncbi.nlm.nih.gov/pmc/articles/PMC3232561/.

[4] S. Ayazian and A. Hassibi. "Delivering optical power to subcutaneous implanted devices". In: *2011 Annual International Conference of the IEEE Engineering in Medicine and Biology Society*. 2011, pp. 2874–2877. DOI: 10.1109/IEMBS.2011.6090793.

[5] C.A. Balanis. *Antenna Theory: Analysis and Design*. 3rd ed. Hoboken, NJ: Wiley, 2005.

[6] R.H. Baughman et al. "Negative Poisson's ratios as a common feature of cubic metals". In: *Nature* 392.6674 (1998), pp. 362–365. ISSN: 0028-0836. DOI: 10.1038/32842.

[7] E. Bernardin et al. "Development of an all-SiC neuronal interface device". In: *MRS Advances* (May 2016), pp. 1–6. DOI: 10.1557/adv.2016.360.

[8] A. Bertrand et al. "Beamforming approaches for untethered, ultrasonic neural dust motes for cortical recording: A simulation study". In: *2014 36th Annual International Conference of the IEEE Engineering in Medicine and Biology Society*. 2014, pp. 2625–2628. DOI: 10.1109/EMBC.2014.6944161.

[9] W. Biederman et al. "A 4.78 mm^2 Fully-Integrated Neuromodulation SoC Combining 64 Acquisition Channels With Digital Compression and Simultaneous Dual Stimulation". In: *IEEE Journal of Solid-State Circuits* 50.4 (2015), pp. 1038–1047. ISSN: 0018-9200. DOI: 10.1109/JSSC.2014.2384736.

[10] W. Biederman et al. "A Fully-Integrated, Miniaturized (0.125 mm^2) 10.5 μW Wireless Neural Sensor". In: *IEEE Journal of Solid-State Circuits* 48.4 (2013), pp. 960–970. ISSN: 0018-9200. DOI: 10.1109/JSSC.2013.2238994.

[11] T. Brinker et al. "A new look at cerebrospinal fluid circulation". In: *Fluids and Barriers of the CNS* 11.1 (2014), p. 10. ISSN: 2045-8118. DOI: 10.1186/2045-8118-11-10.

[12] G. Buzsaki. "Large-scale recording of neuronal ensembles". In: *Nat Neurosci* 7.5 (2004), pp. 446–451. ISSN: 1097-6256. DOI: 10.1038/nn1233.

[13] G.J. Cannon and J.A. Swanson. "The macrophage capacity for phagocytosis". In: *Journal of Cell Science* 101.4 (1992), pp. 907–913. ISSN: 0021-9533. URL: http://jcs.biologists.org/content/101/4/907.

[14] M. Capogrosso et al. "A brain-spine interface alleviating gait deficits after spinal cord injury in primates". In: *Nature* 539.7628 (2016). Letter, pp. 284–288. ISSN: 0028 0836. URL: http://dx.doi.org/10.1038/nature20118.

[15] J.A. Cardin et al. "Targeted optogenetic stimulation and recording of neurons in vivo using cell-type-specific expression of Channelrhodopsin-2". In: *Nat. Protocols* 5.2 (2010), pp. 247–254. ISSN: 1754-2189. DOI: 10.1038/nprot.2009.228.

[16] J.M. Carmena et al. "Learning to Control a BrainMachine Interface for Reaching and Grasping by Primates". In: *PLOS Biology* 1.2 (Oct. 2003). DOI: 10.1371/journal.pbio.0000042.

[17] J.K. Chapin et al. "Real-time control of a robot arm using simultaneously recorded neurons in the motor cortex". In: *Nat Neurosci* 2.7 (1999), pp. 664–670. ISSN: 1097-6256. DOI: 10.1038/10223.

[18] J. Charthad et al. "A mm-Sized Implantable Medical Device (IMD) With Ultrasonic Power Transfer and a Hybrid Bi-Directional Data Link". In: *IEEE Journal of Solid-State Circuits* 50.8 (2015), pp. 1741–1753. ISSN: 0018-9200. DOI: 10.1109/JSSC.2015.2427336.

[19] J. Charthad et al. "An ultrasonically powered implantable device for targeted drug delivery". In: *2016 38th Annual International Conference of the IEEE Engineering in Medicine and Biology Society (EMBC)*. 2016, pp. 541–544. DOI: 10.1109/EMBC.2016.7590759.

[20] A. Cheng et al. "Simultaneous two-photon calcium imaging at different depths with spatiotemporal multiplexing". In: *Nat Meth* 8.2 (2011), pp. 139–142. ISSN: 1548-7091. DOI: 10.1038/nmeth.1552.

[21] J.L. Collinger et al. "High-performance neuroprosthetic control by an individual with tetraplegia". In: *The Lancet* 381.9866 (2013), pp. 557 –564. ISSN: 0140-6736. URL: http://dx.doi.org/10.1016/S0140-6736(12)61816-9.

[22] G.H. Creasey et al. "An implantable neuroprosthesis for restoring bladder and bowel control to patients with spinal cord injuries: A multicenter trial". In: *Archives of Physical Medicine and Rehabilitation* 82.11 (2001), pp. 1512 –1519. ISSN: 0003-9993. URL: http://www.sciencedirect.com/science/article/pii/S000399930128229X.

[23] A.K. Dash and G.C. Cudworth II. "Therapeutic applications of implantable drug delivery systems". In: *Journal of Pharmacological and Toxicological Methods* 40.1 (1998), pp. 1 –12. ISSN: 1056-8719. URL: http://www.sciencedirect.com/science/article/pii/S1056871998000276.

[24] K. Deisseroth. "Optogenetics". In: *Nat Meth* 8.1 (2011). Commentary, pp. 26–29. ISSN: 1548-7091. URL: http://dx.doi.org/10.1038/nmeth.f.324.

[25] T. Denison et al. "A 2 μW 100 nV/rtHz Chopper-Stabilized Instrumentation Amplifier for Chronic Measurement of Neural Field Potentials". In: *IEEE Journal of Solid-State Circuits* 42.12 (2007), pp. 2934–2945. ISSN: 0018-9200. DOI: 10.1109/JSSC.2007.908664.

[26] J. Du et al. "High-Resolution Three-Dimensional Extracellular Recording of Neuronal Activity With Microfabricated Electrode Arrays". In: *Journal of Neurophysiology* 101.3 (2009), pp. 1671–1678. ISSN: 0022-3077. DOI: 10.1152/jn.90992.2008.

[27] J. Du et al. "Multiplexed, High Density Electrophysiology with Nanofabricated Neural Probes". In: *PLOS ONE* 6.10 (Oct. 2011), pp. 1–11. DOI: 10.1371/journal.pone.0026204.

[28] M. Ducros et al. "Encoded multisite two-photon microscopy". In: 110.32 (2013), pp. 13138–13143. DOI: 10.1073/pnas.1307818110.

[29] K. Famm et al. "Drug discovery: A jump-start for electroceuticals". In: *Nature* 496.7444 (2013). Comment, pp. 159–161. ISSN: 0028-0836. URL: http://dx.doi.org/10.1038/496159a.

[30] G.S. Filonov et al. "Deep-Tissue Photoacoustic Tomography of a Genetically Encoded Near-Infrared Fluorescent Probe". In: *Angewandte Chemie International Edition* 51.6 (2012), pp. 1448–1451. ISSN: 1521-3773. DOI: 10.1002/anie.201107026.

[31] K. Finkenzeller. *RFID Handbook: Fundamentals and Applications in Contactless Smart Cards and Identification*. New York, NY: Wiley, 2003.

[32] S.N. Flesher et al. "Intracortical microstimulation of human somatosensory cortex". In: *Science Translational Medicine* (2016). ISSN: 1946-6234. DOI: 10.1126/scitranslmed.aaf8083.

[33] J.D. Foster et al. "A freely-moving monkey treadmill model". In: *Journal of Neural Engineering* 11.4 (2014), p. 046020. URL: http://stacks.iop.org/1741-2552/11/i=4/a=046020.

[34] K. Fotopoulou and B.W. Flynn. "Wireless Power Transfer in Loosely Coupled Links: Coil Misalignment Model". In: *IEEE Transactions on Magnetics* 47.2 (2011), pp. 416–430. ISSN: 0018-9464. DOI: 10.1109/TMAG.2010.2093534.

[35] J.I. Glaser et al. "Statistical Analysis of Molecular Signal Recording". In: *PLOS Computational Biology* 9.7 (July 2013), pp. 1–14. DOI: 10.1371/journal.pcbi.1003145.

[36] C. Gold, D.A. Henze, and C. Koch. "Using extracellular action potential recordings to constrain compartmental models". In: *Journal of Computational Neuroscience* 23.1 (2007), pp. 39–58. ISSN: 1573-6873. DOI: 10.1007/s10827-006-0018-2.

[37] J.A. Gruner and C.P. Mason. "Nonlinear muscle recruitment during intramuscular and nerve stimulation". In: *Journal of rehabilitation research and development* 26.2 (1989), 116. ISSN: 0748-7711. URL: http://europepmc.org/abstract/MED/2724148.

[38] J.S. Ho, S. Kim, and A.S.Y. Poon. "Midfield Wireless Powering for Implantable Systems". In: *Proceedings of the IEEE* 101.6 (2013), pp. 1369–1378. ISSN: 0018-9219. DOI: 10.1109/JPROC.2013.2251851.

[39] J.S. Ho et al. "Self-Tracking Energy Transfer for Neural Stimulation in Untethered Mice". In: *Phys. Rev. Applied* 4 (2 2015), p. 024001. DOI: 10.1103/PhysRevApplied.4.024001.

[40] L.R. Hochberg et al. "Reach and grasp by people with tetraplegia using a neurally controlled robotic arm". In: *Nature* 485.7398 (2012), pp. 372–375. ISSN: 0028-0836. DOI: 10.1038/nature11076.

[41] R. Holland. "Resonant Properties of Piezoelectric Ceramic Rectangular Parallelepipeds". In: *Acoustical Society of America Journal* 43 (1968), p. 988. DOI: 10.1121/1.1910969.

[42] S. Holm. "Ultrasim - a toolbox for ultrasound field simulation". In: *Proc. Nordic Matlab conference*. 2001. URL: http://folk.uio.no/sverre/papers/01_Matlab.pdf.

[43] P.R. Hoskins, K. Martin, and A. Thrush. *Diagnostic Ultrasound: Physics and Equipment*. 2nd ed. New York, NY: Cambridge University Press, 2010.

[44] Y. Hu et al. "Transmitting electric energy through a metal wall by acoustic waves using piezoelectric transducers". In: *IEEE Transactions on Ultrasonics, Ferroelectrics, and Frequency Control* 50.7 (2003), pp. 773–781. ISSN: 0885-3010. DOI: 10.1109/TUFFC.2003.1214497.

[45] A. Hyvarinen and E. Oja. "Independent component analysis: algorithms and applications". In: *Neural Networks* 13.45 (2000), pp. 411 –430. ISSN: 0893-6080. URL: http://www.sciencedirect.com/science/article/pii/S0893608000000265.

[46] "IEEE Standard for Safety Levels with Respect to Human Exposure to Radio Frequency Electromagnetic Fields, 3 kHz to 300 GHz". In: 2006. URL: http://emfguide.itu.int/pdfs/C95.1-2005.pdf.

[47] "Information for Manufacturers Seeking Marketing Clearance of Diagnostic Ultrasound Systems and Transducers". In: 2008. URL: http://www.fda.gov/downloads/UCM070911.pdf.

[48] R. Jegadeesan, Y.X. Guo, and M. Je. "Electric near-field coupling for wireless power transfer in biomedical applications". In: *2013 IEEE MTT-S International Microwave Workshop Series on RF and Wireless Technologies for Biomedical and Healthcare Applications (IMWS-BIO)*. 2013, pp. 1–3. DOI: 10.1109/IMWS-BIO.2013.6756140.

[49] U.M. Jow and M. Ghovanloo. "Design and Optimization of Printed Spiral Coils for Efficient Transcutaneous Inductive Power Transmission". In: *IEEE Transactions on Biomedical Circuits and Systems* 1.3 (2007), pp. 193–202. ISSN: 1932-4545. DOI: 10.1109/TBCAS.2007.913130.

[50] M. Kiani, U.M. Jow, and M. Ghovanloo. "Design and Optimization of a 3-Coil Inductive Link for Efficient Wireless Power Transmission". In: *IEEE Transactions on Biomedical Circuits and Systems* 5.6 (2011), pp. 579–591. ISSN: 1932-4545. DOI: 10.1109/TBCAS.2011.2158431.

[51] R.L. King et al. "Effective Parameters for Ultrasound-Induced In Vivo Neurostimulation". In: *Ultrasound in Medicine and Biology* 39.2 (2013), pp. 312 –331. ISSN: 0301-5629. URL: http://www.sciencedirect.com/science/article/pii/S0301562912005753.

[52] G.L. Knaack et al. "In vivo Characterization of Amorphous Silicon Carbide As a Biomaterial for Chronic Neural Interfaces". In: *Frontiers in Neuroscience* 10 (2016), p. 301. ISSN: 1662-453X. DOI: 10.3389/fnins.2016.00301.

[53] K.P. Kording. "Of Toasters and Molecular Ticker Tapes". In: *PLOS Computational Biology* 7.12 (Dec. 2011), pp. 1–5. DOI: 10.1371/journal.pcbi.1002291.

[54] R. Krimholtz, D.A. Leedom, and G.L. Matthaei. "New equivalent circuits for elementary piezoelectric transducers". In: *Electronics Letters* 6.13 (1970), pp. 398–399. ISSN: 0013-5194. DOI: 10.1049/el:19700280.

[55] E. Krook-Magnuson et al. "Neuroelectronics and biooptics: Closed-loop technologies in neurological disorders". In: *JAMA Neurology* 72.7 (2015), pp. 823–829. ISSN: 2168-6149. DOI: 10.1001/jamaneurol.2015.0608.

[56] P.J. Larson and B.C. Towe. "Miniature ultrasonically powered wireless nerve cuff stimulator". In: *2011 5th International IEEE/EMBS Conference on Neural Engineering*. 2011, pp. 265–268. DOI: 10.1109/NER.2011.5910538.

[57] D.A. LaVan, T. McGuire, and R. Langer. "Small-scale systems for in vivo drug delivery". In: *Nat Biotech* 21.10 (2003), pp. 1184–1191. ISSN: 1087-0156. DOI: 10.1038/nbt876.

[58] B. Lee, M. Kiani, and M. Ghovanloo. "A Triple-Loop Inductive Power Transmission System for Biomedical Applications". In: *IEEE Transactions on Biomedical Circuits and Systems* 10.1 (2016), pp. 138–148. ISSN: 1932-4545. DOI: 10.1109/TBCAS.2014.2376965.

[59] S.B. Lee et al. "A Wideband Dual-Antenna Receiver for Wireless Recording From Animals Behaving in Large Arenas". In: *IEEE Transactions on Biomedical Engineering* 60.7 (2013), pp. 1993–2004. ISSN: 0018-9294. DOI: 10.1109/TBME.2013.2247603.

[60] X. Lei et al. "SiC protective coating for photovoltaic retinal prosthesis". In: *Journal of Neural Engineering* 13.4 (2016), p. 046016. URL: http://stacks.iop.org/1741-2552/13/i=4/a=046016.

[61] R.G. Lorenz and S.P. Boyd. "Robust minimum variance beamforming". In: *IEEE Transactions on Signal Processing* 53.5 (2005), pp. 1684–1696. ISSN: 1053-587X. DOI: 10.1109/TSP.2005.845436.

[62] A.H. Marblestone et al. "Physical Principles for Scalable Neural Recording". In: *ArXiv e-prints* (June 2013). arXiv: 1306.5709 [q-bio.NC].

[63] E.M. Maynard, C.T. Nordhausen, and R.A. Normann. "The Utah Intracortical Electrode Array: A recording structure for potential brain-computer interfaces". In: *Electroencephalography and Clinical Neurophysiology* 102.3 (1997), pp. 228 –239. ISSN: 0013-4694. URL: http://www.sciencedirect.com/science/article/pii/S0013469496951760.

[64] H. Meng and M. Sahin. "An electroacoustic recording device for wireless sensing of neural signals". In: *2013 35th Annual International Conference of the IEEE Engineering in Medicine and Biology Society (EMBC)*. 2013, pp. 3086–3088. DOI: 10.1109/EMBC.2013.6610193.

[65] M.D. Menz et al. "Precise Neural Stimulation in the Retina Using Focused Ultrasound". In: *Journal of Neuroscience* 33.10 (2013), pp. 4550–4560. ISSN: 0270-6474. DOI: 10.1523/JNEUROSCI.3521-12.2013.

[66] R.A. Mezzarane et al. "Electrodiagnosis in New Frontiers of Clinical Research". In: Rijeka: InTech, 2013. Chap. Experimental and Simulated EMG Responses in the Study of the Human Spinal Cord, Ch. 0. URL: http://dx.doi.org/10.5772/54870.

[67] D.M. Mills and S.W. Smith. "Multi-layered PZT/polymer composites to increase signal-to-noise ratio and resolution for medical ultrasound transducers. II. Thick film technology". In: *IEEE Transactions on Ultrasonics, Ferroelectrics, and Frequency Control* 49.7 (2002), pp. 1005–1014. ISSN: 0885-3010. DOI: 10.1109/TUFFC.2002.1020171.

[68] H. Miranda et al. "HermesD: A High-Rate Long-Range Wireless Transmission System for Simultaneous Multichannel Neural Recording Applications". In: *IEEE Transactions on Biomedical Circuits and Systems* 4.3 (2010), pp. 181–191. ISSN: 1932-4545. DOI: 10.1109/TBCAS.2010.2044573.

[69] S.S. Mohan et al. "Simple accurate expressions for planar spiral inductances". In: *IEEE Journal of Solid-State Circuits* 34.10 (1999), pp. 1419–1424. ISSN: 0018-9200. DOI: 10.1109/4.792620.

[70] M. Mujeeb-U-Rahman et al. "Optical power transfer and communication methods for wireless implantable sensing platforms". In: *Journal of Biomedical Optics* 20.9 (2015), p. 095012. DOI: 10.1117/1.JBO.20.9.095012.

[71] R. Muller, S. Gambini, and J. M. Rabaey. "A 0.013 mm^2, 5 μW, DC-Coupled Neural Signal Acquisition IC With 0.5 V Supply". In: *IEEE Journal of Solid-State Circuits* 47.1 (2012), pp. 232–243. ISSN: 0018-9200. DOI: 10.1109/JSSC.2011.2163552.

[72] M.A.L. Nicolelis et al. "Chronic, multisite, multielectrode recordings in macaque monkeys". In: *Proceedings of the National Academy of Sciences* 100.19 (2003), pp. 11041–11046. DOI: 10.1073/pnas.1934665100.

[73] P. Nuyujukian et al. "A High-Performance Keyboard Neural Prosthesis Enabled by Task Optimization". In: *IEEE Transactions on Biomedical Engineering* 62.1 (2015), pp. 21–29. ISSN: 0018-9294. DOI: 10.1109/TBME.2014.2354697.

[74] I. Obeid and P.D. Wolf. "Evaluation of spike-detection algorithms fora brain-machine interface application". In: *IEEE Transactions on Biomedical Engineering* 51.6 (2004), pp. 905–911. ISSN: 0018-9294. DOI: 10.1109/TBME.2004.826683.

[75] A.L. Orsborn et al. "Closed-Loop Decoder Adaptation Shapes Neural Plasticity for Skillful Neuroprosthetic Control". In: *Neuron* 82.6 (2014), pp. 1380 –1393. ISSN: 0896-6273. URL: http://www.sciencedirect.com/science/article/pii/S0896627314003638.

[76] B. Otis, Y.H. Chee, and J.M. Rabaey. "A 400 μW-RX, 1.6 mW-TX super-regenerative transceiver for wireless sensor networks". In: *IEEE International Solid-State Circuits Conference (ISSCC) Digest of Technical Papers*. 2005, 396–606 Vol. 1. DOI: 10.1109/ISSCC.2005.1494036.

[77] T.J. Oxley et al. "Minimally invasive endovascular stent-electrode array for high-fidelity, chronic recordings of cortical neural activity". In: *Nat Biotech* 34.3 (2016), pp. 320–327. ISSN: 1087-0156. URL: http://dx.doi.org/10.1038/nbt.3428.

[78] S. Ozeri and D. Shmilovitz. "Ultrasonic transcutaneous energy transfer for powering implanted devices". In: *Ultrasonics* 50.6 (2010), pp. 556 –566. ISSN: 0041-624X. URL: http://www.sciencedirect.com/science/article/pii/S0041624X09001991.

[79] S. Ozeri et al. "Ultrasonic transcutaneous energy transfer using a continuous wave 650 kHz Gaussian shaded transmitter". In: *Ultrasonics* 50.7 (2010), pp. 666 –674. ISSN: 0041-624X. URL: http://www.sciencedirect.com/science/article/pii/S0041624X1000017X.

[80] A.M. Packer, B. Roska, and M. Hausser. "Targeting neurons and photons for optogenetics". In: *Nat Neurosci* 16.7 (2013). Review, pp. 805–815. ISSN: 1097-6256. URL: http://dx.doi.org/10.1038/nn.3427.

[81] V.S. Polikov, P.A. Tresco, and W.M. Reichert. "Response of brain tissue to chronically implanted neural electrodes". In: *Journal of Neuroscience Methods* 148.1 (2005), pp. 1 –18. ISSN: 0165-0270. URL: http://www.sciencedirect.com/science/article/pii/S0165027005002931.

[82] D.M. Pozar. *Microwave Engineering*. 3rd ed. Wiley, 2005.

[83] R.J. Przybyla et al. "In-Air Rangefinding With an AlN Piezoelectric Micromachined Ultrasound Transducer". In: *IEEE Sensors Journal* 11.11 (2011), pp. 2690–2697. ISSN: 1530-437X. DOI: 10.1109/JSEN.2011.2157490.

[84] J.M. Rabaey et al. "Powering and communicating with mm-size implants". In: *2011 Design, Automation Test in Europe*. 2011, pp. 1–6. DOI: 10.1109/DATE.2011.5763123.

[85] S. Rajangam et al. "Wireless Cortical Brain-Machine Interface for Whole-Body Navigation in Primates". In: *Scientific Reports* 6 (2016), 22170 EP –. URL: http://dx.doi.org/10.1038/srep22170.

[86] A.K. RamRakhyani, S. Mirabbasi, and M. Chiao. "Design and Optimization of Resonance-Based Efficient Wireless Power Delivery Systems for Biomedical Implants". In: *IEEE Transactions on Biomedical Circuits and Systems* 5.1 (2011), pp. 48–63. ISSN: 1932-4545. DOI: 10.1109/TBCAS.2010.2072782.

[87] J.E.B. Randles. "Kinetics of rapid electrode reactions". In: *Discuss. Faraday Soc.* 1 (0 1947), pp. 11–19. URL: http://dx.doi.org/10.1039/DF9470100011.

[88] H.G. Rey, C. Pedreira, and R.Q. Quiroga. "Past, present and future of spike sorting techniques". In: *Brain Research Bulletin* 119, Part B (2015). Advances in electrophysiological data analysis, pp. 106 –117. ISSN: 0361-9230. URL: http://www.sciencedirect.com/science/article/pii/S0361923015000684.

[89] S. Roa-Prada et al. "An Ultrasonic Through-Wall Communication (UTWC) System Model". In: *Journal of Vibration and Acoustics* 135.1 (2013), pp. 011004–011004. ISSN: 1048-9002. DOI: 10.1115/1.4007565.

[90] J.T. Robinson, M. Jorgolli, and H. Park. "Nanowire electrodes for high-density stimulation and measurement of neural circuits". In: *Front Neural Circuits* 7 (2013), p. 38. ISSN: 1662-5110. DOI: 10.3389/fncir.2013.00038.

[91] S.J. Roundy. "Energy Scavenging for Wireless Sensor Nodes with a Focus on Vibration to Electricity Conversion". PhD thesis. University of California, Berkeley, 2003.

[92] A. Salim, A. Baldi, and B. Ziaie. "Inductive link modeling and design guidelines for optimum power transfer in implantable wireless microsystems". In: *Proceedings of the 25th Annual International Conference of the IEEE Engineering in Medicine and Biology Society (IEEE Cat. No.03CH37439)*. Vol. 4. 2003, 3368–3371 Vol.4. DOI: 10.1109/IEMBS.2003.1280867.

[93] A.P. Sample et al. "Enabling Seamless Wireless Power Delivery in Dynamic Environments". In: *Proceedings of the IEEE* 101.6 (2013), pp. 1343–1358. ISSN: 0018-9219. DOI: 10.1109/JPROC.2013.2252453.

[94] D.A. Schwarz et al. "Chronic, wireless recordings of large-scale brain activity in freely moving rhesus monkeys". In: *Nat Meth* 11.6 (2014), pp. 670–676. ISSN: 1548-7091. URL: http://dx.doi.org/10.1038/nmeth.2936.

[95] D. Seo et al. "Model validation of untethered, ultrasonic neural dust motes for cortical recording". In: *Journal of Neuroscience Methods* 244 (2015), pp. 114 –122. ISSN: 0165-0270. URL: http://www.sciencedirect.com/science/article/pii/S0165027014002842.

[96] D. Seo et al. "Neural Dust: An Ultrasonic, Low Power Solution for Chronic Brain-Machine Interfaces". In: *arXiv e-prints* (July 2013). arXiv: 1307.2196 [q-bio.NC].

[97] D. Seo et al. "Ultrasonic beamforming system for interrogating multiple implantable sensors". In: *2015 37th Annual International Conference of the IEEE Engineering in Medicine and Biology Society (EMBC)*. 2015, pp. 2673–2676. DOI: 10.1109/EMBC.2015.7318942.

[98] D. Seo et al. "Wireless Recording in the Peripheral Nervous System with Ultrasonic Neural Dust". In: *Neuron* 91.3 (2016), pp. 529 –539. ISSN: 0896-6273. URL: http://www.sciencedirect.com/science/article/pii/S0896627316303440.

[99] I.H. Stevenson and K.P. Kording. "How advances in neural recording affect data analysis". In: *Nat Neurosci* 14.2 (2011), pp. 139–142. ISSN: 1097-6256. DOI: 10.1038/nn.2731.

[100] M.S.J. Steyaert and W.M.C. Sansen. "A micropower low-noise monolithic instrumentation amplifier for medical purposes". In: *IEEE Journal of Solid-State Circuits* 22.6 (1987), pp. 1163–1168. ISSN: 0018-9200. DOI: 10.1109/JSSC.1987.1052869.

[101] P.J. Strollo et al. "Upper-Airway Stimulation for Obstructive Sleep Apnea". In: *New England Journal of Medicine* 370.2 (2014), pp. 139–149. DOI: 10.1056/NEJMoa1308659.

[102] T.A. Szuts et al. "A wireless multi-channel neural amplifier for freely moving animals". In: *Nat Neurosci* 14.2 (2011), pp. 263–269. ISSN: 1097-6256. DOI: 10.1038/nn.2730.

[103] M. Tabesh et al. "A Power-Harvesting Pad-Less Millimeter-Sized Radio". In: *IEEE Journal of Solid-State Circuits* 50.4 (2015), pp. 962–977. ISSN: 0018-9200. DOI: 10.1109/JSSC.2014.2384034.

[104] H.Y. Tang et al. "Integrated ultrasonic system for measuring body-fat composition". In: *IEEE International Solid-State Circuits Conference (ISSCC) Digest of Technical Papers*. 2015, pp. 1–3. DOI: 10.1109/ISSCC.2015.7063000.

[105] H.Y. Tang et al. "Miniaturizing Ultrasonic System for Portable Health Care and Fitness". In: *IEEE Transactions on Biomedical Circuits and Systems* 9.6 (2015), pp. 767–776. ISSN: 1932-4545. DOI: 10.1109/TBCAS.2015.2508439.

[106] Y. Tufail et al. "Ultrasonic neuromodulation by brain stimulation with transcranial ultrasound". In: *Nat. Protocols* 6.9 (2011), pp. 1453–1470. ISSN: 1754-2189. DOI: 10.1038/nprot.2011.371.

[107] B.D. Van Veen and K.M. Buckley. "Beamforming: a versatile approach to spatial filtering". In: *IEEE ASSP Magazine* 5.2 (1988), pp. 4 –24. ISSN: 0740-7467. DOI: 10.1109/53.665.

[108] X. Wang et al. "Noninvasive laser-induced photoacoustic tomography for structural and functional in vivo imaging of the brain". In: *Nat Biotech* 21.7 (2003), pp. 803–806. ISSN: 1087-0156. DOI: 10.1038/nbt839.

[109] K.D. Wise et al. "Wireless implantable microsystems: high-density electronic interfaces to the nervous system". In: *Proceedings of the IEEE* 92.1 (2004), pp. 76–97. ISSN: 0018-9219. DOI: 10.1109/JPROC.2003.820544.

[110] C. Xie et al. "Intracellular recording of action potentials by nanopillar electroporation". In: *Nat Nano* 7.3 (2012), pp. 185–190. ISSN: 1748-3387. DOI: 10.1038/nnano.2012.8.

[111] R.F. Xue, K.W. Cheng, and M. Je. "High-Efficiency Wireless Power Transfer for Biomedical Implants by Optimal Resonant Load Transformation". In: *IEEE Transactions on Circuits and Systems I: Regular Papers* 60.4 (2013), pp. 867–874. ISSN: 1549-8328. DOI: 10.1109/TCSI.2012.2209297.

[112] R.F. Yazicioglu et al. "A 30 μW Analog Signal Processor ASIC for Portable Biopotential Signal Monitoring". In: *IEEE Journal of Solid-State Circuits* 46.1 (2011), pp. 209–223. ISSN: 0018-9200. DOI: 10.1109/JSSC.2010.2085930.

[113] M. Yin et al. "Wireless Neurosensor for Full-Spectrum Electrophysiology Recordings during Free Behavior". In: *Neuron* 84.6 (2014), pp. 1170 –1182. ISSN: 0896-6273. URL: http://www.sciencedirect.com/science/article/pii/S0896627314010101.

[114] B.M. Zamft et al. "Measuring Cation Dependent DNA Polymerase Fidelity Landscapes by Deep Sequencing". In: *PLOS ONE* 7.8 (Aug. 2012), pp. 1–10. DOI: 10.1371/journal.pone.0043876.

[115] Y. Ziv et al. "Long-term dynamics of CA1 hippocampal place codes". In: *Nat Neurosci* 16.3 (2013). 10.1038/nn.3329, 264 EP –266. ISSN: 1097-6256. DOI: 10.1038/nn.3329.